



## Review

# Advanced paramagnetic resonance spectroscopies of iron–sulfur proteins: Electron nuclear double resonance (ENDOR) and electron spin echo envelope modulation (ESEEM) <sup>☆</sup>



George E. Cutsail III <sup>a</sup>, Joshua Telser <sup>b,1</sup>, Brian M. Hoffman <sup>a</sup>

<sup>a</sup> Department of Chemistry, Northwestern University, 2145 Sheridan Road, Evanston, IL 60208, USA

<sup>b</sup> Department of Biological, Chemical and Physical Sciences, Roosevelt University, Chicago, IL 60605, USA

## ARTICLE INFO

## Article history:

Received 20 November 2014

Received in revised form 29 January 2015

Accepted 29 January 2015

Available online 14 February 2015

## Keywords:

Advanced paramagnetic resonance spectroscopy of iron–sulfur proteins  
Electron nuclear double resonance (ENDOR)  
Electron spin echo envelope modulation (ESEEM)

## ABSTRACT

The advanced electron paramagnetic resonance (EPR) techniques, electron nuclear double resonance (ENDOR) and electron spin echo envelope modulation (ESEEM) spectroscopies, provide unique insights into the structure, coordination chemistry, and biochemical mechanism of nature's widely distributed iron–sulfur cluster (FeS) proteins. This review describes the ENDOR and ESEEM techniques and then provides a series of case studies on their application to a wide variety of FeS proteins including ferredoxins, nitrogenase, and radical SAM enzymes. This article is part of a Special Issue entitled: Fe/S proteins: Analysis, structure, function, biogenesis and diseases.

© 2015 Elsevier B.V. All rights reserved.

## 1. Introduction

Iron–sulfur proteins share an important history with paramagnetic resonance techniques. Indeed, FeS proteins were first identified by Helmut Beinert with the use of electron paramagnetic resonance (EPR) spectroscopy [1–4]. This review will assume some familiarity with the basics of EPR, and will thus focus on the advanced EPR techniques, electron nuclear double resonance (ENDOR) and electron spin echo envelope modulation (ESEEM) spectroscopies, and their contributions towards extending our understanding of the roles played by FeS proteins. These spectroscopic techniques were invented roughly concurrently with the discovery of FeS proteins (i.e., late 1950s–early 1960s) [3–6], and ENDOR was applied to two-iron ferredoxins (2Fe-Fds) not long thereafter [7,8].

This review first provides an overview of the multiple forms in which ENDOR and ESEEM spectroscopies are currently practiced, and then describes in detail specific cases where these techniques have yielded important insights into the structure and biochemical action of iron–sulfur proteins. The emphasis is on more recent work; however, as appropriate we will detail studies that, beginning in the 1980s,

initiated the application of these techniques to FeS proteins, and that provide the foundation for recent studies.

The techniques of ENDOR and ESEEM spectroscopies aid in the understanding of various characteristics of metal ions and FeS clusters in biology such as: electronic and magnetic properties, enzyme mechanism, structure (coordination geometry, valence, and ligand identification with or without substrate/product/inhibitors) and protein dynamics. EPR spectra of metalloproteins are often too broad to resolve the interactions that contain the desired biochemical and physical information. In these cases, ENDOR and ESEEM spectroscopies provide this information at significantly higher resolution than from EPR alone.

The interactions of a metalloprotein's unpaired electron spin(s) ( $S$ ) and a nuclear spin ( $I$ ), are measured by their hyperfine couplings, denoted  $A$ . A large number of biochemically relevant nuclei have non-zero nuclear spin ( $I > 0$ ) with examples arising from amino acid residues, cofactors, or substrates/inhibitors including naturally abundant isotopes such as:  $^1\text{H}$ ,  $^{14}\text{N}$ ,  $^{19}\text{F}$ ,  $^{31}\text{P}$ , and those requiring isotopic enrichment such as:  $^2\text{H}$  (D),  $^{13}\text{C}$ ,  $^{15}\text{N}$ ,  $^{17}\text{O}$ , and  $^{33}\text{S}$ . Many metallic elements have non-zero spin isotopes of which  $^{57}\text{Fe}$  ( $I = 1/2$ , 2.2% abundance) is the most relevant here. For larger hyperfine couplings, or interactions where the intrinsic linewidth of the EPR spectrum is narrow, these electron–nuclear interactions can be directly observed in the EPR spectrum. An example is the observation of hyperfine coupling from  $^{63,65}\text{Cu}$  ( $I = 3/2$ , together 100% abundance) in Type II copper centers, and even in this case, the coupling is resolved only in the  $g_{\parallel}$  region. More often than not, and in particular in the case of iron–sulfur proteins, the EPR linewidth of

<sup>☆</sup> This article is part of a Special Issue entitled: Fe/S proteins: Analysis, structure, function, biogenesis and diseases.

E-mail address: [bmh@northwestern.edu](mailto:bmh@northwestern.edu) (B.M. Hoffman).

<sup>1</sup> Permanent address.

## Abbreviations

### Spectroscopic terms

CW	continuous wave
EPR	electron paramagnetic resonance
ENDOR	electron nuclear double resonance
ESEEM	electron spin echo envelope modulation
hfc	hyperfine coupling
HYSCORE	hyperfine sublevel correlation
PESTRE	Pulsed ENDOR Saturation and Recovery
RF	radiofrequency

### Biochemical terms

Aae	<i>Aquifex aeolicus</i>
AdoMet/SAM	S-adenosylmethionine
BioB/BS	Biotin synthase
CoM	coenzyme M, mercaptoethane sulfonate
CoB	coenzyme B, 7-mercaptoheptanoyl-L-threonine phosphate
Fd	ferredoxin
FeMo-co	iron molybdenum cofactor of nitrogenase
FeS	iron-sulfur
5'-GTP	guanosine 5'-triphosphate
Hdr	heterodisulfide reductase
HiPIP	high potential iron-sulfur protein
HMBPP	(E)-4-hydroxy-3-methyl-but-2-enyl diphosphate
5'-ITP	inosine 5'-triphosphate
MDTB	9-mercaptodethiobiotin
MEcPP	2-C-methyl-D-erythritol-2,4-cyclodiphosphate
MiaB,RimO	Radical S-adenosyl methionine methylthiotransferase (MTTase) enzymes
MoaA	Molybdenum cofactor biosynthetic enzyme
PFL-AE	Pyruvate formate lyase-activating enzyme

metalloprotein centers is sufficiently broad that small but important electron–nuclear hyperfine couplings are unresolved. To determine these hyperfine couplings and identify the nuclei of origin requires ENDOR and ESEEM spectroscopies, which will be described in the next section. The hyperfine information gained may identify nuclei within the coordination sphere, characterize bonding structure, determine bond order, and estimate electron–nuclear spin distances. These complementary advanced EPR techniques each are capable of resolving hyperfine couplings; whereas ENDOR spectroscopy is able to detect a wide range of hyperfine couplings, from as little as  $\sim 10^{-1}$  MHz up to  $>10^2$  MHz, ESEEM techniques are typically limited to smaller hyperfine values,  $A < 10$  MHz. Each technique can identify the nuclei present with ENDOR having the advantage of being broad-banded, but ESEEM spectroscopy has the advantage of being able to ‘count’ the number of equivalent nuclei (as in NMR).

## 2. Techniques

### 2.1. EPR

The electronic paramagnetic resonance (EPR) spectrum provides the first information associated with the FeS center: its electronic spin state ( $S \geq 1/2$ , with  $S = 1/2$  and  $3/2$  being the most amenable to study), iron d orbital configuration, FeS cluster oxidation state, and general molecular framework of the FeS cluster are established, and described in more detail elsewhere [9–11]. This information arises from the associated electron energy levels and their interaction with an externally applied magnetic field. In recording an EPR spectrum, the magnetic field,  $\mathbf{B}$ , is swept while a microwave field of fixed energy ( $E = h\nu$ ;  $\nu$  = frequency; typically  $\sim 9$  GHz (X-band) or 35 GHz (Q-band)), is applied, and

resonant transitions occur at field positions characteristic to the electronic structure, which are described in terms of a  $\mathbf{g}$  tensor (or matrix). In general, the three components of the  $\mathbf{g}$  tensor (typically,  $g_x, g_y, g_z$ , or, if one is reluctant to choose a geometrical designation,  $g_1, g_2, g_3$ , or  $g_{\min}, g_{\text{mid}}, g_{\max}$ ) depend on the electronic structure, electron spin interactions, and the relative orientation of the molecule within the magnetic field. The individual  $g$  values that make up the  $\mathbf{g}$  tensor may be viewed as deviations of the unpaired electron(s) from that of a ‘true’ free electron without any other interactions, which is  $g_e = 2.00232\dots$ . These deviations result from the orbital aspects of the unpaired electron(s), which interact with the spin aspects of the electron. As the number of electrons in the paramagnetic center increases, these spin-orbital interactions increase, and are thus more significant for FeS clusters (i.e., paramagnetic 3d ions) than for, say, organic radical species (paramagnetic 2s, 2p molecules).

### 2.2. ENDOR

The paramagnetic centers of FeS clusters in nature create unique spectroscopic probes for both electronic and structural coordination characterization by EPR (discussed in detail elsewhere in this special issue) and electron nuclear double resonance (ENDOR) spectroscopies [4,12–16]. In principle, any system with non-zero electron spin,  $S > 0$ , not only Kramers ( $S$  half-integer) but also non-Kramers states ( $S$  integer), can be EPR active and give advanced paramagnetic resonance responses. However, we focus here on what is perhaps the most common spin state in FeS proteins, and which is by far the most amenable to study by EPR and advanced techniques, namely  $S = 1/2$ . This unpaired electron spin of the FeS center paired with either its own iron nuclear spin(s), with spins of nuclei within the coordination sphere and of substrates/products/inhibitors allow one to generate a wealth of information for the FeS center. First, the electronic information of the iron ions may be determined through ENDOR hyperfine measurements of the  $^{57}\text{Fe}$  nuclei [17–20]. This sole magnetically active isotope of iron is present in only 2.15% natural abundance, and thus, isotopic enrichment in  $^{57}\text{Fe}$  is usually desirable [1,2]. Secondly, one may answer the question of what atoms, either through natural abundance or isotopic labeling, are within the first and second coordination sphere of the FeS cluster. These include isotopes such as  $^1\text{H}$ ,  $^{13}\text{C}$ ,  $^{15}\text{N}$ ,  $^{19}\text{F}$ ,  $^{31}\text{P}$ ,  $^{57}\text{Fe}$  (all  $I = 1/2$ ),  $^2\text{H}$ ,  $^{14}\text{N}$  (both  $I = 1$ ),  $^{33}\text{S}$  ( $I = 3/2$ ), and  $^{17}\text{O}$ ,  $^{95,97}\text{Mo}$  (all  $I = 5/2$ ).

While the EPR spectrum provides us with much preliminary information, including an orientation frame with which to view our molecule, much of the information desired, namely the electron–nuclear hyperfine and quadrupole interactions are small in energy and thus unresolved within the broad linewidth of the FeS cluster’s EPR spectrum. ENDOR spectroscopy, by virtue of the higher resolution and lower energy scale of the NMR experiment, directly measures these interactions governed by the nuclear spin Hamiltonian,  $H_N$ :

$$H_N = \underbrace{g_N \beta_N I \cdot \mathbf{B}}_{\text{nuclear Zeeman}} + \underbrace{S \cdot \mathbf{A} \cdot I}_{\text{hyperfine}} + \underbrace{I \cdot \mathbf{P} \cdot I}_{\text{quadrupole}} \quad (1)$$

where  $\beta_N$  is the Bohr magneton, which is a constant for all nuclei,  $g_N$  is the nuclear  $g$  value, unique to each isotope,  $I$  is the isotope’s nuclear spin, and  $\mathbf{B}$  is the magnetic field. The orientation dependent hyperfine interaction,  $\mathbf{A}$ , depends on the electronic spin,  $S$ , and the nuclear spin of the isotope being measured,  $I$ . For a given  $S$ , the quantized spin angular momentum levels are:  $M_S = [-S, (-S + 1), \dots, 0, \dots, (S - 1), S]$ , with an analogous situation for  $I$  ( $M_I = [-I, (-I + 1), \dots, 0, \dots, (I - 1), I]$ ). Allowed EPR transitions involve a change in electronic spin level:  $\Delta M_S = \pm 1$ ,  $\Delta M_I = 0$ , while ENDOR (i.e., NMR) transitions are:  $\Delta M_S = 0$ ,  $\Delta M_I = \pm 1$ . Fig. 1 outlines the allowed EPR and ENDOR transitions of an  $S = 1/2$ ,  $I = 1/2$  system, where solid lines  $a$  and  $b$  satisfy the  $\Delta M_S = \pm 1$ ,  $\Delta M_I = 0$  selection rule for EPR, while solid lines  $c$  and  $d$  satisfy the selection rules  $\Delta M_S = 0$ ,  $\Delta M_I = \pm 1$  for ENDOR spectroscopy. Lines  $e$  and  $f$  are  $\Delta M_S = \pm 1$ ,  $\Delta M_I = 1$  forbidden EPR transitions.

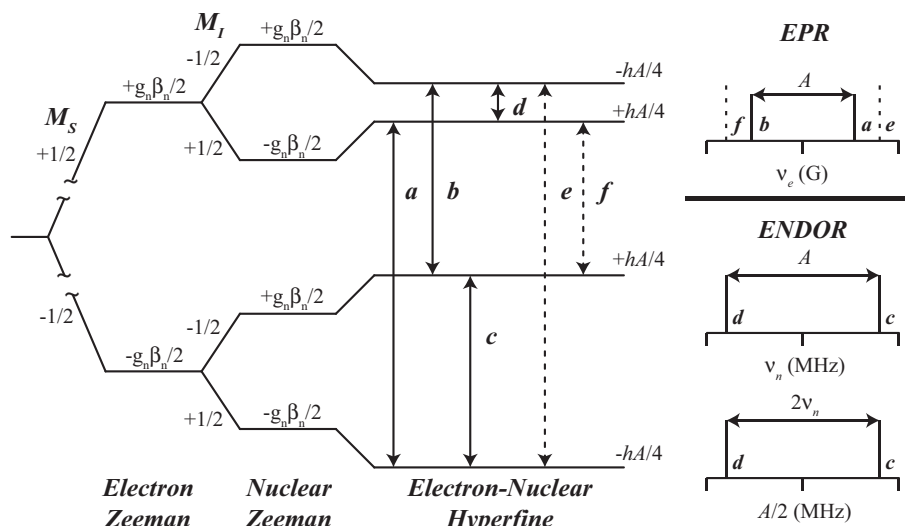


**Fig. 1.** Energy level diagram derived from the nuclear spin Hamiltonian (Eq. (1)) for an  $S = 1/2, I = 1/2$  system. Solid lines represent allowed EPR ( $a, b$ ) and ENDOR/ESEEM ( $c, d$ ) transitions and dashed lines represent forbidden EPR ( $e, f$ ) transitions. The stick representations (right) display the transition observed for EPR spectra (top) and for ENDOR spectra in ‘weak’  $\nu_n$  centered (middle) and ‘strong’  $A/2$  centered (bottom) coupling patterns.

ENDOR spectra are collected at static magnetic fields, each field defining a single EPR resonance among all possible, fixing the nuclear Zeeman portion of the nuclear Hamiltonian. Nuclei at this fixed magnetic field will resonate at a Larmor frequency,  $\nu_N$ , determined by:  $h\nu_N = g_N \beta_N \mathbf{B}$ , which scales with magnetic field,  $\mathbf{B}$ . An unpaired electron spin creates an large internal field that perturbs any nearby magnetically active nuclear spins, much like the significantly smaller internal field interactions between nuclear spins created in traditional NMR experiments measured by their chemical shift. Just as a 500 MHz  $^1\text{H}$  NMR spectrum measures the deviation of protons from their Larmor frequency,  $\nu_N$  ( $^1\text{H}$ ) = 500 MHz, at a magnetic field of 120 kG (12 T), ENDOR will measure proton interactions with large electronic spins which increases the internal magnetic field felt by the surrounding nuclear spins [16]. For ENDOR, this internal field is measured as a hyperfine coupling interaction tensor,  $\mathbf{A}$ . The observed ENDOR transitions may appear as Larmor centered,  $\nu_N$ , split by the hyperfine coupling,  $A$ , when the internal field is smaller than the external field:  $\nu_N > A/2$  – or – when the internal field is larger than external field:  $\nu_N < A/2$ , the transitions with appear centered at half of the hyperfine coupling and split by  $2\nu_N$ . These two possibilities are given by the following (first-order) equation:

$$\nu_{\pm} = \left| \nu_n \pm \frac{A}{2} \right|. \quad (2)$$

The right panel of Fig. 1 explores the ‘weak’ Larmor-centered and ‘strong’  $A/2$ -centered hyperfine coupling patterns for an  $S = 1/2, I = 1/2$  spin system – the simplest ENDOR-active spin system.

The hyperfine coupling (hfc),  $A$ , interaction for a particular nucleus contains a wealth of information. This is because hfc is related to electron spin delocalization onto a given nucleus, and hence, bonding information, geometry, and structural information. The matrix,  $\mathbf{A}$ , can thus be decomposed into two components:  $\mathbf{A} = A_{\text{loc}} + T$ . The first component,  $A_{\text{loc}}$ , is the local contribution to the observed hyperfine coupling and it depends on the nuclear properties of the nucleus observed. Various interactions of this nucleus with the electron spin are ‘contained’ within  $A_{\text{loc}}$ , including covalent bonding interactions and isotropic hyperfine coupling arising in general from electron spin density in s-orbitals at the nucleus. Ideally, the collection of  $A_{\text{loc}}$  of all nuclei for a metalcenter yields a complete composition of the covalent bonding network electron spin in the first coordination sphere. For the atoms involved in the ‘covalent’ bonded network, in-depth analysis of  $A_{\text{loc}}$  can yield rich

inorganic information, such as: *i*) valency of the metal ions [21], *ii*) covalency of the ligands [22] and *iii*) the coordination geometry of the metalcenter. The second term,  $T$ , garners the non-local, dipolar coupling information of atoms near the metalcenter, covalently bonded or not. Dipolar couplings allow for distance estimates between the nuclear and electron spin, and other geometric constraints such as angles and coordinates [14,23].

Atoms of nuclear spin  $I \geq 1$  possess a non-spherical atomic nucleus and are referred to as quadrupolar nuclei. In contrast to nuclei with  $I = 1/2$ , for which the  $M_I = \pm 1/2$  values are equal in energy (degenerate) in the absence of an external magnetic field, regardless of their electronic environment, nuclei with, e.g.,  $I = 1$  (as in  $^{14}\text{N}$ ) have  $M_I = 0, \pm 1$  levels, which may have differing nuclear energy magnitudes, even in the absence of external magnetic field [9]. All that is required is an internal electric field gradient, which can result from an unequal charge distribution around the quadrupolar nucleus, which could be the consequence of an imbalance of p orbital valence electrons about the nucleus [24]. This ‘charge distribution’ is measured and observed as an additional splitting of the ENDOR transitions described above. In this case of quadrupolar splitting, denoted as  $P$  (or sometimes  $Q$ ), each ENDOR peak is further split by the quadrupole moment into  $2I$  lines dictated by the following (first-order) equation:

$$\nu_{\pm}(M_I) = \left| \nu_N \pm \frac{A}{2} \pm \frac{3P(2M_I - 1)}{2} \right| \quad (3)$$

applicable when the quadrupole splitting is much smaller than the hyperfine [9]. For an  $S = 1/2, I = 1$  system, the same ENDOR selection rules,  $\Delta M_S = 0, \Delta M_I = \pm 1$ , still apply, however, the possible splitting pattern is now more complex, as seen in Fig. 2. For an axial quadrupole tensor,  $\mathbf{P} = [-P_x/2, -P_y/2, P_z]$ , the allowed ENDOR transitions are as follows:  $e$  and  $f$  of the  $M_S = +1/2$  manifold, and  $d$  and  $g$  of the  $M_S = -1/2$  manifold. The hyperfine can once again be in a ‘weak’ or ‘strong’ coupling regime as described earlier, however, for each, the observed quadrupole splitting is the same,  $3P$  (Fig. 2). The quadrupole coupling information thus obtained can be extremely powerful in determining bonding information and bond order, critical for distinguishing e.g.,  $sp^2$  imidazole nitrogens from other protein nitrogenous species [24,25].

Many of the FeS protein samples studied by EPR and ENDOR spectroscopy are in a frozen solution and therefore are a random distribution of all possible orientations in the magnetic or lab frame, hence the

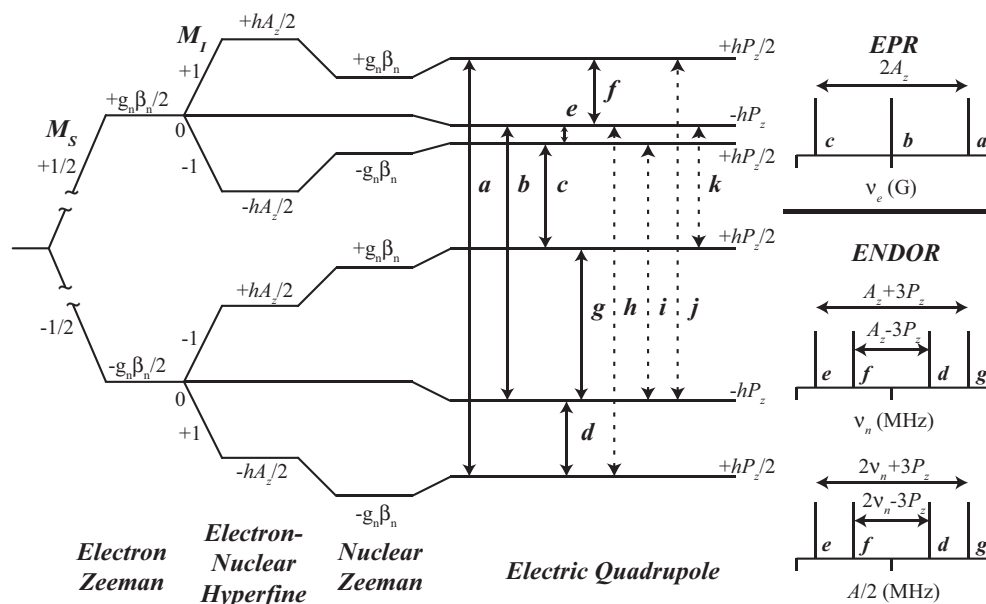


**Fig. 2.** Energy level diagram derived from the nuclear spin Hamiltonian (Eq. (1)) for an  $S = 1/2, I = 1$  system with an axial quadrupole tensor along the  $z$  axis. Solid lines represent allowed EPR ( $a, b, c$ ) and ENDOR/ESEEM ( $d, e, f, g$ ) and dashed lines represent semi-forbidden ESEEM ( $h, i, j, k$ ) transitions.

probability distribution of the field to align with any given orientation is equivalent. As each of the hyperfine,  $A$ , and quadrupole,  $P$ , tensors are orientation dependent, the deconvolution and mapping of complete tensors onto the electronic  $g$  tensor is performed through analysis of 2D field-frequency ENDOR spectra [16,26–29]. ENDOR spectra collected at the magnetic field edges of the rhombic EPR spectrum typically resemble a ‘single-crystal-like’ position, therefore one is observing only a single map of the  $A$  and  $P$  tensors along a single axis of the  $g$  tensor. ENDOR spectra of the 2D field-frequency between these field edges represent a mathematical subset of orientations of hyperfine and quadrupole. Through the correspondence of magnetic field ( $g$  values) and angular section, the absolute values and orientations of each  $A$  and  $P$  may be mapped onto the relative molecular frame provided by the  $g$  tensor.

ENDOR spectra may be collected with ‘continuous-wave’ (CW) microwave instrumentation by holding the magnetic field static while sweeping an applied radiofrequency (RF). The classic CW method for ENDOR acquisition involves field modulation and phase-sensitive detection with an RF sweep, and has superior sensitivity to the currently more popular pulsed ENDOR techniques [14]. However, pulsed ENDOR techniques frequently are able to give better-resolved ENDOR line shapes, and to resolve weaker hyperfine couplings [30,31].

Pulsed ENDOR techniques consist of microwave pulse sequences with the incorporation of RF pulses. There are two fundamental pulsed ENDOR techniques, named after their inventors, Mims [6] and Davies [32], respectively. The Mims ENDOR pulse sequence is based on the three-pulse (each  $90^\circ$  pulse is represented by  $\pi/2$  in the sequence) stimulated electron spin echo (ESE) sequence:  $\pi/2-\tau-\pi/2-T-\pi/2-\tau$ -echo (Fig. 3). To achieve ENDOR, an RF pulse is applied during time  $T$ . The Mims sequence can be used for large couplings but is most useful for resolving small hyperfine couplings, generally less than 4 MHz. Its sensitivity is a joint function of the hyperfine coupling being interrogated,  $A$ , and the interval,  $\tau$ :

$$\text{ENDOR} \propto (1 - \cos(\pi A \tau)) / 2. \quad (4)$$

The Mims ENDOR sequence thus is affected by ‘blind spots’ (i.e., points at which the S/N is essentially zero), when  $A = n/\tau$ , where  $n = 0, 1, \dots$ , integer [33].

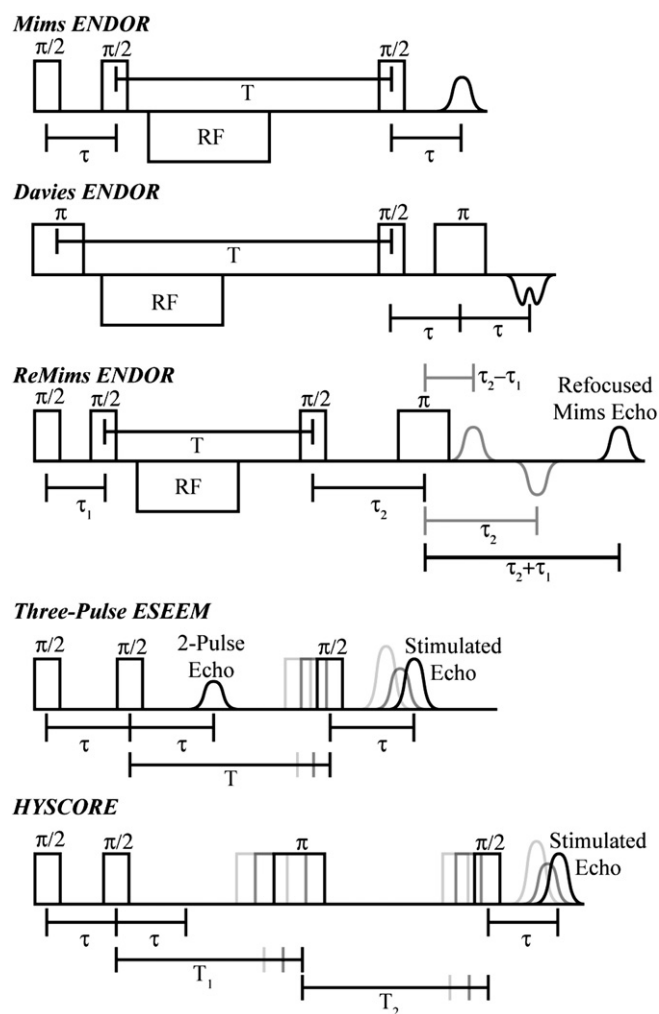


**Fig. 3.** Schematic representations of the Mims, Davies, and ReMims ENDOR pulse sequences, the three pulse ESEEM sequences, and the hyperfine sublevel correlation (HYSOCORE) pulse sequence.

The presence of blind spots can sometimes be advantageous as they can allow suppression of signals with specific hyperfine coupling, potentially simplifying spectra [33]. The first two ‘non-selective’ microwave pulses of the stimulated pulse sequence are responsible for the holes created in Mims ENDOR as the  $\pi/2-\tau-\pi/2$  sequence creates a ‘polarization grating’ within the inhomogeneous EPR line where the ENDOR is detected [34].

For larger hyperfine couplings, generally greater than 4 MHz, the Davies ENDOR sequence,  $\pi-T-\pi/2-\tau-\pi-\tau$ -echo, where the RF is applied once again at time  $T$ , is employed (Fig. 3) [32]. The preparation microwave  $\pi$  pulse is first applied to ‘flip’ the electron spin and then the RF pulse is applied during time  $T$  to then excite and mix nuclear transitions that match the RF pulse frequency. A Hahn echo sequence (i.e., the originally invented ESE sequence; described in more detail in the ESEEM section below):  $\pi/2-\tau-\pi-\tau$ -echo, is then applied and directly detects the NMR polarization of the EPR transition created by the RF pulse, yielding the ENDOR measurement. In contrast to the Mims pulse sequence; the Davies ENDOR detection is described by the function [33,35],

$$\text{ENDOR} \left( A \text{ (MHz)}, t_p \text{ (\mu s)} \right) \propto \frac{1.4 \left( t_p \right)}{0.7^2 + \left( A t_p \right)^2} \quad (5)$$

where  $t_p$  is the separation in time between the first two pulses. For the Davies ENDOR response, the ‘hole in the middle,’ appears as  $A$  goes to zero, but otherwise the ENDOR response does not have ‘blind spots’.

These two pulse sequences have set the foundation for development of additional techniques. The Remote-Echo Mims (ReMims) ‘four-pulse’ sequence (Fig. 3) developed by Doan allows for the collection of distortion-free ENDOR spectra of nuclei with hyperfine coupling greater than typically obtainable by the Mims pulse sequence, and is useful to bridge the gap in hyperfine coupling between traditional Mims and Davies ENDOR methods [36].

Another pulsed ENDOR ‘trick’ for deconvolution of ENDOR spectra and to ease the process of assignments of overlapping peaks is the employment of TRIPLE spectroscopy (where TRIPLE is not an acronym for anything and is sometimes referred to as *double ENDOR*) [34,37]. As it is considered a ‘pump-probe’ technique, the TRIPLE technique may be able to resolve and confirm nuclei hyperfine coupling assignments. A second ‘pump’ RF pulse of a constant frequency is added before the variable ‘probe’ RF pulse of the ENDOR pulse sequence. When the pump frequency matches a ENDOR transition of a  $\nu_+$  transition of a given nuclei, for example, the irradiation will cause an intensity change of the  $\nu_-$  transition, correlating the  $\nu_-/\nu_+$  pair for a single hyperfine coupling.

Relative signs of a hyperfine tensor for individual nuclei can sometimes be found through the analysis and simulation of 2D field-frequency ENDOR patterns, when a through-space dipole interaction gives a reference sign (e.g. [38,39]). Likewise TRIPLE can sometimes be used to determine relative hyperfine signs of multiple nuclei in a system through the so-called implicit TRIPLE effect [40]. First established on the low-spin  $\text{Fe}^{\text{III}}$  ( $S = 1/2$ ) center of the non-heme enzyme nitrile hydratase [40], the implicit TRIPLE effect has been extended to FeS clusters [41]. Whereas the determination of relative  $^{57}\text{Fe}$  hyperfine coupling signs has been well established in ENDOR, recently multi-pulse sequences have been developed to obtain absolute sign information, starting with the work of Bennebroek and Schmidt [42–44]. Most recently, a robust and reliable multi-pulse sequence has been developed by Doan, the Pulsed ENDOR Saturation Recovery (PESTRE) protocol, which determines absolute signs of hyperfine couplings in conjunction with corresponding ENDOR measurements, described below [45,46]. No longer does the assignment of absolute signs of  $^{57}\text{Fe}$  hyperfine couplings of FeS clusters depend solely on high field Mössbauer measurements [20].

### 2.3. ESEEM

Electron spin echo envelope modulation spectroscopy (ESEEM) [47–49] is a microwave-only pulsed technique that has the ability to resolve small hyperfine and quadrupole couplings that may not be resolved using other advanced techniques such as ENDOR spectroscopy, and has the experimental advantage of simplicity as no separate RF equipment is required, unlike for ENDOR [50]. ESEEM, as the name implies, employs the detection of a spin echo by a two pulse (primary echo),  $\pi/2-\tau-\pi-\tau$ -echo, or a three pulse (stimulated echo) sequence, described later. The basic two pulse sequence, often employed for ‘electron-spin-echo-detected’ EPR spectra, will create what is also often referred to as a Hahn spin echo [51]. After the  $\pi/2$  pulse flips electron spins into the orthogonal plane of the magnetic field vector, the electron spins dephase at a relaxation rate,  $T_{1e}$ , characteristic of the electron spin system. For transition metal ions at temperatures below 10 K, typical  $T_{1e}$  times are on the order of 10  $\mu\text{s}$ . The electron spin is allowed to ‘dephase’ during a time  $\tau$  before it is flipped again by  $\pi$ . The electron spin has memory and will begin to ‘rephase’ much like the previous ‘dephasing’ but now in the opposite axis direction so as to develop an echo which appears at the same time interval for the original dephasing,  $\tau$ . By varying  $\tau$ , the ‘dephasing’ behavior of the electron spin is detected.

As in ENDOR, the electron and nuclear Zeeman effects dominate the spectrum and will dominate the electron spin echo’s intensity. However, electron–nuclear hyperfine and quadrupole interactions also contribute to the echo intensity, and they are better exploited by varying  $\tau$  over a series of applied pulse sequences. When  $\tau$  is varied, the echo intensity of each pulse sequence of a given step in time,  $\tau$ , is measured, forming a time-domain spectrum. Primarily, the phase memory of the system is observed as exponential decay of the echo intensity as  $\tau$  increases. Of central interest, periodic modulation(s) of the electron spin echo by nuclear interactions appear within the time domain spectrum. This modulation created by nuclear hyperfine and/or quadrupole transitions is of central interest in the ESEEM experiment, therefore deeper modulation is desired for increased S/N. The relaxation decay of the echo is subtracted from the time domain spectrum followed by subsequent processing (windowing, zero filling, etc. – the same “tricks” as used in FT-NMR) before the final Fourier transform that yields a frequency domain spectrum for easier observation of the hyperfine and quadrupole couplings.

ESEEM spectroscopy has the advantage over ENDOR spectroscopy of being able to quantify the nuclear modulation depth so as to ‘count’ similar nuclei, provided they have similar hyperfine and quadrupole coupling parameters [25]. In contrast, ENDOR signal intensities are difficult to correlate with number of nuclei. For example, this quantitative ability of ESEEM has been extremely useful in the determining the number of imidazole ligands of a given metalcenter [25].

The transitions observed in ESEEM vary slightly from those of ENDOR. As ENDOR spectroscopy follows its selection rules more rigorously, ESEEM techniques exploit both allowed and ‘semi-forbidden’ transitions [34]. For  $S = 1/2$ ,  $I = 1/2$  cases, maximum modulation depth within the ESEEM time-domain spectrum is obtained when the microwave energy ‘matches’ the Hamiltonian energy (Eq. (1)), taking into specific consideration the second and third terms, the hyperfine and quadrupole interactions, respectively. ESEEM transitions observed for  $I = 1/2$  nuclei are a result of only the anisotropic portion of the hyperfine tensor (primarily  $T$ ; see definition for  $\mathbf{A}$  given above). Many anisotropic nuclei that may be of interest, e.g.,  $^1\text{H}$  couplings of metal-bound  $^1\text{H}_2\text{O}$  species, have very broad lines, so that the modulation is frequently lost within the dead time of the instrument, making ESEEM of  $I = 1/2$  systems often difficult [50]. However,  $^{15}\text{N}$  ( $I = 1/2$ ) isotopic labeling can be useful for analyzing weaker  $^{14}\text{N}$  couplings, because the  $^{15}\text{N}$  ESEEM can yield a more direct estimate of the dipolar contribution, which can then be used in interpreting the  $^{14}\text{N}$  ESEEM data, which contain isotropic and quadrupole couplings, as discussed next.

For  $S = 1/2$ ,  $I = 1$  cases, frequently histidine  $^{14}\text{N}$  systems at X-band ( $\sim 9.5$  GHz), the quadrupole term now plays a significant role [25]. The off-diagonal matrix elements introduced by the rhombic quadrupole tensor allows for more significant mixing of the quantum states, and semi-forbidden  $\Delta M_I = \pm 2$ , double quantum, transitions to occur, such as  $h$ ,  $i$ ,  $j$ , and  $k$  in Fig. 2. The semi-forbidden transitions in Fig. 2 are combination differences between the allowed EPR and ENDOR transitions, creating unique observable transitions for the ESEEM experiment. In the opposite view, when both allowed EPR and semi-forbidden ESEEM transitions are excited in the ESEEM experiment, their frequencies will beat against each other and result in single transitions at the ENDOR frequencies, for example  $i$  (EPR)  $- h$  (semi-forbidden)  $= f$  (ENDOR).

Three-pulse ESEEM, which has the sequence:  $\pi/2 - \tau - \pi/2 - \Delta T - \pi/2 - \tau$ -echo (Fig. 3), is often simpler to analyze as it contains only the principal ENDOR (NMR) frequencies and semi-forbidden transitions, while lacking the sum and difference peaks of transitions observed in a two-pulse ESEEM experiment. While greater signal intensity is achieved with the three-pulse ESEEM sequence as compared to the two-pulse ESEEM sequence for disordered (frozen solution) systems, the main disadvantage of three-pulse ESEEM is the inclusion of 'blind-spots' as a function of  $\tau$ . These holes are caused by the same 'polarization grating',  $\pi/2 - \tau - \pi/2$ , of the stimulated echo as seen in the Mims ENDOR spectroscopy, however, the hole pattern has no dependence on  $A$ , only on  $\tau$ , therefore, multiple three pulse ESEEM spectra of varying  $\tau$  should be collected to ensure proper assignments.

#### 2.4. HYSORE

The development of three-pulse ESEEM techniques led to its extension into a two-dimensional form [52], much as what had occurred earlier in NMR spectroscopy. This 2D ESEEM is referred to as hyperfine sublevel correlation (HYSORE) spectroscopy, and is produced by the addition of a 'mixing pulse' to create a four-pulse ESEEM sequence [53]. While 3-pulse ESEEM works well for some disordered systems, it often loses much of the fast decaying modulation amplitude, quicker than the electron spin decay. This is much more of a problem for larger coupling with significant hyperfine anisotropy. Because of instrument dead time, most, if not all, of the nuclear modulation is often lost before data collection begins. The addition of a fourth  $\pi$  pulse to the three pulse sequence alleviates this problem by transferring nuclear spin coherence from one manifold to the other and prolonging the modulation decay time. The addition of this  $\pi$  pulse between the second and third  $\pi/2$  pulses of the three-pulse sequence,  $\pi/2 - \tau - \pi/2 - T_1 - \pi - T_2 - \pi/2 - \tau$ -echo (Fig. 3), creates two separate 'evolution' periods before and after the  $\pi$  pulse, termed  $T_1$  and  $T_2$ . The  $\pi$  pulse takes the nuclear coherence developed in the  $M_S = \pm 1/2$  electron manifold during the first evolution period,  $T_1$ , and mixes it between the electron spin manifolds. The nuclear spin coherence now evolves in the opposite  $M_S = \pm 1/2$  electron spin manifold, and a nuclear coherence transfer echo is created at  $T_1 = T_2$ . The nuclear coherence transfer echo is most easily observed in the frequency domain spectrum along the diagonal of  $T_1 = T_2$ . The last  $\pi/2$  pulse transfers the nuclear coherences to electron coherences for detection as an electron spin echo. The key aspect of the HYSORE experiment is that the final electron spin echo produced has been modulated by the nuclear spins, similar to the ESEEM experiment, however, the mixing pulse helps extend the electron spin relaxation decay time. For disordered (frozen solution) systems, HYSORE therefore has improved sensitivity relative to 2D three-pulse ESEEM spectroscopy.

The typical four-pulse ESEEM experiment is done in a 2D fashion (HYSORE) where  $T_1$  and  $T_2$  are incremented independently of each other and the final product therefore correlates the nuclear frequencies with the mixing of the electron spin manifolds. The 2D time domain spectrum is processed in a similar fashion as described earlier for ESEEM; a 2D Fourier transform results in four quadrants, where, as with ENDOR, two coupling regimes are possible, either a strong

( $A > \nu_N$ ) or weak coupling ( $\nu_N > A$ ) regime; however, all peaks are not observed in a single quadrant. For 'weak' couplings of powder samples, peaks are once again Larmor centered perpendicular to the frequency diagonal in the first (+,+) and third (-,-) quadrants. For stronger couplings, cross peaks appear in the second and fourth quadrants, occasionally labeled as (+,-) and (-,+), respectively. This process allows for the readout and interpretation of multiple nuclei in a single spectrum that may have been unmanageable in a single ESEEM experiment. The powder pattern responses do not easily translate to complete hyperfine and quadrupole tensors. Complete line shape analysis and simulations at multiple magnetic field positions is the only true way to fully resolve **A** and **P** tensor values and their respective orientation to **g**, reviewed extensively elsewhere [50,54–57].

HYSORE is most useful to resolve broad hyperfine lines that three-pulse ESEEM often fails to detect. The ability of HYSORE to detect large anisotropic couplings of  $I = 1/2$  nuclei such as  $^1\text{H}$  and  $^{13}\text{C}$  is a result of the added  $\pi$  mixing pulse, as these couplings are no longer lost through destructive interference which occurs in the three pulse experiment. Of course, HYSORE still retains 'blind-spots' with  $\tau$  time dependencies; therefore careful experimental and/or simulation considerations must be made.

#### 2.5. Advanced EPR techniques applied to non-Kramers (integer-spin) systems

The above description of ENDOR, ESEEM, and HYSORE techniques uses as examples the Kramers,  $S = 1/2$ , state the most common and spectrally rewarding of the possible spin states of FeS clusters. However, FeS clusters can also be found in higher spin states. Resting state nitrogenase has  $S = 3/2$ , and has been extensively studied by ENDOR as described elsewhere in this review and in other reviews [58–60]. For completeness it is useful to note that ENDOR and ESEEM can be productively applied to favorable integer spin states, primarily  $S \geq 2$ , which can be found in 3Fe-red clusters,  $[\text{Fe}_3\text{S}_4]^{10}$ , and has recently been identified in catalytic turnover states of nitrogenase [60–62]. It has been known for many years that integer-spin (non-Kramers) states having  $S \geq 2$  with negative zero-field splitting parameter  $D$  (so that the spin ground doublet is  $|S, \pm M_S\rangle = \pm S$ ) exhibit EPR spectra, generally at low fields [63, 64]. More recently, it was shown that ENDOR and ESEEM of such EPR signals can be highly informative [65–67].

### 3. Advanced EPR studies of FeS clusters in iron-sulfur and related proteins

This section describes advanced EPR studies that focus on the FeS cluster itself, using as probes primarily the Fe ions themselves (enriched in  $^{57}\text{Fe}$ ), but also  $^1\text{H}$  nuclei located on coordinated thiolates that directly provide information on their nearby Fe ion. As discussed subsequently the inorganic sulfides can also be studied upon enrichment in  $^{33}\text{S}$  ( $I = 3/2$ , 0.75% natural abundance). In the case of heterometallic clusters, such as in nitrogenase FeMo-co, other nuclei can be studied, such as  $^{95}\text{Mo}$  ( $I = 5/2$ , 15.9% natural abundance, and enriched) and the central ion of FeMo-co, now identified as a carbide, due in part to enrichment in  $^{13}\text{C}$  [68–70].

#### 3.1. $^{57}\text{Fe}$ ENDOR

It is of interest to note that  $^{57}\text{Fe}$  studies of FeS clusters not only initiated the use of ENDOR in characterizing metalloenzymes [7], but were the motivation [71] for the development of the theory and methodology for determining hyperfine interactions tensors through the simulation of 2D field-frequency patterns of ENDOR spectra collected across the EPR envelope of the center under study [16,26,27], as well as the development of the most robust method for determining hyperfine signs, PESTRE [45].

### 3.1.1. 2Fe-ferredoxins

The exchange coupling of the two iron spins,  $S = 2 \text{ Fe}^{\text{II}}$  and  $S = 5/2 \text{ Fe}^{\text{III}}$  ions, in an EPR observable reduced  $[2\text{Fe}2\text{S}]^+$  cluster result in either a ferromagnetically [72] coupled ground state, which yields a total spin,  $S = 9/2$ , or an antiferromagnetically coupled ground state, which gives  $S = 1/2$  [73]. The observed  $g$  tensor for the antiferromagnetically coupled state is given by

$$\mathbf{g} = \frac{7}{3}\mathbf{g}_{\text{III}} - \frac{4}{3}\mathbf{g}_{\text{II}} \quad (6)$$

where  $\mathbf{g}_{\text{III}}$  and  $\mathbf{g}_{\text{II}}$  are the individual  $g$  tensors of the ferric and ferrous centers, respectively. The low-spin  $S = 1/2$  ground state is more commonly observed for  $[2\text{Fe}2\text{S}]$  clusters. Fig. 4 presents Q-band (35 GHz) EPR spectra of three, representative FeS proteins with  $S = 1/2$  ground states, including  $[2\text{Fe}2\text{S}]^+$  cluster from *Aquifex aeolicus* Fd1 (Fig. 4A) which has a significantly rhombic signal with  $g$  values straddling 2.0

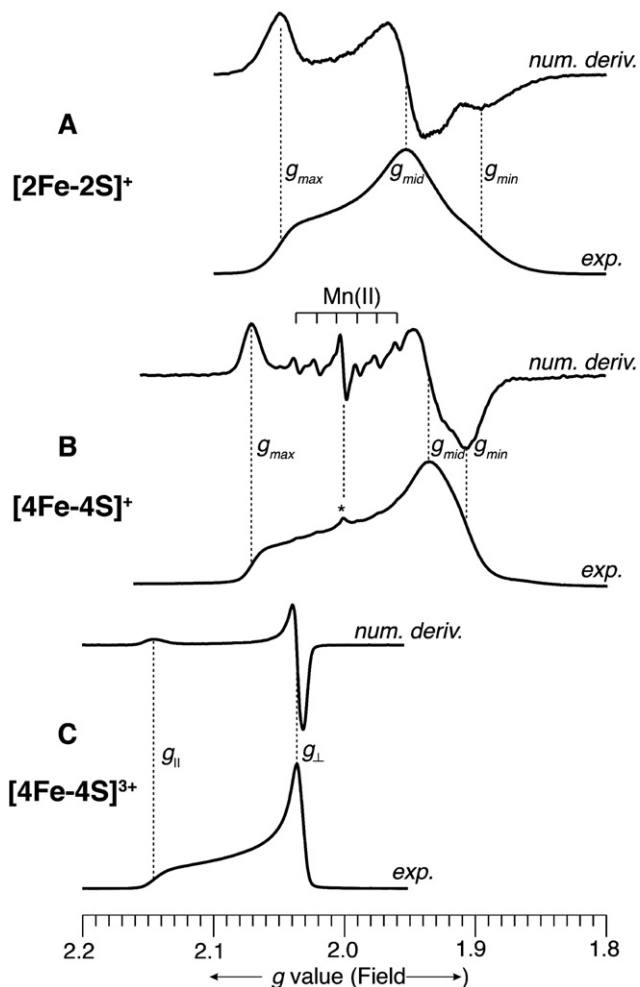


**Fig. 4.** Q-band (35 GHz) EPR spectra of three, representative FeS proteins. The spectra were all recorded at 2 K under “rapid passage” conditions, so that the experimental spectrum appears as an absorption lineshape. A digital derivative spectrum is displayed above each experimental spectrum, which gives the familiar presentation of EPR spectra. The intensities of all spectra have been arbitrarily scaled for ease of viewing. The abscissa is given in descending  $g$  value scale (corresponding to increasing magnetic field) to allow comparison among spectra recorded at slightly different microwave frequencies. The  $g$  values of the FeS clusters are indicated on each spectrum. A) *Aquifex aeolicus* Fd1 reduced 2Fe-Fd,  $[2\text{Fe}2\text{S}]^+$ , recorded at 35.028 GHz; B) *Desulfovibrio gigas* reduced 4Fe-Fd,  $[4\text{Fe}4\text{S}]^+$ , recorded at 34.946 GHz; In (B), the presence of a small amount of adventitious Mn(II), a common occurrence in metalloprotein samples, is indicated. This narrow line sextet ( $^{55}\text{Mn}$ ,  $I = 5/2$ , 100%) is accentuated in the derivative presentation. An unknown radical ( $g \approx 2.00$ ) is also present in very small amount and is indicated by an asterisk. C) *Halorhodospira halophila* (formerly *Ectothiorhodospira halophila*) oxidized HiPIP,  $[4\text{Fe}4\text{S}]^{3+}$ , recorded at 34.958 GHz.

( $g = [2.05, 1.95, 1.89]$ ,  $g_{\text{iso}} = 1.96$ ). The spectra were all recorded at 2 K under “rapid passage” conditions [74], so that the experimental spectrum appears as an absorption line shape. In addition, for each protein, a numerical derivative spectrum is also provided, which thus has the first derivative line shape of an EPR spectrum recorded under “slow passage” conditions, as is the case for typically reported spectra. Each format has advantages and disadvantages. The absorption lineshape is better for observation of broad lines and gives a better idea as to the actual amount of signal. The first derivative lineshape is better for observation of narrow lines. This can easily be seen in Fig. 4B, wherein the spectral signature of a small amount of adventitious Mn(II), which appears as a sextet due to hyperfine coupling to  $^{55}\text{Mn}$  ( $I = 5/2$ , 100%) is greatly accentuated in the numerical derivative presentation, even though the Mn(II) is actually present in very low concentration, as shown by the experimental, absorption lineshape, which is dominated by the much broader  $[4\text{Fe}4\text{S}]^+$  EPR signal.

Either of the  $S = 1/2$  or  $9/2$  paramagnetic states for  $[2\text{Fe}2\text{S}]^+$  clusters are amenable to ENDOR characterization of both the  $^{57}\text{Fe}$  centers and of coordinated ligands and other nearby molecules. Both  $^{57}\text{Fe}$  ENDOR and magnetic Mössbauer spectroscopies may characterize the electronic structure of the iron ions of a given FeS center [64,75]. Each technique has distinct advantages and disadvantages. As discussed elsewhere [13,14,20,76], Mössbauer is able to detect all Fe sites in a given sample, while ENDOR observes only those interacting with unpaired electron(s). This fact alone can lead to complementary information being provided by the two techniques. For example, Mössbauer is able to characterize the diamagnetic, reduced  $[2\text{Fe}2\text{S}]^0$   $S = 0$  ground state, inaccessible by ENDOR, as well as other paramagnetic, or integer-spin systems ( $S = 1, 2, \dots$ ), which are more difficult, but not impossible (vide supra) to study by EPR and ENDOR. However, Mössbauer may be overwhelmed when multiple FeS clusters reside within a protein, severely convoluting a spectrum. ENDOR, in contrast, has the advantage of being ‘blind’ to diamagnetic species and can select among paramagnetic FeS clusters whose EPR envelopes do not overlap. Indeed, the spin state selection of ENDOR plays a critical role in the study of some complex FeS systems. A more subtle distinction is that Mössbauer can determine  $^{57}\text{Fe}$  quadrupole splitting that is unattainable through ENDOR spectroscopy as this information arises from the nuclear excited state of  $^{57}\text{Fe}$  ( $I = 3/2$ ), accessed by the  $\gamma$ -ray energy employed by Mössbauer [77]. Traditionally, an advantage of Mössbauer is that it allowed determination of the sign of hyperfine couplings, along with their magnitudes, while such sign information was not obtainable from ENDOR. However, as discussed above, newly developed ENDOR protocols for determining absolute hyperfine signs [20,45,46] have “leveled the playing field” between the two techniques in this regard.

The  $g$  tensor for  $[2\text{Fe}2\text{S}]$  clusters may be used to classify clusters into families and determine electronic characteristics [20], however it is the  $^{57}\text{Fe}$  hyperfine couplings that provide the deepest insight into their electronic structure and ENDOR spectroscopy has the added advantage of being able to map the  $g$  tensor orientation onto the molecular frame.

The  $[2\text{Fe}2\text{S}]^+$  clusters from *A. aeolicus* (*Aae*) ferredoxins (Fd1, Fd5, and Fd5) are cysteine coordinated and belong to a  $g_{\text{iso}} = 1.96$  subclass of 2Fe ferredoxins [20]. By grouping  $[2\text{Fe}2\text{S}]$  proteins into subclasses of related electronic structure, various ligand-field energies may be determined from EPR parameters as shown recently for Fd1, Fd4, and Fd5 from *Aae*. Such  $[2\text{Fe}2\text{S}]^+$  clusters exhibit fairly isotropic  $\text{Fe}^{\text{III}}$  coupling, while the hyperfine coupling of the  $\text{Fe}^{\text{II}}$  ion is very anisotropic with its strongest hyperfine coupling along  $g_1$ . The constituent  $\text{Fe}^{\text{III}}$  ion in a  $[2\text{Fe}2\text{S}]^+$  cluster is relatively insensitive to its coordination environment, which is expected due to the spherical electron distribution of its high-spin  $d^5$  (half-filled) electronic configuration [18,20,78,79]. In contrast, the ligand field of the  $\text{Fe}^{\text{II}}$  ion is very sensitive to its coordination environment as a result of the unsymmetrical electron distribution of its high-spin  $d^6$  configuration. The differences in the average of  $g$  values for different classes of  $[2\text{Fe}2\text{S}]$  clusters reflect the environment of the  $\text{Fe}^{\text{II}}$  site [80]. The dictates the ligand field energy  $d^6$ ,  $\text{Fe}^{\text{II}}$  ion

controls the rhombic splitting of the cluster  $\mathbf{g}$  tensor, which is proportional to the mixing of pure  $d(z^2)^{(5A_1)}$  (axial compression) or  $d(x^2-y^2)^{(5B_1)}$  (axial elongation) states of  $\text{Fe}^{\text{II}}$  for  $D_{2d}$  symmetry. For  $g_{\text{iso}} = 1.96$  class of [2Fe2S] proteins, the various ligand-field energies of the  $\text{Fe}^{\text{II}}$  ion in its ground state may be determined from fitting the  $g$  values to a diagonalized energy matrix for two pure  $z^2$  and  $x^2-y^2$  states (diagonal terms) and the amount of rhombic crystal field mixing (off-diagonal terms) due to a rhombic crystal-field distortion ( $D_{2h} \rightarrow C_{2v}$ ). Thus, the plot of rhombic splitting versus canonical  $g$  values yields the ligand-field parameters for a given class of [2Fe2S] clusters. Fig. 5 presents a solution to Eqs. (6) and (8) with ligand-field parameters given in the figure caption.

$$\tan 2\eta = -\frac{2\varepsilon_{\text{mix}}}{\varepsilon_{z^2} - \varepsilon_{x^2-y^2}} \quad (7)$$

$$\begin{aligned} g_{\text{Iix}}(\eta) &= g_e - \frac{8\lambda}{\Delta E_{yz}} \sin^2\left(\eta + \frac{\pi}{3}\right) = g_e + \Delta g_{\text{Iix}}(\eta), \\ g_{\text{Iiy}}(\eta) &= g_e - \frac{8\lambda}{\Delta E_{xz}} \sin^2\left(\eta - \frac{\pi}{3}\right) = g_e + \Delta g_{\text{Iiy}}(\eta), \\ g_{\text{Iiz}}(\eta) &= g_e - \frac{8\lambda}{\Delta E_{xy}} \sin^2\eta = g_e + \Delta g_{\text{Iiz}}(\eta). \end{aligned} \quad (8)$$

The amount of orbital mixing is proportional to the rhombic splitting of  $\mathbf{g}$ ,  $\Delta g_{\perp} = g_3 - g_2$ , and is a function of the fictitious angle  $2\eta$  (Fig. 5) [20].

As the EPR spectrum is influenced by the symmetry of the FeS cluster, the same is obviously true for the iron hyperfine couplings. High precision ENDOR of the  $^{57}\text{Fe}$  hfc of Fd1, Fd4, and Fd5 from *Aae* reveal isotropic  $\text{Fe}^{\text{III}}$  hyperfine couplings, matching those previously established by Mössbauer spectroscopy. The  $\text{Fe}^{\text{II}}$  hyperfine couplings are vastly different for Fd1 and Fd5 which happen to be remarkably similar in structure. Further investigation of the slight differences in the structural, electronic, hyperfine properties of characterized ferredoxin proteins needs to be done to achieve a more general understanding of the mixed valent [2Fe-2S] cluster. Understanding of the simplest FeS cluster serves as a building block for understanding higher nuclearity FeS clusters.

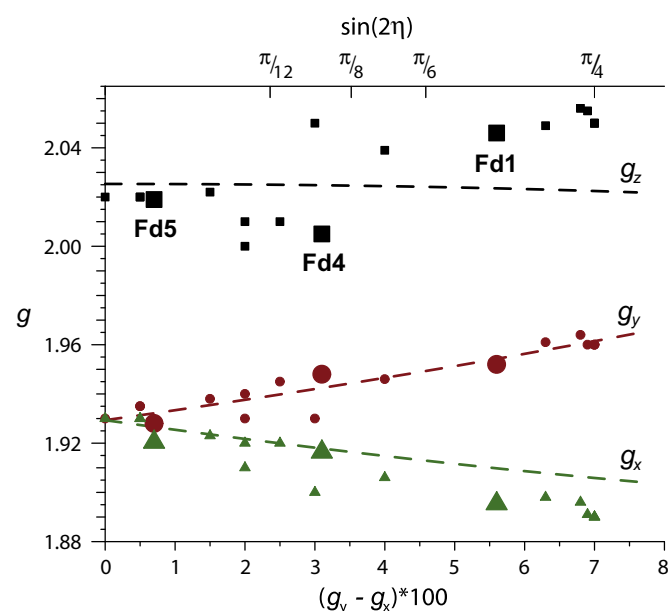


**Fig. 5.** 'Bertrand plot' of  $g$  tensor components against  $\Delta g_{\perp}$  ( $\times 100$ ) for various [2Fe-2S] proteins of the  $g_{\text{iso}} = 1.96$  subclass. Dashed lines represent values from Eqs. (6)–(8) calculated with the parameters  $\lambda = -60 \text{ cm}^{-1}$ ,  $\Delta E_{xy} = 15,000 \text{ cm}^{-1}$ ,  $\Delta E_{xz} = \Delta E_{yz} = 5000 \text{ cm}^{-1}$ ,  $g(^{57}\text{Fe}^{\text{III}}) = 2.01$ .

Reprinted from Fig. 5 of Cutsail et al. [20] with kind permission from Springer Science and Business Media © 2012 SBIC.

### 3.1.2. 4Fe-ferredoxin overview

Various oxidation states of [4Fe4S] clusters are observed, ranging from the 3+ state seen in oxidized high potential iron-sulfur protein (HiPIP-ox), to 2+, 1+, and 0. Only 3+,  $S = 1/2$ , and 1+,  $S = 1/2$  or  $S = 3/2$ , cluster oxidation states possess paramagnetic ground spin states and are amenable to typical advanced EPR spectroscopies [81–83]. The other, diamagnetic 2+,  $S = 0$ , and 0,  $S = 4$ , oxidation states may be observed through Mössbauer spectroscopy. The ground spin states are most conveniently explained by antiferromagnetic coupling of [2Fe2S] cluster pairs (the so-called 2–2 model), ( $[2\text{Fe}2\text{S}]^{2+}$ ,  $S = 5$ ;  $[2\text{Fe}2\text{S}]^+$ ,  $S = 9/2$ ;  $[2\text{Fe}2\text{S}]^0$ ,  $S = 4$ ) and the  $\text{Fe}^{\text{II}}$   $S = 2$  and/or  $\text{Fe}^{\text{III}}$   $S = 5/2$  ion(s). The common  $[4\text{Fe}4\text{S}]^{3+}$   $S = 1/2$  state is the result of an  $[2\text{Fe}2\text{S}]^+$  ( $\text{Fe}^{2.5}\text{-Fe}^{2.5}$ )  $S = 9/2$  pair antiferromagnetically coupled with two  $\text{Fe}^{\text{III}}$   $S = 5/2$  ions. The two electron reduced  $[4\text{Fe}4\text{S}]^+$  is composed also of an  $[2\text{Fe}2\text{S}]^+$  ( $\text{Fe}^{2.5}\text{-Fe}^{2.5}$ )  $S = 9/2$  pair however it is antiferromagnetically coupled with two  $\text{Fe}^{\text{II}}$   $S = 2$  ions [18,84]. Examples of an oxidized HiPIP [4Fe4S] $^{3+}$  and a reduced [4Fe4S] $^+$  are exhibited in Fig. 4. The oxidized HiPIP [4Fe4S] $^{3+}$  exhibits an axial, narrow linewidth signal, with  $g$  values above 2.0 ( $g_{\parallel} = 2.14$ ,  $g_{\perp} = 2.04$ ,  $g_{\text{iso}} = 2.07$ ) and the reduced 4Fe-Fe [4Fe4S] $^+$  has a broader linewidth, slightly rhombic signal with  $g$  values straddling 2.0 ( $\mathbf{g} = [2.07, 1.94, 1.91]$ ,  $g_{\text{iso}} = 1.97$ ). It should be noted, as can be seen by comparison of Fig. 4A and C, that it is essentially impossible to distinguish solely by EPR between 4Fe-red and 2Fe-red centers. As described below, the specific nature of the coupling can be variable and more intricate than indicated here.

### 3.1.3. 4Fe-ferredoxin models

The synthesis of small molecule model compounds of the active site center of ferredoxins and other FeS cluster species was a great achievement of inorganic chemistry that has been extensively reviewed elsewhere [85–87]. Of relevance here is the use made of several synthetic ferredoxins for detailed EPR and ENDOR studies by Gloux, Lamotte, Mouesca, and co-workers in Grenoble [18,88–93]. The synthetically accessible cluster,  $[\text{Fe}_4\text{S}_4(\text{SR})_4]^{2-}$  (where R = Ph ( $-\text{C}_6\text{H}_5$ ), Bz ( $-\text{CH}_2\text{C}_6\text{H}_5$ )) is diamagnetic and corresponds to the 4Fe-ox (or HiPIP-red) protein cluster forms. These workers were able to generate EPR active forms of the synthetic clusters by low-temperature  $\gamma$ -irradiation of single crystals, this process, which has also been used extensively with metalloproteins in frozen solution [94–96], generates free electrons which can then reduce the FeS center to generate  $[\text{Fe}_4\text{S}_4(\text{SR})_4]^{3-}$ , the analog to the 4Fe-red cluster. In addition, oxidized clusters,  $[\text{Fe}_4\text{S}_4(\text{SR})_4]^{1-}$ , can also be concurrently generated, analogous to the HiPIP-ox form. The different EPR signatures of these species allowed their deconvolution in single-crystal EPR spectra [90,92,97]. In these synthetic clusters, the only ENDOR active nucleus is  $^1\text{H}$ , with the methylene hydrogen atoms of the benzylthiolato (or related) ligands serving as models for the  $\beta$ -H atoms of cysteinyl ligands in FeS clusters [89,93]. Nevertheless,  $^1\text{H}$  ENDOR has provided a wealth of information on the electronic structure of these 4Fe4S model compounds. All eight  $^1\text{H}$  hyperfine tensors were fully determined for  $[\text{Fe}_4\text{S}_4(\text{SCH}_2\text{C}_6\text{D}_5)_4]^{1-}$ , wherein the benzene ring deuteration assisted in simplifying the  $^1\text{H}$  X-band ENDOR spectra. The results on hydrogen dipolar coupling and spin distribution within the cluster could be related to those from paramagnetic NMR and allowed a proposal to be made as to the specific spin coupling state, namely  $|S_{\text{mixed-valence}}, S_{\text{ferric}}, S_{\text{total}}\rangle = |7/2, 3, 1/2\rangle$ , as opposed to  $|9/2, 4, 1/2\rangle$  [89], (note that in some 2Fe-Fds,  $S_{\text{mixed-valence}} = S_{\text{ferric}} + S_{\text{ferrous}} = 5/2 + 2 = 9/2$ , and  $0 \leq S_{\text{ferric}} \leq 10 (+5/2 + 5/2)$ ). The same parent compound, in the reduced form generated by  $\gamma$ -irradiation was later studied by Q-band  $^1\text{H}$  ENDOR [98]. It was possible to determine the full hyperfine tensors of all eight benzyl methylene hydrogen atoms, plus three more tensors from  $^1\text{H}$  nuclei on adjacent molecules. Analogously to the earlier study, the spin distribution within the 4Fe-red model cluster was determined, including the spin projection onto each Fe ion, which is crucial for understanding hyperfine coupling to bound substrate in enzymatic FeS clusters. In this cluster, the spin coupling ground state was determined to be  $|S_{34}, S_{134}, S_{\text{total}}\rangle = |4, 2, 1/2\rangle$ ,



using the so-called ‘3–1’ scheme, wherein the three formally ferrous ions ( $\text{Fe}^{\text{II}}$ ,  $\text{Fe}^{\text{II}}$ , and  $\text{Fe}^{\text{II}}$ ) are coupled to give first  $S_{34}$  ( $0 \leq S_{34} \leq 4$ ; here 4) and then  $S_{134} = S_{34} - S_2 = 4 - 2$  in this case, which is then antiferromagnetically coupled to the ferric ion:  $S_{\text{total}} = S_{134} - S_2 = |4 - 5/2| = 1/2$ . An alternate, and widely used coupling scheme (vide supra), although considered less physically sound for  $[\text{Fe}_4\text{S}_4]^{3+}$  by Moriaud et al. [105], is the ‘2–2’ scheme which is analogous to that used above for  $[\text{Fe}_4\text{S}_4]^{3+}$ , namely,  $S_{\text{mixed-valence}} = S_{12} = 9/2$  (or lower) and  $S_{\text{ferrous}} = S_{34} = 4$  (or lower), with  $S_{\text{total}} = S_{12} - S_{34} = |9/2 - 4| = 1/2$ . Using the 2–2 model, the  $[\text{Fe}_4\text{S}_4(\text{SCH}_2\text{C}_6\text{H}_5)_4]^{3-}$ , is best represented as  $|S_{\text{mixed-valence}}, S_{\text{ferrous}}, S_{\text{total}}\rangle = |S_{12}, S_{34}, S_{\text{total}}\rangle = |7/2, 3, 1/2\rangle$ ; the spin coupling scheme analogous to that for the HiPIP-ox model cluster.

The Grenoble workers were also able to prepare  $[\text{Fe}_4\text{S}_4(\text{SCH}_2\text{C}_6\text{H}_5)_4]^{2-}$ , and made  $^{57}\text{Fe}$  X-band ENDOR measurements of  $\gamma$ -irradiated species that allowed the determination of the full  $^{57}\text{Fe}$  hyperfine coupling tensors of all four Fe sites in a  $[\text{Fe}_4\text{S}_4]^{3+}$  cluster [88]. Subsequently, thanks to the advantages provided by Q-band ENDOR, namely shifting the  $^1\text{H}$  ENDOR resonances far from those of  $^{57}\text{Fe}$  as well as providing greater  $g$  value dispersion, Moriaud et al. [105] were able to study successfully a 4Fe-red model,  $[\text{Fe}_4\text{S}_4(\text{SCH}_2\text{C}_6\text{H}_5)_4]^{3-}$ , and determined the full  $^{57}\text{Fe}$  hyperfine tensors in this cluster as well [88]. These landmark experimental results on model compounds have been crucial in subsequent theoretical studies of FeS cluster electronic structure [91], and have been extremely helpful in providing benchmarks for understanding biological FeS clusters for which such high precision single-crystal ENDOR studies are not feasible.

### 3.1.4. Heterodisulfide reductase

During the final methane forming step by methanogenic archaea, a mixed disulfide of coenzyme M (CoM, mercaptoethane sulfonate) and coenzyme B (CoB, 7-mercaptoheptanoyl-L-threonine phosphate), CoM-S-S-CoB, is formed [99]. Methanogens from *Methanothermobacter marburgensis* do not contain cytochromes and must reduce CoM-S-S-CoB by other means, as the regeneration of the individual CoM-SH and CoB-SH thiols is needed for continued methane formation [100]. The exothermic reduction of this disulfide is performed by heterodisulfide reductase (Hdr), a part of the proposed hydrogenase-heterodisulfide reductase complex, MvhADG-HdrABC [99]. Hdr is composed of three subunits, HdrA containing a FAD bonding motif as found from primary sequence data and four [4Fe4S] cluster binding sites, based again on the primary sequence. HdrC contains two additional [4Fe4S] binding sites. The subunit of disulfide reduction, HdrB, contains a bound [4Fe4S] cluster in a C-terminal CCG motif (CX<sub>31–39</sub>CCGX<sub>35–36</sub>CXXC) and a bound zinc to the N-terminal CCG domain [101].

HdrABC in the presence of only CoM (CoM-HdrABC) exhibits an EPR signal below 50 K from a paramagnetic  $S = 1/2$  species which has  $g$  values similar to those of the oxidized form of HdrB. This  $S = 1/2$  signal of CoM-HdrABC is lost upon the addition and reaction of CoB-SH, which reduces the [4Fe4S] cluster. The reduction of the FeS cluster observed by EPR, hyperfine broadenings of the EPR signal from  $^{57}\text{Fe}$  enriched enzyme [102] and  $^{33}\text{S}$ -labeled CoM-SH [103], combined with variable-temperature magnetic circular dichroism (VT-MCD) experiments [104], led to the suggested  $[\text{4Fe4S}]^{3+}$  formal charge of the CoM substrate bound cluster in the CoM-HdrABC complex.

Previous 9 and 95 (W-band) GHz ENDOR of CoM-Hdr exhibited unusually isotropic  $^{57}\text{Fe}$  couplings of four distinct iron responses for an [4Fe4S] cluster, with respective signs implied from polarized patterns of the W-band ENDOR responses [105]. The cluster is observed only under oxidizing conditions, with two iron hyperfine couplings resembling an  $(\text{Fe}^{2.5+}-\text{Fe}^{2.5+})$  pair [18], indicating the cluster is  $[\text{4Fe4S}]^{3+}$ , however, this is not supported by the observed average of Hdr-CoM  $g$  values,  $g_{\text{iso}} < 2.0$ , which contrasts to what is observed for well-known  $[\text{4Fe4S}]^{3+}$  clusters, such as oxidized HiPIPs, which have  $g$  values  $> 2.0$  [92] (see Fig. 4).

The 34 GHz  $^{57}\text{Fe}$  ENDOR spectra of CoM-HdrABC and HdrB in an oxidized form (HdrB<sub>oxid</sub>) (Fig. 6), unambiguously resolve all four iron sites

of the [4Fe4S] cluster [106] and provide improved resolution over the earlier W-band results [105]. Using the hyperfine sign results previously found for CoM-HdrABC from 95 GHz ENDOR spectroscopy [105], a mixed valence pair,  $\text{Fe}^{2.5+}-\text{Fe}^{2.5+}$ , with isotropic coupling of approximately  $-30$  MHz is observed, along with a ferric pair,  $\text{Fe}^{\text{III}}-\text{Fe}^{\text{III}}$ , with coupling of approximately  $+20$  MHz, which together are typical for an  $[\text{4Fe4S}]^{3+} S = 1/2$  cluster and have been observed previously for other HiPIP proteins [18] and are almost identical to that of the oxidized HiPIP  $[\text{4Fe4S}]^{3+}$  cluster in *Chromatium vinosum* measured by Mössbauer spectroscopy [107].

These  $^{57}\text{Fe}$  hyperfine couplings are in the ‘strong coupling’ regime where the ENDOR response at each microwave frequency is centered at  $A/2$ . The increased separation of the ENDOR  $\nu_{+/-}$  doublets at Q-band frequency and correspondingly higher magnetic fields yielded higher resolution of the four iron hyperfine couplings compared to the situation at X-band measurements, Fig. 6.

### 3.1.5. Hydrogenase

The hydrogenase enzymes consist of three classes, separated by their metal cofactor active sites: the mononuclear iron [Fe]-, diiron [FeFe]-, and the [NiFe]-hydrogenases [108]. The active site of the [FeFe] enzymes is shown in Fig. 7. Both [FeFe] and [NiFe]-hydrogenases contain multiple FeS clusters for electron delivery to their active sites, however the [FeFe]-hydrogenase uniquely contains an [4Fe4S] cluster that is completely cysteinyl coordinated and is bound to the proximal iron ( $\text{Fe}_p$ ) of the active site diiron center (H-cluster) through a cysteine thiolate bridge conserved throughout the [FeFe] hydrogenases [109,110]. The proximal (to the [4Fe4S] cluster) iron,  $\text{Fe}_p$ , and the distal iron,  $\text{Fe}_d$ , each contain CO and  $\text{CN}^-$  exogenous ligands, and are bridged by a CO and two thiolate bridges from a dithiolate moiety, unique to [FeFe]-hydrogenases [108].

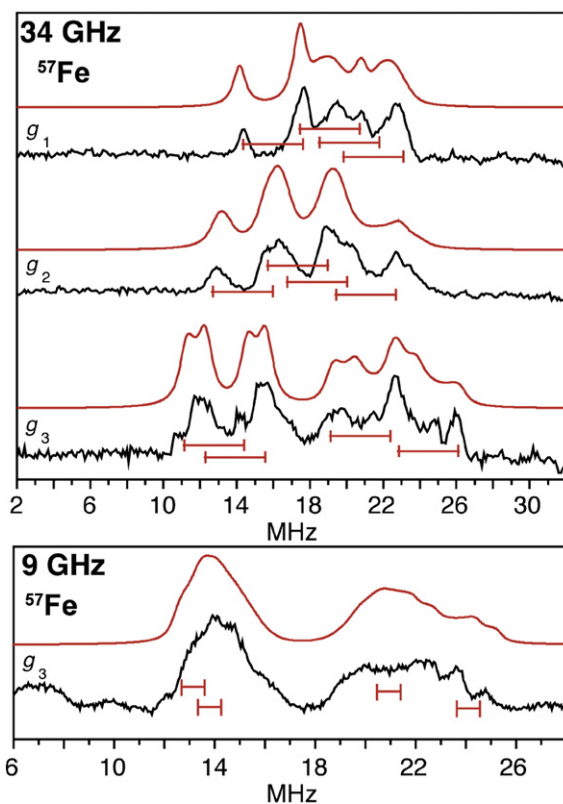


Fig. 6. The  $^{57}\text{Fe}$  ENDOR of the [4Fe4S] cluster of the HdrB subunit taken at Q- and X-band frequencies with  $A/2$  centered goalposts in red of length equal to  $2\nu_N$ . The higher frequency, Q-band (34 GHz) ENDOR generated better separation of the  $^{57}\text{Fe}$  hyperfine as  $2\nu_N$  is much greater from the higher magnetic field than that employed at X-band (9 GHz) frequency.  $^{57}\text{Fe}$  ENDOR reprinted from Fig. 2 of Fielding et al. [106] with kind permission from Springer Science and Business Media © 2013 SBIC.

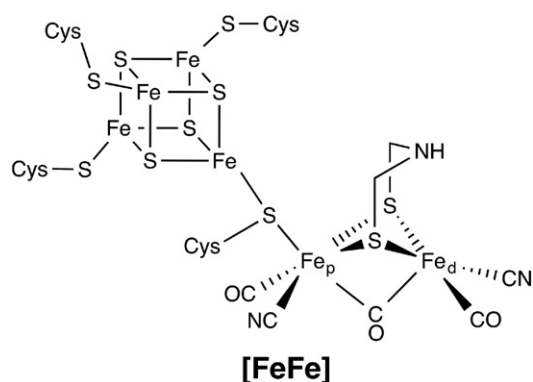


Fig. 7. Hydrogenase active site structure; iron-only [FeFe] hydrogenase.

While the advanced EPR spectroscopic characterization of hydrogenase has provided an abundance of information including ligand unpaired spin density [111], thiolate bridge atom identification [112–115], cluster assembly [113,116–121], and model complexes [122–124], all extensively reviewed elsewhere [108,116,125], we will briefly show the particular example of the  $^{57}\text{Fe}$  ENDOR and HYSCORE work of the [4Fe4S] cluster of the [FeFe]-hydrogenase [41]. This study determined that the  $\text{Fe}_p$  of the paramagnetic  $[\text{Fe}^{1+}-\text{Fe}^{2+}]$  oxidized H-center is in the  $\text{Fe}^I$  oxidation state and binds to the cuboidal [4Fe4S] cluster, while the distal iron,  $\text{Fe}_d$ , alternates between  $\text{Fe}^I$  (reduction) and  $\text{Fe}^{II}$  (oxidation) states. It is the paramagnetic  $\text{Fe}_p^I$  ( $3d^7$ ) ion that is the source of unpaired electron spin density that contributes to all iron hyperfine values observed for the formally diamagnetic  $[\text{4Fe4S}]^{2+}$  center via spin density distribution across the entire 6Fe center [41]. All six iron hyperfine values were determined, the four of the [4Fe4S] cluster through ENDOR spectroscopy, with their overlapping, orientation-dependent pattern deconvoluted through the use of pulsed Davies TRIPLE experiments (See Fig. 8), a ‘pump-probe’ technique [37]. The weaker hyperfine values of the [FeFe] active site were determined through HYSCORE spectroscopy [41]. This *tour de force* combination of advanced EPR techniques has fully characterized the iron electronic structure of the [FeFe]-hydrogenase.

### 3.1.6. Nitrogenase

ENDOR and ESEEM spectroscopies have been applied extensively to the ‘‘Everest of metalloenzymes’’ in an effort to shine light on biological reduction of dinitrogen to ammonia [14,58–60,126]. The complex mixed-metal active site of nitrogen reduction by nitrogenase,  $\text{FeMo-co}$  ( $\text{Fe}_7\text{S}_9\text{CMo}$ ). As noted above, the early development of orientation-selective ENDOR occurred in the context of X-band  $^{57}\text{Fe}$  field-modulated CW ENDOR studies of the resting-state ( $S = 3/2$ )  $\text{FeMo-co}$ . The hyperfine tensors thus derived [127–129] were later used for the Mössbauer analysis [130]. More recently, 35 GHz  $^{57}\text{Fe}$  ENDOR was used to identify the different CO-bound inhibitor states [131,132].

Most recently, 35 GHz Davies pulsed  $^{57}\text{Fe}$  ENDOR was combined with the PESTRE techniques to allow the characterization of all seven of the Fe sites in an  $S = 1/2$  hydrogen turnover state of  $\text{FeMo-co}$  that has accumulated four electrons/protons, stored as two hydrides that bridge Fe and two protons [46].  $^{57}\text{Fe}$  ENDOR studies yield the hyperfine tensors for five Fe sites of this intermediate and the coupling magnitude of a sixth. TRIPLE ENDOR provided valuable assistance in decomposing overlapping  $^{57}\text{Fe}$  responses. Pulsed ENDOR Saturation and Recovery (PESTRE) allowed a direct measurement of the hyperfine signs, Fig. 9. The PESTRE protocol employs three stages of Davies microwave pulse sequences: (I) no applied RF, to establish an electron spin echo baseline; (II) applied RF at the frequency of the probed ENDOR transition, applied to saturate the response; and (III) RF frequency turned off, to monitor

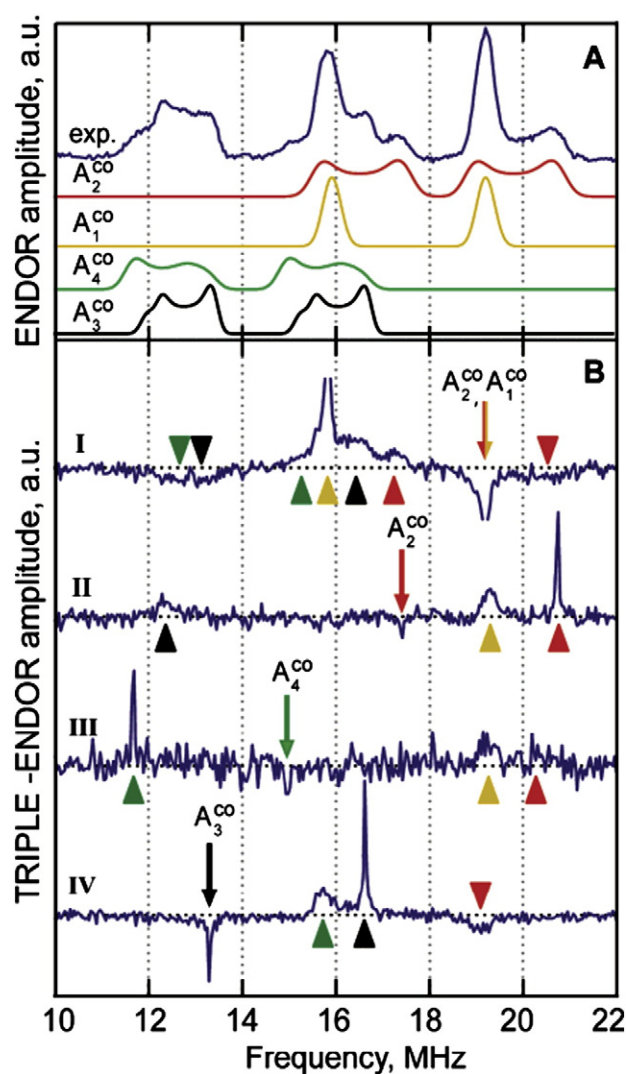
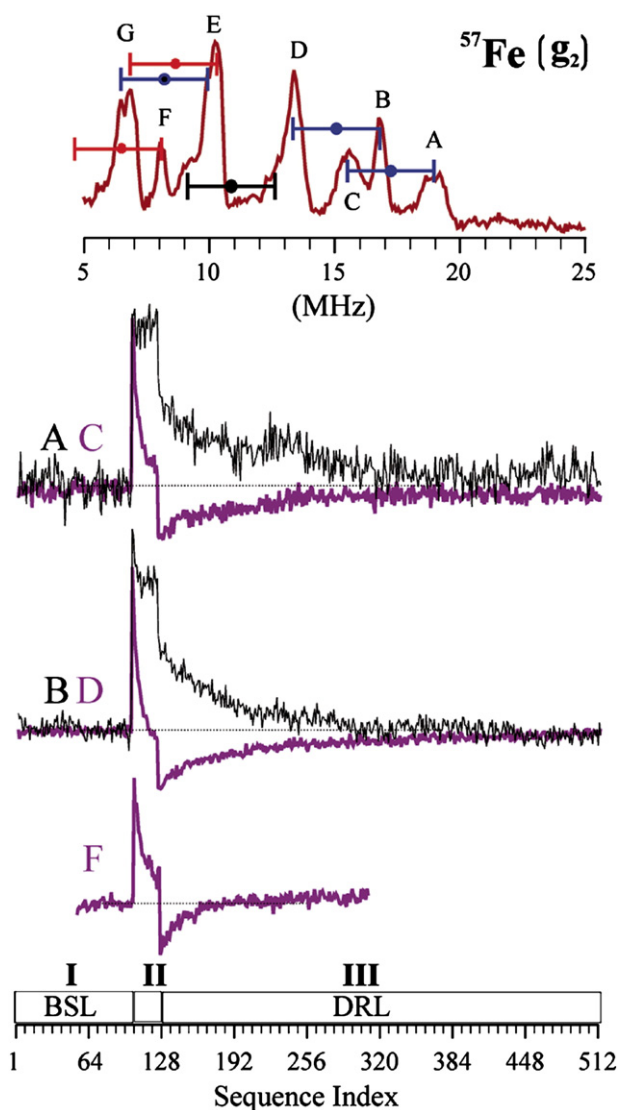


Fig. 8. Q-band TRIPLE spectra of the  $^{57}\text{Fe}$ -enriched H-cluster of the [FeFe] hydrogenase in the  $\text{H}_{\text{ox}}-\text{CO}$  state (where an exogenous CO ligand is bound). (A) Reference  $^{57}\text{Fe}$  ENDOR spectrum with simulated components  $A_2^{\text{CO}}$ ,  $A_1^{\text{CO}}$ ,  $A_4^{\text{CO}}$ , and  $A_3^{\text{CO}}$  of the cuboidal [4Fe4S] cluster. (B) Difference (TRIPLE ENDOR) Q-band spectra for various pump frequencies (second RF pulse) at frequencies indicated by arrows, with color of the arrows corresponds to the HFI components of the ENDOR spectrum (panel A), which were predominantly excited. The triangles in B assign the peaks in the difference TRIPLE spectra to the hyperfine couplings of the ENDOR spectrum using the same color code as in A. Reprinted with permission from Silakov et al. [41] Copyright 2007 American Chemical Society.

the ESE relaxation behavior which is characteristic of the ratio of  $A/g_n$ . A particular benefit of this technique is that it does not require comparison of the intensities of  $\nu_+$  and  $\nu_-$  branches of an ENDOR spectrum, giving reliable sign information from a single branch.

Through the use of a sum-rule on the spin projection coefficients [18], the magnitude and sign of all seven Fe sites are found. The significance of these measurements is to account for the four additional electrons of the  $E_4$  state compared to resting state ( $E_0$ ), using the Lowe–Thorneley scheme for nitrogenase intermediates [133]. The  $^{57}\text{Fe}$  hyperfine character reveals that the formal redox state of the  $E_4$  intermediate is the same as the resting state cluster, although it has four additional electrons. Therefore, these additional electrons must be ‘stored’ on 2 of the 4 protons of the  $E_4$  intermediate as bridging hydrides, yielding critical insight into the nitrogenase mechanism.



**Fig. 9.** Determination of signs of hyperfine couplings at  $g_2$  by PESTRE technique at Q-band. Top: Davies ENDOR spectrum indicating the ENDOR peaks being interrogated. The goalposts here are color coded to indicate sign of hyperfine coupling: blue, negative; red, positive; black, undetermined. Center: PESTRE traces, presented as the difference between the observed ESE signal and the BSL ( $\Delta$ ESE) recorded at: upper set: peaks A (black trace) and C (purple trace); middle set: B (black trace) and D (purple trace); lower: F (purple trace). Bottom: schematic of the PESTRE protocol showing Stage I (RF off, BSL); Stage II (RF on, ENDOR signal); Stage III (RF off, DRL). Reprinted with permission from Doan et al. [46] Copyright 2011 American Chemical Society.

### 3.1.7. Other components: heterometal

**3.1.7.1.  $^{95}\text{Mo}$  ENDOR.** The nitrogenase  $\alpha$ -70<sup>le</sup> MoFe protein described above contains two metal-bridging hydride ligands, as characterized by  $^1\text{H}$  ENDOR [134]. Although hydride binding only to Fe sites seemed more plausible, it was important to test the possibility of hydride binding involving the Mo ion. The Davies ENDOR studies at multiple magnetic fields of the  $^{95}\text{Mo}$ -enriched intermediate showed that the isotropic  $^{95}\text{Mo}$  hyperfine coupling was extremely small,  $a_{\text{iso}} \approx 4$  MHz, decreased from that in the resting state (Fig. 10). This  $a_{\text{iso}}$  value is at least five-fold less than the lower bound required by the  $^1\text{H}$  ENDOR measurements for Mo to be involved in forming a Mo–H–Fe, hydride. These measurements thus led to the conclusion that this catalytically central intermediate contains two Fe–H–Fe moieties [60].

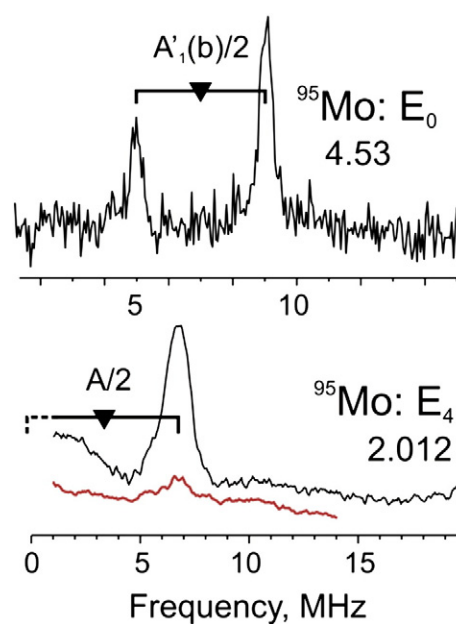


**Fig. 10.** (Top) Davies  $^{95}\text{Mo}$ -ENDOR spectra of  $^{95}\text{Mo}$ -enriched (black) and natural-abundance (red)  $\alpha$ -70<sup>le</sup> MoFe protein: (top) in the resting state ( $E_0$ ); (bottom) CW  $^{95}\text{Mo}$  ENDOR of trapped intermediate ( $E_4$ ) state. Reprinted with permission from Lukoyanov et al. [135] Copyright 2010 American Chemical Society.

**3.1.7.2.  $^{95}\text{Mo}$  NK-ESEEM of a nitrogenase  $S \geq 2$  catalytic intermediate.** Rapid freezing during turnover of a remodeled nitrogenase MoFe protein ( $\alpha$ -70<sup>Val</sup>  $\rightarrow$  Ala,  $\alpha$ -195<sup>His</sup>  $\rightarrow$  Gln) with the electron-transfer Fe protein and with the substrates diazene, methyl diazene ( $\text{HN}=\text{N}-\text{CH}_3$ ), hydrazine,  $\text{NO}_2^-$ , or  $\text{NH}_2\text{OH}$  each results in the loss of the resting-state signal from the catalytic FeMo-co and appearance of the signals from two new signals, Fig. 11 [62]. One signal (denoted **I**) appears in the vicinity of  $g_2$  and has  $S = 1/2$ . A second signal (denoted **H**) is seen as a broad featureless absorption that begins near zero field and extends to  $\sim 5000$  G (at Q-band). Such an EPR signature arises from an FeS cluster in an integer-spin, ‘non-Kramers (NK)’ state with  $S \geq 2$  [62,136]. and could potentially be due to a variety of FeS systems; in nitrogenase, there are three such possibilities: the catalytically active FeMo-co cluster, the electron-transfer P-cluster ( $\text{Fe}_7\text{S}_9$ ) also present in the MoFe protein; and [4Fe4S] cluster in the Fe protein.

NK-ESEEM [65,67] was able to identify the source of the **H** signals. NK-ESEEM time-waves of the **H** signal of  $^{95}\text{Mo}$  enriched MoFe protein produced significant changes of the NK-ESEEM time-wave, which established that this NK-EPR signal arose from the Mo-containing

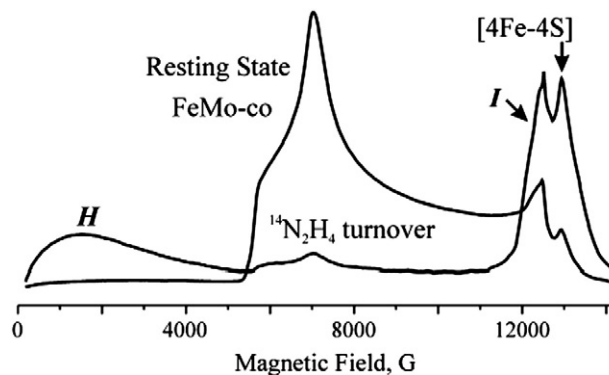


**Fig. 11.** 35 GHz CW EPR spectra (absorption-display) of resting-state FeMo-co and from freeze-trapped turnover intermediates **H** and **I**. Note that resting state FeMo-co has  $S = 3/2$  ground state and effective  $g$  values of [4.3, 3.64, 2.0] and the **H** intermediate has  $S = 2$  ground state and very high effective  $g$  values (low field transitions).

FeMo-co in an integer-spin state, and not the all-iron P or [4Fe4S] clusters [62].

### 3.1.8. Other components: sulfide

The first  $^{33}\text{S}$  ENDOR measurements were performed on the reduced cluster of aconitase, and analysis of  $^{33}\text{S}$  resonances from the [4Fe4S] $^{+}$  cluster of the enzyme–substrate complex suggested that the sulfur sites occur as two pairs ( $S_{\alpha 1}$ ,  $S_{\alpha 2}$ ;  $S_{\beta 1}$ ,  $S_{\beta 2}$ ) with remarkably small spin density on sulfur, and even disclosed their spatial relation to the Fe sites [137]. Fig. 12 summarizes the information from the  $^{57}\text{Fe}$  and  $^{33}\text{S}$  studies about the four Fe and four inorganic sulfides, placing it within the context of the X-ray diffraction structure [138], which showed that cysteines are bound to the three iron ions that correspond to the three  $F_b$  seen spectroscopically. Subsequently,  $^{33}\text{S}$  ENDOR measurements were performed on the resting-state FeMo-co of nitrogenase [128]. We should also note that the substitution for S by isotopically enriched  $^{77}\text{Se}$  ( $I = 1/2$ ) in a [2Fe2S] cluster was instrumental in deducing the stoichiometry of these clusters [139].

## 4. Cluster ligation

### 4.1. Nitrogenous protein-derived ligands (Rieske and Fra2)

The [2Fe2S] cluster is found in many proteins across nature and comprises several classes. These include clusters with complete cysteine coordination as in ferredoxins [7,8,20,140–143], or with some degree of noncysteine coordination. This section focuses on advanced EPR studies of the protein-derived, non-cysteinylligands of the FeS cluster. This situation was first examined for [2Fe2S] clusters with the Rieske and Fra2 proteins. Single histidine ligation (i.e., (Cys $_2$ [Fe $^{II}$ S $_2$ Fe $^{III}$ ]HisCys)) is found in the yeast regulatory protein Fra2-Grx3, which has been characterized by ENDOR [144], and the human protein mitoNEET, and has been well characterized by advanced EPR [78,145–147]. Double histidine ligation (Cys $_2$ [Fe $^{III}$ S $_2$ Fe $^{II}$ ]His $_2$ ) occurs in the well studied Rieske proteins [79,148–152]. These active site structures are all shown in Fig. 13. We discuss here the more recent example of mitoNEET, and the demonstration that even arginine ligation exists, as in the sulfur atom donating [2Fe2S] cluster of Biotin Synthase [153–156].

### 4.2. MitoNEET

The homodimeric [2Fe2S] human mitoNEET protein is located within the mitochondrial membrane [147]. This protein is known to interact with the thiazolidinedione class of diabetes drugs, however its primary function is currently unknown [145]. This [2Fe2S] cluster attained significant bioinorganic interest when it was revealed that it was coordinated by 3Cys 1His amino acids [145], a first among [2Fe2S] proteins,

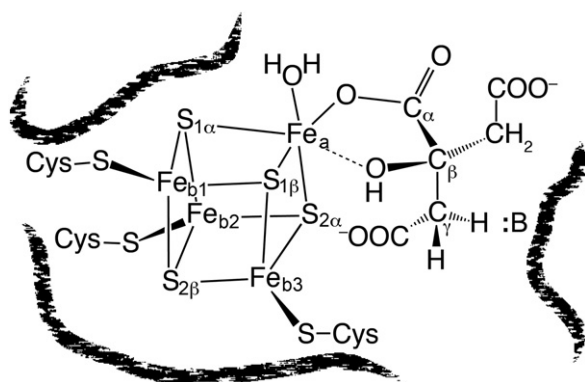


**Fig. 12.** Aconitase structure showing disposition of Fe and S ions as deduced from  $^{57}\text{Fe}$  ENDOR/Mössbauer studies and  $^{33}\text{S}$  ENDOR studies; structure of citrate bound to the unique  $F_a$  site of the [4Fe4S] cluster as deduced from ENDOR spectroscopy of substrates, as described below.

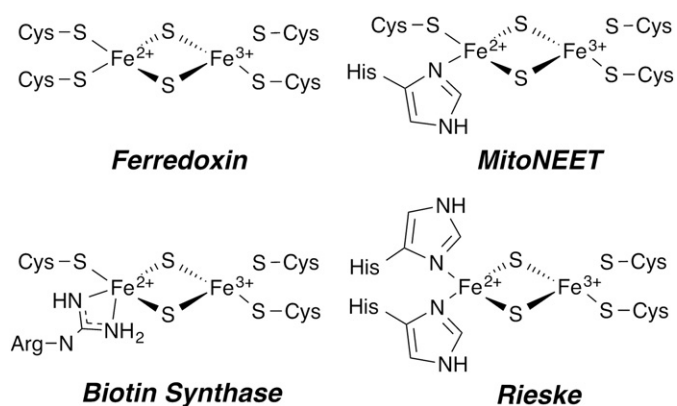


**Fig. 13.** [2Fe2S] $^{+}$  coordination in a variety of biological systems as indicated.

differing from the all Cys ferredoxin class and 2Cys 2His Rieske class (see Fig. 13) [79,149–151,157]. The sole histidine of mitoNEET coordinates to the Fe through the  $N_{\delta}$  of the imidazole ring, the same coordination as observed for each His in Rieske clusters [145].

The multi-frequency EPR and ESEEM work at X- (9.5 GHz),  $K_a$ - (31 GHz), and ‘Q’- (34 GHz) bands elucidated the full structural characteristics the individual clusters and the dipole interaction of the two  $S = 1/2$  [2Fe2S] $^{+}$  clusters of the homodimer [78], which are separated at a distance of 16 Å [145]. As is typically done, the Fe ions are separately described as a ferric, Fe $^{III}$   $S = 5/2$ , and ferrous, Fe $^{II}$   $S = 2$ , ions and an antiferromagnetically coupled representation results in the observed  $S = 1/2$  ground state [20]. The coupled representation for a [2Fe2S] cluster typically represents a single isolated FeS cluster well, however, the close proximity of the two [2Fe2S] clusters ( $\sim 16$  Å) of the homodimer was taken into consideration. The uncoupled representation employed by Dicus et al. [78] employs the usual Fe ion spin projections (Eq. (6)) [158] and sums of all dipolar interactions of every iron of the two [2Fe2S] clusters, both *inter*-cluster and *intra*-cluster dipole interactions, 6 interactions total. This approach was advantageous for the assignment of the [2Fe2S] iron oxidation states as the intra-cluster dipolar distances vary enough to yield predictable differences in Fe–Fe couplings. By mapping the Fe–Fe pairs onto the crystal structure the assignment of the Fe $^{II}$  and Fe $^{III}$  oxidation states could be made to the specific iron sites of the [2Fe2S] clusters. In this model, the Fe $^{III}$  can either be coordinated by the two cysteines or by one cysteine and one histidine. Only an assignment where the Fe $^{III}$ –Fe $^{III}$  intra-cluster pair occupies the inner iron sites, i.e., those with the least separation (Fig. 14), yields a dipolar coupling observable by X-band EPR. Therefore the Fe $^{II}$  ions occupy the outer intra-cluster pair and have the single histidine ligand coordinated, as shown by ‘Fe2’ in Fig. 14 [78].

The small hyperfine interaction of the  $^{14}\text{N}_{\delta}$  histidine was amenable to ESEEM spectroscopy, and multi-frequency microwave instrumentation allowed for the deepest available modulation to be obtained. To obtain the deepest amount of modulation, increased ESEEM signal, one may aim to be within the ‘cancellation regime’ where one electron manifold ( $M_S$ ) is nearly canceled. This is the case when the hyperfine energy is (approximately) equal to twice its Larmor frequency [159]. Recall, as the microwave frequency of instrument is increased, the Larmor frequency of the resonant nuclei scales linearly. For example, the Larmor frequency of  $^{14}\text{N}$  is approximately 1.03 MHz for a  $g = 2$  field position at X-band (9.5 GHz), but will increase to 3.40 and 3.84 MHz for the same EPR transition at  $K_a$  (31 GHz) and Q-band (35 GHz), respectively. One of the largest advantages of moving in microwave frequency from X- up to Q-band is that proton resonances are shifted from the nitrogen region as the proton, with its large  $g_N$  value, Larmor frequency moves from 14 MHz to  $>50$  MHz.

The mid-range frequency ESEEM studies by Dicus et al. [78] assigned the coordinating histidine nitrogen,  $N_{\delta}$ , to the Fe $^{II}$  ion of the reduced [2Fe2S] $^{+}$  cluster of mitoNEET. As  $^{15}\text{N}$  lacks a quadrupole moment, the

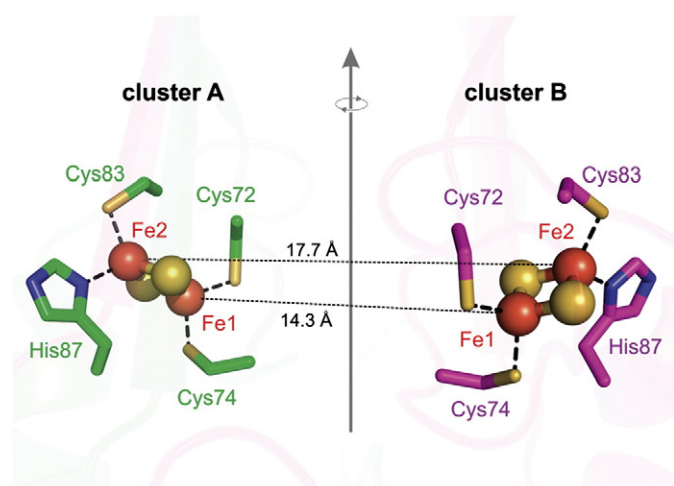


**Fig. 14.** Two [2Fe2S] clusters, (iron, orange, sulfur, yellow) of the homodimer human mitoNEET separated by ~16 Å, related by a rotation around a 2-fold symmetry axis between the two monomers (green and pink). PDB ID 2QH7.

Reprinted with permission from Dicus et al. [78] Copyright 2010 American Chemical Society.

transitions obtained by ESEEM are a result of only the anisotropic portion of the hyperfine tensor, allowing for a more direct estimate of the dipolar contribution, which can be used in refining the  $^{14}\text{N}$  ESEEM analysis. The values of  $(^{15}\text{N})a_{\text{iso}} = 8.77$  MHz and  $T = 1.77$  MHz obtained by both  $K_a$ - and  $Q$ -band ESEEM were consistent with both  $Q$ -band Davies ENDOR and HYSCORE spectroscopies, demonstrating the accuracy of obtaining the  $^{15}\text{N}$  hyperfine tensor through ESEEM at either  $K_a$  or  $Q$  band microwave frequencies.

The  $^{14}\text{N}$  hyperfine parameters are scaled from the  $^{15}\text{N}$  ESEEM analysis by their nuclear gyromagnetic ratio  $|A(^{14}\text{N})/A(^{15}\text{N})| = |g_{\text{N}}(^{14}\text{N})/g_{\text{N}}(^{15}\text{N})| = 0.713$ , which then facilitates extraction of the  $^{14}\text{N}$  quadrupole parameters. The complete  $^{14}\text{N}$  quadrupole tensor,  $\mathbf{P}(^{14}\text{N})$  and its relative orientation with respect to the iron sulfur cluster could then be elucidated by extensive analysis involving field dependent simulations and crystal structure information. From the simulation-determined  $\mathbf{P}$  and  $\mathbf{A}$  orientations with respect to  $\mathbf{g}$ , assuming a typical quadrupole tensor orientation for the imidazole nitrogen [24], the orientation of  $\mathbf{g}$  was mapped on the cluster with its principal component,  $g_1$ , lying in the  $\text{Fe}-(\mu)\text{S}_2\text{-Fe}$  plane, offset  $33^\circ$  from the Fe–Fe vector, Fig. 15. This assignment for mitoNEET is in partial agreement with that of the original Rieske protein studies, where  $g_1$  was also assigned along the Fe–Fe vector [79]. It also only partially agrees with the later study on Rieske protein of bovine mitochondrial cytochrome *bc1* complex by Bowman et al. [149] who had available a protein crystal. Single crystal EPR has the ability to definitively map a  $\mathbf{g}$  tensor onto the molecular frame. The Rieske bishistidine ligated [2Fe2S] core in the single-crystal case was found to have  $g_1$  close to the S–S vector [149]. Ultimately, single crystal EPR would need to be done on mitoNEET along with further examples of Rieske clusters to determine  $\mathbf{g}$  tensor orientations overall in these systems. Such information would greatly assist computational studies of electronic structure of [2Fe2S] centers and how changes in coordination can tune the redox and catalytic properties of these important systems.

#### 4.3. Biotin synthase

The biotin synthase enzyme (BS, or BioB) contains two FeS clusters. One is a [4Fe4S] cluster which binds S-adenosylmethionine (SAM or AdoMet) as observed by crystallography [155] and catalyzes the production of 5'-deoxyadenosyl radical (5'-dA•) as performed by the radical SAM enzyme family, to be discussed later. The [4Fe4S] radical SAM cluster is not air-stable and is lost within minutes upon exposure to

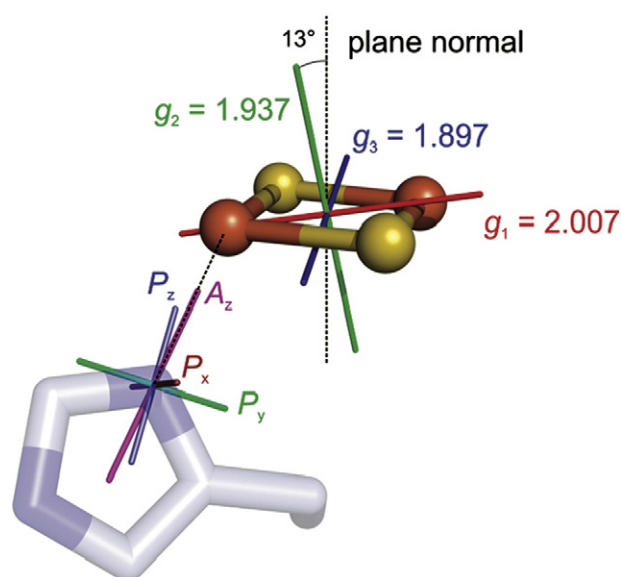


**Fig. 15.** The assignment shown of  $A_z$  aligned with the N–Fe bond and  $P_x$  with the imidazole plane normal yields the  $\mathbf{g}$  tensor orientation for mitoNEET protein ( $\mathbf{g} = [g_1, g_2, g_3] = [2.007, 1.937, 1.897]$ ). The angle between the  $g_2$  axis and the cluster plane normal is  $13^\circ$ , the  $g_1$  axis is  $34^\circ$  offset from the Fe–Fe vector, and  $g_3$  is  $33^\circ$  offset from the S–S vector. Reprinted with permission from Dicus et al. [78] Copyright 2010 American Chemical Society.

air and is thus absent from protein purified aerobically. A second single air-stable  $[2\text{Fe}2\text{S}]^{2+}$  cluster is observed per monomer of the biotin synthase homodimer isolated and purified from *Escherichia coli* [153].

Isotopic  $^{15}\text{N}$  labeling of the Arg amino acids through the incorporation of (*guanidino*- $^{15}\text{N}_2$ )-L-arginine into the growth media confirms the ligation of the paramagnetic  $[2\text{Fe}2\text{S}]^+$  cluster by the amino group of Arg260 (see Fig. 13) and is supported by the previous loss of  $^{14}\text{N}$  hyperfine coupling observed for the Arg260Met variant by previous 3-pulse ESEEM spectroscopy and more recent  $^{14}/^{15}\text{N}$  HYSCORE studies (Fig. 16) [153,156]. This unique Arg ligation to a  $[2\text{Fe}2\text{S}]^+$  cluster, also observed in the crystal structure [155], introduces another  $[2\text{Fe}2\text{S}]^+$  cluster with non-cysteine coordination.

### 5. Spectroscopy of substrates

The [4Fe4S] clusters serve many functions in nature. Initially characterized solely as electron transfer agents, as in ferredoxins and other redox enzymes, their roles quickly expanded upon the discovery of the unique open iron site of the [4Fe4S] cluster of aconitase [160]. Beinert and Kennedy [137,161–163] were the first to characterize an FeS cluster that catalyzed a chemical reaction, not just electron transfer. This section focuses on advanced EPR studies of exogenous compounds: substrates, substrate analogs, or inhibitors, which interact with the FeS cluster active site of such enzymes, and either have naturally occurring magnetic nuclei ( $^1\text{H}$ ,  $^{14}\text{N}$ ,  $^{31}\text{P}$ ) or can be specifically labeled with them ( $^2\text{H}$ ,  $^{13}\text{C}$ ,  $^{15}\text{N}$ ,  $^{17}\text{O}$ ).

#### 5.1. Aconitase

The enzyme aconitase catalyzes the stereospecific interconversion of citrate and isocitrate via the dehydrated intermediate *cis*-aconitate, Fig. 17. The active site contains a  $[4\text{Fe}4\text{S}]^{2+}$  cluster that can be reduced to the EPR-active  $[4\text{Fe}4\text{S}]^+$  state with retention of activity. The cluster does not act in electron transport but rather performs its catalytic function through interaction with substrate at a specific single iron site of the cluster ( $\text{Fe}_a$ ), first identified by Mössbauer [164]. This enzyme was the test bench whose study not only showed how ENDOR spectroscopy could determine active-site composition and electronic and geometric

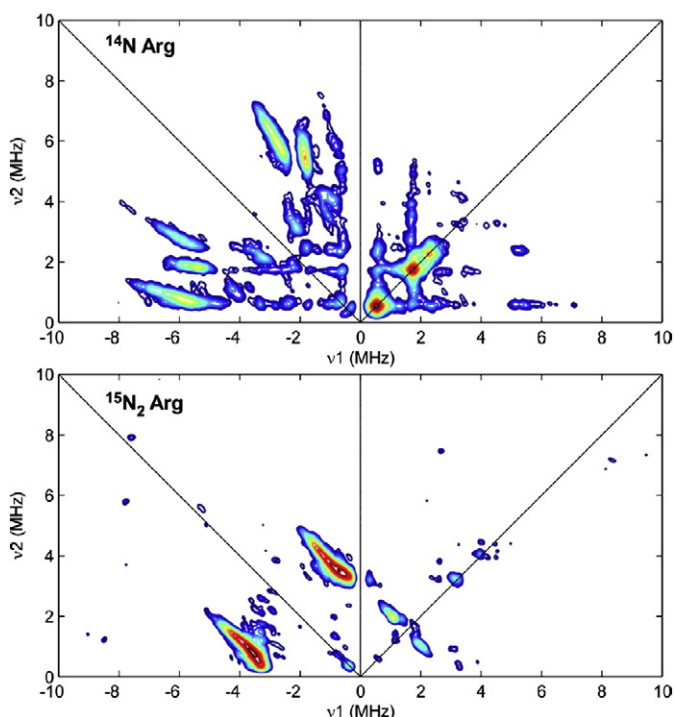


**Fig. 16.** X-band HYSCORE spectra of biotin synthase paramagnetic intermediate grown in *E. coli* with natural abundance arginine (top) and (*guanidino*- $^{15}\text{N}_2$ )-L-arginine (bottom). The  $^{15}\text{N}$  coupling observed in the bottom HYSCORE spectrum corresponds to  $^{15}\text{N}$  labeling of the Arg260 residue.

Reprinted with permission from Fugate et al. [153] Copyright 2012 American Chemical Society.

structure: ENDOR studies of substrate interactions made decisive contributions to the determination of the enzyme catalytic mechanism.

The first question addressed in the ENDOR investigation of the catalytic role of the cluster in a dehydration/hydration reaction was whether solvent  $\text{H}_2\text{O}$  ( $\text{H}_2\text{O}$  or  $\text{OH}^-$ ) and/or the OH of substrate binds to the cluster. The use of  $^{17}\text{O}$ ,  $^1\text{H}$ , and  $^2\text{H}$  ENDOR showed that the fourth ligand of

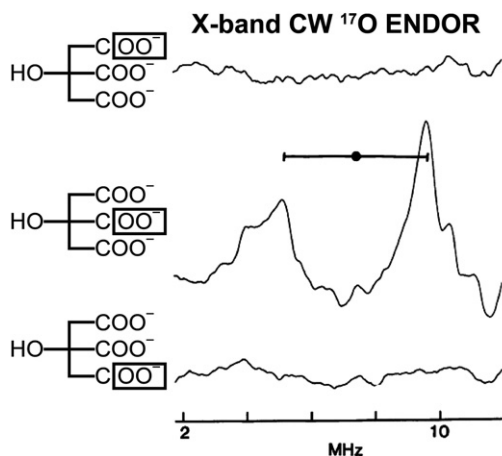
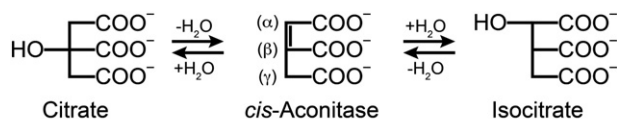


**Fig. 17.** X-band  $^{17}\text{O}$  CW ENDOR of isotopically labeled substrate at the  $\alpha$ ,  $\beta$ , and  $\gamma$  carboxyl positions as indicated in the figure. A  $^{17}\text{O}$  ENDOR response is observed only with labeling of the  $\beta$  carboxyl group.

ENDOR spectra reprinted from Kennedy et al. [162].

$\text{Fe}_a$  in substrate-free enzyme is a hydroxyl ion from solvent, and that binding of substrate or substrate analogs to  $\text{Fe}_a$  causes the hydroxyl to become protonated to form a bound water molecule. Note that this represented the first demonstration of an exogenous ligand bound to an iron-sulfur cluster. The studies further suggested that the cluster might simultaneously coordinate the OH of substrate and  $\text{H}_2\text{O}$  of the solvent (Fig. 17).

The second key question was whether one or more carboxylate groups of substrate bind to the cluster. This was answered through the use of  $^{17}\text{O}$  ENDOR spectroscopy in conjunction with the biochemical brilliance of Beinert and Kennedy. Fig. 17 presents ENDOR spectra of  $[\text{4Fe4S}]^+$  aconitase in the presence of three citrate isotopologues in which the three carboxyl groups have been *individually* labeled with  $^{17}\text{O}$ . ENDOR measurements with substrate whose central ( $\beta$ ) carboxyl group is  $^{17}\text{O}$  labeled show a strong  $^{17}\text{O}$  pattern but no  $^{17}\text{O}$  ENDOR signal was observed when either of the terminal carboxyl groups ( $\alpha$  or  $\gamma$ ) was  $^{17}\text{O}$  labeled (Fig. 17). Thus under the experimental conditions of these samples, the central carboxyl group binds to  $\text{Fe}_a$ , but the two terminal groups ( $\alpha$  or  $\gamma$ ) do not bind to the cluster. The end result of these and other  $^{17}\text{O}$  ENDOR measurements was that the substrate is bound as a chelate involving the citrate hydroxyl and a  $\beta$ -carboxyl oxygen, Fig. 12. This ENDOR-derived structure for the substrate-bound cluster was eventually corroborated by subsequent X-ray diffraction studies [165].

However, the enzyme also is able to accommodate substrate bound by the  $\alpha$ -carboxyl, as was shown by  $^{17}\text{O}$  ENDOR of enzyme that had bound a  $^{17}\text{O}$ -enriched isocitrate analog that lacks the  $\beta$ -carboxylate. Presumably the addition of the negatively charged carboxyl causes protonation of the  $\text{OH}^-$  that binds to the cluster in the absence of substrate. The resulting structure of citrate bound to the unique Fe of the cluster, as deduced from ENDOR spectroscopy, is shown in Fig. 12.

ENDOR spectroscopy thus showed that the cluster functions as follows: (i) it helps to position the substrate through the binding of one carboxyl; (ii) it coordinates and accepts the hydroxyl of substrate during the dehydration of citrate and isocitrate; (iii) it donates a bound hydroxyl during the rehydration of *cis*-aconitase. To accommodate the stereochemistry of the reaction, *cis*-aconitase must furthermore disengage from the active site, rotate  $180^\circ$ , and switch the carboxyl that binds before completing the catalytic cycle.

## 5.2. Nitrogenase

The mechanism of nitrogenase has been probed by ENDOR of numerous isotopically labeled substrates [61,166,167]. A detailed discussion of this aspect of the use of ENDOR is beyond the scope of this review, but has been recently summarized elsewhere [58–60,168].

### 5.2.1. Radical SAM

Following aconitase, other catalytic  $[\text{4Fe4S}]$  clusters have been discovered [171], leading to a renaissance of interest in FeS proteins. The realization that the role of  $[\text{4Fe4S}]$  clusters extends beyond electron transfer has been greatly magnified by the discovery of their role in the radical SAM (*S*-adenosylmethionine) enzymes. Radical SAM enzymes comprise a diverse and rapidly expanding superfamily that has been recently reviewed (many times) [121,172–180] and is the subject of other contributions to this Special Issue.

Enzymes of the radical SAM superfamily utilize a  $[\text{4Fe4S}]$  cluster and *S*-adenosylmethionine (SAM) to generate catalytically essential radicals, Fig. 18. A key mechanistic question posed by this family was the role of the  $[\text{4Fe4S}]$  cluster bound by a characteristic  $\text{CX}_3\text{CX}_2\text{C}$  motif. As with aconitase, the clusters of these enzymes have a “unique” iron site that is not coordinated to the enzyme by a cysteinyl sulfur: does this Fe have a catalytic function, as is true for aconitase? This question was answered through the use of EPR and pulsed 35 GHz ENDOR spectroscopy applied to the radical-SAM enzymes, pyruvate formate-lyase (PFL) activating enzyme (PFL-AE), and lysine 2–3 aminomutase (LAM) [170, 181,182]. The experiments disclosed that the cluster plays at least a

dual role: the unique Fe anchors the AdoMet cofactor by chelating the amino and carboxyl groups of methionine; electron transfer from the cluster initiates homolytic cleavage of the bond to adenosine.

$^2\text{H}$  and  $^{13}\text{C}$  pulsed ENDOR spectroscopy was performed on  $[4\text{Fe}4\text{S}]^+-\text{PFL-AE}$  ( $S = 1/2$ ) with bound AdoMet (denoted  $[1+/\text{AdoMet}]$ ) that had been labeled at the methyl position with either  $^2\text{H}$  or  $^{13}\text{C}$  (see Fig. 19) [181]. The observation of substantial  $^2\text{H}$  and  $^{13}\text{C}$  hyperfine couplings from the labels clearly demonstrated that AdoMet binds adjacent to the 4Fe cluster. The cofactor was shown to bind in the same geometry to both the  $1+$  and  $2+$  states of the cluster through cryoreduction of the frozen  $[4\text{Fe}4\text{S}]^{2+}/\text{AdoMet}$  complex to form the EPR-active reduced ( $1+$ ) state which was trapped in the structure of the oxidized ( $2+$ ) state.

Modeling of the through-space electron–nuclear dipolar interaction between the cluster electron spin and the methyl- $^{13}\text{C}$  and  $^2\text{H}$  showed that the shortest distance between an AdoMet methyl proton and an iron of the cluster is  $\sim 3.7(2)$  Å, with a distance of  $\sim 4.9(6)$  Å from the methyl carbon to this iron. Most intriguingly, the analysis disclosed a through-bond (local), isotropic contribution to the  $^{13}\text{C}$  interaction, which requires overlap between orbitals on the cluster and on AdoMet. Later studies of the same state formed within LAM indicated that the coupling likely arises from interaction of the SAM sulfur with the unique Fe of the cluster.

The coordination sphere of the unique Fe was examined by 35 GHz pulsed ENDOR spectroscopic studies of PFL-AE complexed with SAM labeled with  $^{17}\text{O}/^{13}\text{C}$  in the carboxyl group of the methionine fragment, and with  $^{15}\text{N}$  in the amino group [182]. ENDOR signals observed with all three labels (Fig. 19) showed that both the carboxylato and amino groups of methionine are coordinated to the unique iron of the  $[4\text{Fe}4\text{S}]$  cluster in a classical five-membered-ring N/O chelate. The key structural role of the cluster revealed by ENDOR spectroscopy was subsequently confirmed by X-ray diffraction studies (Fig. 19) [155,177,183,184].

The formation of the amino-acid chelate to the unique Fe anchors the methionine end of SAM, thereby fixing the geometry of the

sulfonium linkage for the subsequent initiation of radical chemistry. In conjunction with the localization of the methylsulfonium moiety near to the unique Fe, as revealed by the  $^{13}\text{C}$  and  $^2\text{H}$  ENDOR measurements, these results led to a proposed reaction mechanism in which inner-sphere electron transfer from the cluster to SAM causes cleavage of the methionine–sulfonium/adenosyl bond that in part is driven by the formation of a coordinate bond between the unique Fe and the thioether sulfur of the methionine product of SAM fragmentation (Fig. 18). The anchoring of SAM and the methionine product to the  $[4\text{Fe}4\text{S}]$  cluster in the structure exhibited in Figs. 18 and 19 is a general bonding motif observed for all radical SAM enzymes.

### 5.2.2. Heterodisulfide reductase

As introduced earlier, Hdr reduces the disulfide bond of CoM–S–S–CoB. Isotopic  $^{13}\text{C}$  labeling of CoM–SH at the second carbon of mercaptoethane sulfonate and subsequent oxidation with CoM formed the singly labeled disulfide product, CoM–S–S– $^{13}\text{C}_2\text{H}_2\text{SO}_3$  [106]. This allowed  $^{13}\text{C}$  Mims ENDOR spectroscopy to yield  $^{13}\text{C}$  hyperfine couplings and confirm the substrate's binding to the  $[4\text{Fe}4\text{S}]$  cluster of HdrB (Fig. 20). The  $^{13}\text{C}$  couplings, [1.8, 1.8, 0.4] MHz, are comparable to those observed for the  $^{13}\text{C}$  hyperfine of methyl- $^{13}\text{C}$ –AdoMet binding to the  $[4\text{Fe}4\text{S}]$  cluster of PFL-AE (vide supra) [181]. These small couplings are expected as the  $^{13}\text{C}$  label is one bond away from the S that is directly interacting with the FeS cluster [106]. In contrast, an Fe ion directly bound to  $^{13}\text{C}$  would give much larger couplings,  $A_{\text{min}} = 12$  MHz [185].

### 5.2.3. The 'second cluster' of radical SAM enzymes

Numerous radical SAM enzymes have a 'second cluster' in addition to the 4Fe4S cluster that binds SAM and reductively cleaves it. The role of the second cluster has also been investigated with advanced paramagnetic resonance techniques, beginning with the ENDOR study of MoA.

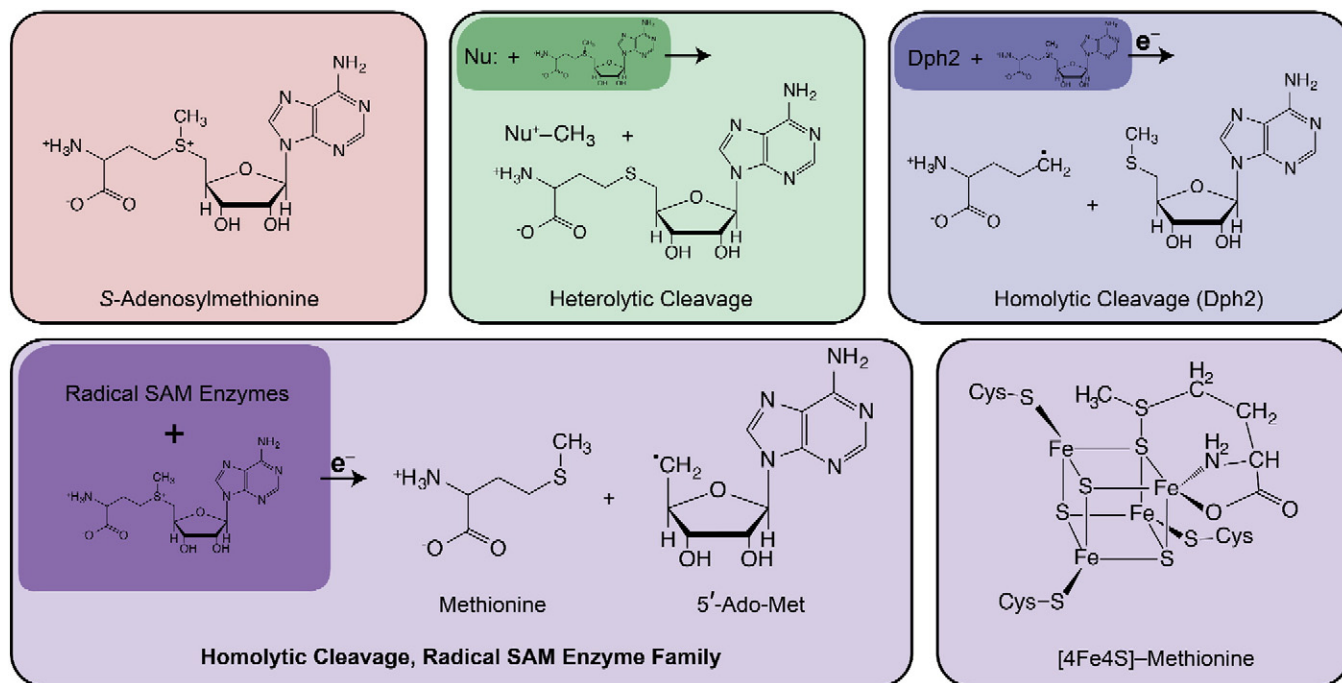


**Fig. 18.** The various reaction products of the S-Adenosylmethionine (SAM) (red) co-substrate. Different reactions, either heterolytic or homolytic cleavage, at the positively charged sulfur atom provide the final products. Heterolytic cleavage by a nucleophilic base (Nu:) results in cleavage of the methyl group by breaking the methyl–sulfur bond, leaving both electrons on the sulfur. Homolytic cleavage of SAM has most commonly been observed in the radical SAM enzyme family, where SAM accepts an electron yielding a methionine and 5'-deoxyadenosyl radical (5'-Ado-Met). Homolytic cleavage (such as in Dph2) may occur uniquely at the opposite 3-amino-3-carboxypropyl group after accepting an electron and results in a different organic radical.

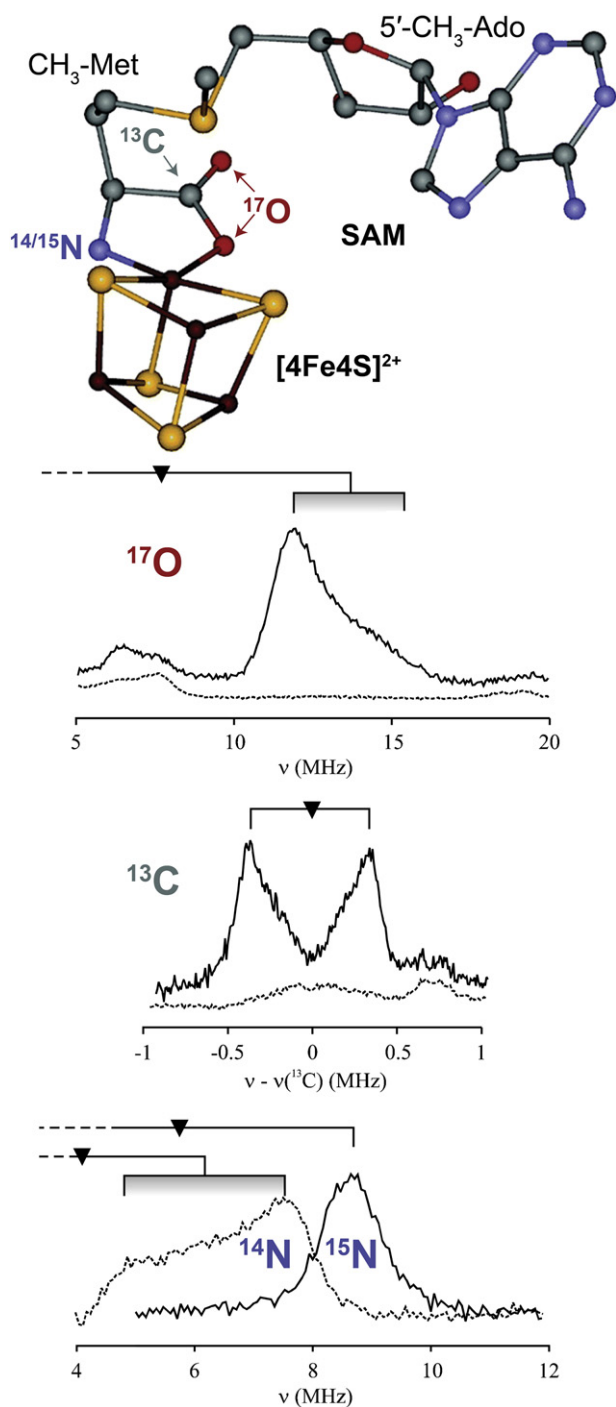


**Fig. 19.** Arrangement of  $[4\text{Fe}_4\text{S}]^{2+}$  and SAM (top) with isotopic labels for corresponding ENDOR spectra below. Q-band Pulsed ENDOR of PF-AE with  $\text{H}_2^{17}\text{O}$ ,  $^{13}\text{C}$  carboxylato-labeled and  $^{15}\text{N}$ -amino-labeled AdoMet compared with data from an unlabeled sample with triangle representing each nuclei's Larmor frequency.

Adapted with permission from Walsby et al. [169] and Lees et al. [170] Copyright 2005, 2006 American Chemical Society.

#### 5.2.4. MoaA

The enzymes MoaA and MoaC catalyze the first step in the biosynthesis of the molybdenum cofactor (Moco) found in the biologically important molybdopterin enzymes, such as xanthine oxidase [186]. Each of these Moa enzymes contain two  $[4\text{Fe}_4\text{S}]^{2+}$  clusters. One  $[4\text{Fe}_4\text{S}]^{2+}$  site, cluster I, is found in an N-terminus  $\text{CX}_3\text{CX}_2\text{C}$  motif and is a characteristic Radical SAM cluster that generates the  $5'\text{-dA}^\bullet$  radical to further catalyze the conversion of guanosine  $5'$ -triphosphate ( $5'$ -GTP) substrate to tetrahydropyranopterin [183,187]. The role of

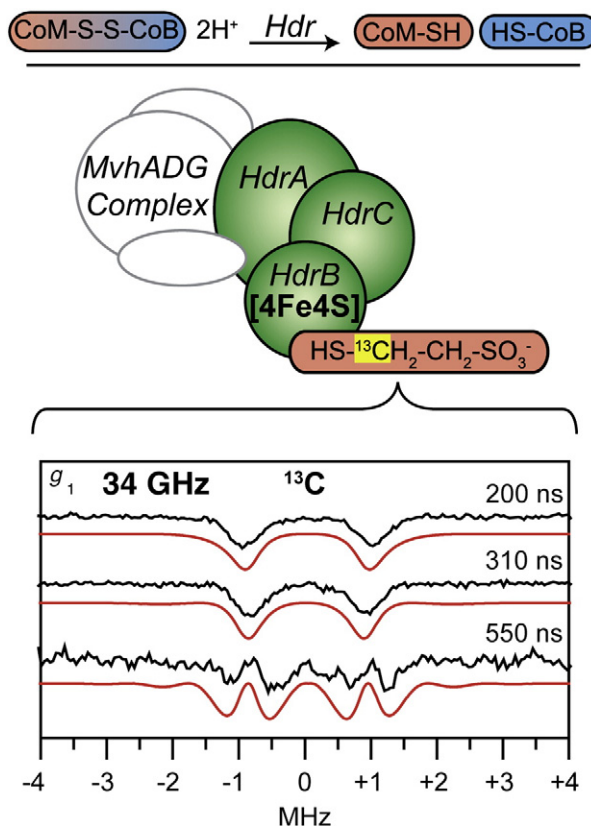


**Fig. 20.** (Top) A cartoon reaction of the reduction of  $\text{CoM-S-S-CoB}$  by Hdr and the cartoon MvhADG-HdrABC protein complex with  $^{13}\text{C}$  ENDOR of  $\text{CoM-HdrABC}$  with  $^{13}\text{C}$  labeled  $\text{CoM}$  ( $\text{HS-}^{13}\text{CH}_2\text{-CH}_2\text{-SO}_3^-$ ). (Bottom)  $^{13}\text{C}$  ENDOR adapted and reprinted from Fig. 4 of Fielding et al. [106] with kind permission from Springer Science and Business Media © 2013 SBIC.

the other cluster, cluster II, was less certain, although X-ray crystallography clearly indicated that it was involved in substrate  $5'$ -GTP binding and/or activation. A crystal structure of MoaA with  $5'$ -GTP suggested that an atom of the purine ring might be coordinating to a unique iron of the second  $[4\text{Fe}_4\text{S}]$  cluster [187], however, ambiguity remained as to whether it was the exocyclic amino group or nitrogen of the purine ring that is coordinating. The ambiguity of interaction of the  $5'$ -GTP substrate with cluster II was a perfect candidate for unraveling by ENDOR spectroscopy.

The radical SAM  $[4\text{Fe}_4\text{S}] S = 1/2$  cluster of MoaA was disrupted through mutagenesis of its  $\text{CX}_3\text{CX}_2\text{C}$  binding motif cysteines. The CW EPR and ENDOR signals of this mutant then arise only from cluster II, the site of  $5'$ -GTP binding. The ENDOR exhibits  $^{14}\text{N}$  hyperfine coupling [188] similar to that found for the amino-nitrogen of the SAM bound to iron in PFL-AE [182]. Nitrogen coordination is easily confirmed through global  $^{15}\text{N}$  labeling of the  $5'$ -GTP substrate and the observed  $^{15}\text{N}$  ENDOR response at the expected shift in frequency as determined from the ratio of the nuclear  $g_N$  values:  $\gamma = |A(^{15}\text{N})/A(^{14}\text{N})| = |g_N(^{15}\text{N})/g_N(^{14}\text{N})| = 1.41$  [11,188]. However, given that the  $5'$ -GTP substrate was globally labeled in  $^{15}\text{N}$ , the issue of whether it is the purine ring or amino nitrogens of  $5'$ -GTP that bind to cluster II is not resolved [187]. Employing an active substrate analog, inosine  $5'$ -triphosphate ( $5'$ -ITP), which lacks the exocyclic amino group at C2 (termed N2) of  $5'$ -GTP, yielded a very similar EPR signal as with the natural substrate and remarkably similar  $^{14}\text{N}$  ENDOR couplings were observed (see Fig. 21). This result confirms that either N1 or N3 of purine rings of both  $5'$ -GTP substrate and  $5'$ -ITP are the sources of nitrogen coordination to the fourth iron of the  $[4\text{Fe}_4\text{S}]$  cluster, not the exocyclic amino group (in  $5'$ -GTP) [188].



Both 5'-GTP substrate and 5'-ITP have multiple purine nitrogen atoms, N1 and N3, and correspondingly multiple nitrogen ENDOR signals of various couplings [188]. With these differing couplings, point-dipole distance estimations could be made for each nitrogen coupling and in conjunction with the predicted bound structure from X-ray crystallography [187], allowed for the assignment of these couplings. The strongest coupled nitrogen belongs to N1 of the purine ring, not the exocyclic amino group, as shown through the use of the substrate analog. However, signals from two additional nitrogens were anticipated, one from the purine ring and the other from the exocyclic amino group, at further distances and thus with weaker couplings. Pulsed Mims ENDOR for the weaker coupled N2 and N3 of the purine yielded maximum couplings of ( $^{15}\text{N}$ )A = 0.5 and 0.2 MHz. The maximum and minimum dipolar components of each nitrogen measurement yield point-dipole model estimates of the distance between the nuclear ( $^{15}\text{N}$ ) spin and the unpaired electron spin of the  $[\text{4Fe4S}]^+$  cluster.

By maintaining the crystallographically well resolved phosphate moiety of 5'-GTP in its fixed position, the ribose sugar and purine ring groups could then be positioned with respect to the  $[\text{4Fe4S}]^+$  cluster to match the cluster-nitrogen distance estimates determined by ENDOR spectroscopy. Fig. 22 superimposes the 5'-GTP model made through the ENDOR distance measurements upon that from the previous X-ray crystal structure. One can readily see some differences and indeed improvements upon the crystal structure. As ENDOR spectroscopy is performed on solution 'powder' samples, the resulting structure may differ from that determined by X-ray crystallography of solid state crystals. In addition to providing another view of active site structure, ENDOR and other advanced EPR techniques have the potential of "seeing" these structures in intermediates that may not be easily crystallized.

### 5.2.5. Biotin synthase (BS)

BS catalyzes biotin synthesis by formation of a thioether linkage between the methylene (C6) and methyl (C9) positions of dethiobiotin (DTB). This sulfur addition is a two step process whereby a 5'-deoxyadenosyl radical ( $5'\text{-dA}^\bullet$ ) is generated by a radical SAM cluster which next abstracts a hydrogen atom from the methyl group (C9) of DTB (Fig. 23). The subsequent high-energy 9-dethiobiotinyl radical is

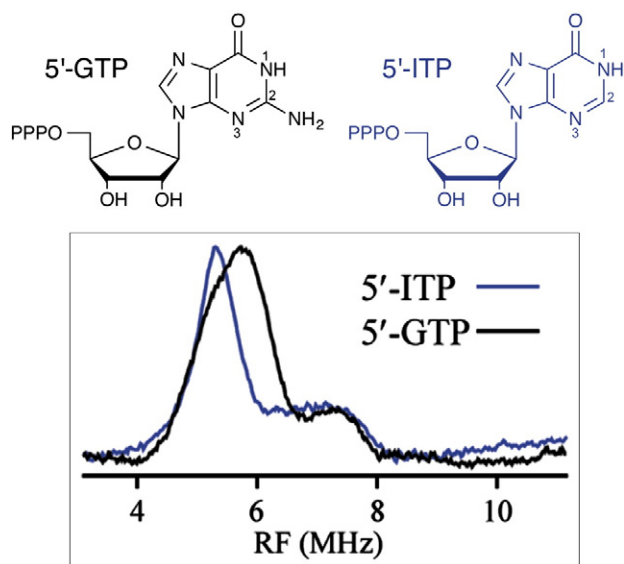


Fig. 21. Chemical schematics of 5'-GTP and 5'-ITP substrates in black and blue, respectively, with corresponding 35 GHz  $^{14}\text{N}$  CW-ENDOR of the bound 5'-GTP and 5'-ITP substrates to MoaA  $[\text{4Fe4S}]^+$  cluster in black and blue, respectively. The possible amino group coordination at C2 (N2) to the FeS cluster is eliminated as the  $^{14}\text{N}$  ENDOR of 5'-ITP do not differ upon the amino group's removal.

Reprinted with permission from Lees N. et al. [188] Copyright 2009 American Chemical Society.

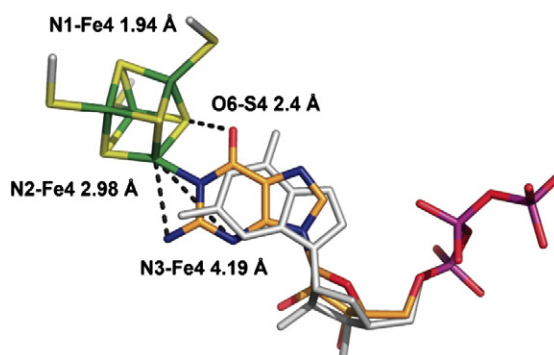


Fig. 22. Proposed model for 5'-GTP binding (C, orange; N, blue; O, red; P, purple) to the Fe4 ion of cluster II (S, yellow; Fe, green). The 5'-GTP model derived by X-ray crystallography (PDB entry 2FB3) is shown in white. Reprinted with permission from Lees N. et al. [188] Copyright 2009 American Chemical Society.

quenched by the addition of a sulfur atom to form the stable enzyme intermediate 9-mercaptodethiobiotin (MDTB). The introduction of a second equivalent of AdoMet and the resulting generation of another  $5'\text{-dA}^\bullet$  radical which abstracts a hydrogen from the methylene group (C6) to allow for the formation of the thioether group and ring closure.

While the  $[\text{4Fe4S}]$  cluster of biotin synthase is the site of AdoMet binding and  $5'\text{-dA}^\bullet$  radical formation [189], the candidacy of AdoMet as the sulfur donor to biotin was excluded by isotopic labeling:  $^{35}\text{S}$  of  $^{35}\text{S}$ -AdoMet is not incorporated into biotin [190]. After the classification of biotin synthase as a radical SAM enzyme, the origin of the sulfur atom that is inserted into biotin needed to be answered. The  $[\text{2Fe2S}]$  cluster, discovered initially by X-ray crystallography [155], was also proposed as the sulfur atom source and shown to be the sulfur atom donor to MDTB by reconstitution of apoenzyme with  $\text{Fe}^{3+}$  and  $^{34}\text{S}^{2-}$  and by the substitution of  $\text{S}^{2-}$  by  $\text{Se}^{2-}$ , each incorporated as the sulfur (or selenium) atom for the ring closure of biotin [191,192].

As the formation of biotin is not a single step process, samples frozen during turnover are a mixture of EPR paramagnetic species poised at various states [156]. The initially proposed binding of the 9-dethiobiotinyl radical to the  $[\text{2Fe2S}]^{2+}$  cluster yields a paramagnetic species, the reduced  $[\text{2Fe2S}]^+$  cluster [156]. The formation of this reduced cluster creates a new paramagnetic probe for coordination studies of the MDTB intermediate formation. EPR studies previously showed that the reduction of the  $[\text{2Fe2S}]^{2+}$  cluster was kinetically linked with the production of MDTB, however they were unable to conclusively determine if the reduction of  $[\text{2Fe2S}]^{2+}$  cluster and MDTB formation occur at the same time [156].

Recent HYSCORE studies of biotin synthase under turnover reveals that the dethiobiotinyl radical, a result of hydrogen abstraction by  $5'\text{-dA}^\bullet$ , moves  $\sim 2.9$  Å closer to the  $\mu$ -sulfide of the  $[\text{2Fe2S}]^{2+}$  cluster for attack and sulfur abstraction [153]. The (9-methyl- $^{13}\text{C}$ )-DTB labeled substrate, obtained by biosynthesis, yielded  $^{13}\text{C}$  coupling ( $a_{\text{iso}} = 2.9$  MHz) observed by HYSCORE spectroscopy (see Fig. 24). This result is consistent

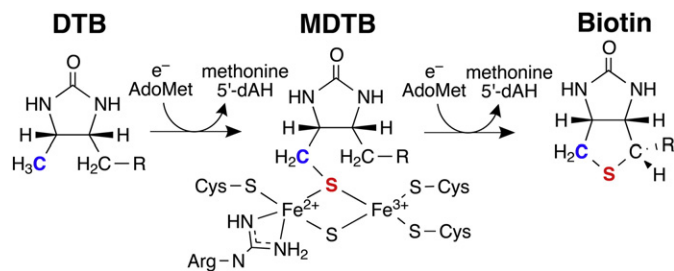


Fig. 23. Formation of biotin from dethiobiotin (DTB) via a two-step reaction with a stable 9-mercaptodethiobiotin MDTB intermediate bound to the sulfur donating  $[\text{2Fe2S}]^+$  cluster.

with the newly formed MDTB intermediate remaining bound to the remnant FeS cluster through the sulfur atom (MDTB–Fe–( $\mu$ )S–Fe) [153], as depicted in Fig. 23. The  $^{13}\text{C}$  coupling is reminiscent of that observed for the Fe–S– $^{13}\text{C}$  of the radical SAM PFL-AE enzyme [182]. This work has characterized the transient MDTB structure, and the binding of substrate to the subsequently remnant Fe–S–Fe cluster [153]. There is great potential for advanced EPR, such as in further characterization of the ring closure mechanism. The kinetics of biotin synthase are favorably slow, so rapid-freeze quench techniques can be dispensed with. Additionally, as the [2Fe2S] cluster is the sulfur donor to biotin, the [2Fe2S] cluster must be regenerated, but we are unaware of any results on the regeneration mechanism. Radical SAM enzymes often play a critical role in the maturation of FeS clusters, maybe the radical SAM character of this enzyme plays two roles?

### 5.2.6. MiaB

Recently, several radical SAM enzymes have been identified that catalyze the attachment of methylthio groups to transfer RNAs or ribosomal proteins. These enzymes are thus called methylthiotransferases (MTTases) and include MiaB, MtaB, and RimO [193–198]. Very recently, MiaB and RimO from *Thermotoga maritima* (TmMiaB, TmRimO) have been investigated by advanced EPR techniques [199]. MiaB contains a radical SAM cluster, but, as described above in MoaA, there is an additional cluster (cluster II), which is proposed as the site of sulfur (here as  $\text{CH}_3\text{S}^-$ ) transfer. These workers used both WT and an inactive MiaB mutant in which the three Cys residues binding the radical SAM cluster were mutated to alanine, so that only cluster II remained, but cluster II retained the ability to bind exogenous ligands. In this case,  $\text{CH}_3^{77}\text{SeNa}$  was used ( $^{77}\text{Se}$ ,  $I = 1/2$ , 7.6% natural abundance), which is an active substrate for these MTTases. HYSCORE of both WT and mutant showed signals due to  $^{77}\text{Se}$  interacting with cluster II ( $A = 3.8(5)$  MHz) indicating direct binding and thus supporting the accepted mechanism for MTTases [199].

### 5.2.7. $^{14,15}\text{N}$ NK-ESEEM of a nitrogenase intermediate common to multiple substrates

We state above that rapid freezing of a remodeled nitrogenase MoFe protein during turnover with each of the substrates, diazene, methyldiazene ( $\text{HN}=\text{N}-\text{CH}_3$ ), hydrazine,  $\text{NO}_2^-$  and  $\text{NH}_2\text{OH}$  results in trapping of a common NK state, **H**, with  $S \geq 2$ . The conclusion that all these substrates react to generate **H** was arrived at from NK-ESEEM studies, which showed that the NK intermediates formed with each substrate give the same time and frequency-domain spectra (Fig. 25) [62,136]. The NK-ESEEM studies of the intermediates formed with methyldiazene  $^{14,15}\text{N}$  isotopologues plus  $^1\text{H}$  isotopologues further demonstrated that **H** corresponds to the nitrogen fixation intermediate with FeMo-co-bound  $[\text{NH}_2]^-$  that is formed upon N–N bond cleavage [62].

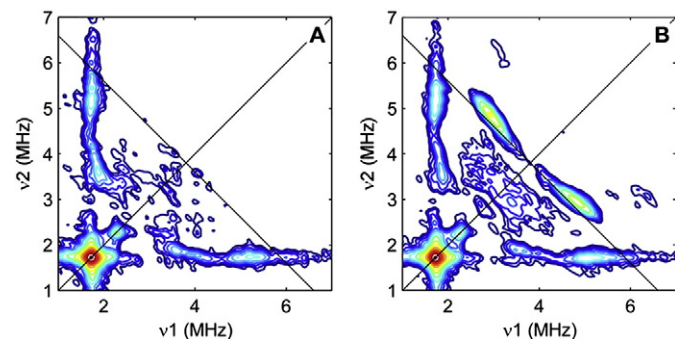


**Fig. 24.** X-band HYSCORE spectra of the biotin synthase paramagnetic intermediate prepared with (A) natural abundance DTB and (B) (9-methyl- $^{13}\text{C}$ )-DTB. The two unique peaks perpendicular to the  $\nu_1 = \nu_2$  diagonal of B are the  $^{13}\text{C}$  response. Reprinted with permission from Fugate et al. [153] Copyright 2012 American Chemical Society.

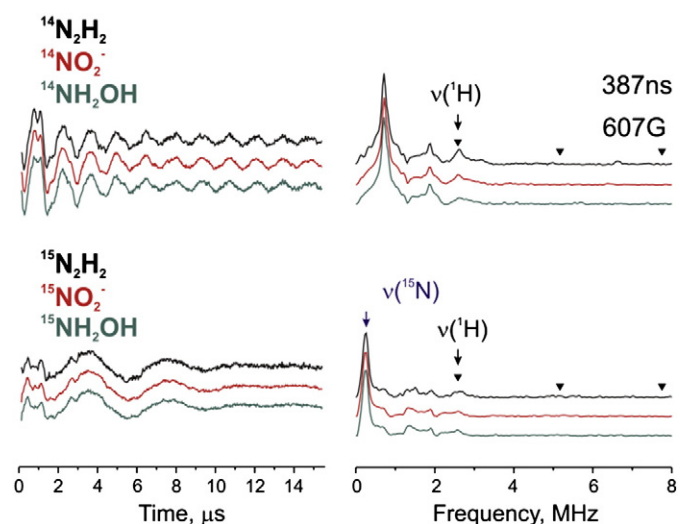


**Fig. 25.** Q-band NK-ESEEM spectra in time (left) and frequency (right) domains obtained for integer spin intermediates of  $\alpha$ - $^{70}\text{Ala}$ / $\alpha$ - $^{195}\text{Gln}$  MoFe protein turnover samples prepared with diazene (black), nitrite (red) and hydroxylamine (green). Upper spectra were measured for  $^{14}\text{N}$  substrate samples, lower – for samples with  $^{15}\text{N}$  labeled substrates. Triangles in the frequency domain spectra represent suppressed frequencies  $n/\tau$ ,  $n = 1, 2$ .

### 5.2.8. Bio-organometallic enzyme intermediates

Perhaps the most remarkable cluster–substrate complexes contain bio-organometallic moieties, involving Fe–C bonds (and not involving  $\text{CN}^-$  as seen in hydrogenase!). The first such was a state in which the nitrogenase active site binds the alkene product of alkyne reduction. Considerably later, this study was used as the foundation for efforts to assign analogous states of other catalytic [4Fe4S] clusters.

### 5.2.9. Nitrogenase

Biological ‘nitrogen fixation’, the reductive cleavage of the  $\text{N}_2$  triple bond at ambient pressure and temperature to form two  $\text{NH}_3$ , is carried out by the nitrogenase enzyme system. The catalytic site is a multimetallic cluster, denoted FeMo-cofactor (FeMo-co), [ $\text{Fe}_7\text{MoS}_9\text{C}$ ]. In recent years a number of states have been freeze-trapped with reduction intermediates of  $\text{N}_2$  and alternative substrates bound to FeMo-co, and characterized by ENDOR/ESEEM/HYSCORE. The first of these were states trapped during the reduction of alkynes: acetylene, propargyl alcohol ( $\text{HC}\equiv\text{C}-\text{CH}_2\text{OH}$ ), and propargyl amine ( $\text{HC}\equiv\text{C}-\text{CH}_2\text{NH}_2$ ).

The as-isolated form of the nitrogenase WT MoFe protein exhibits a characteristic  $S = 3/2$  electron paramagnetic resonance (EPR) spectrum from resting state FeMo-co. The  $\alpha$ -Ala $^{70}$ -remodeled MoFe protein behaves similarly, but this mutation allows the use of larger substrates than just  $\text{N}_2$  or acetylene. When the  $\alpha$ -Ala $^{70}$ -MoFe protein is freeze-trapped under turnover conditions with either propargyl alcohol or propargyl amine, the resting state is converted to one with an  $S = 1/2$  signal, similar to that observed when acetylene is used as substrate with WT enzyme. Such a well-defined EPR signal indicated that FeMo-co had been trapped with a single reduction intermediate bound in high occupancy, and thus an unprecedented opportunity to explore the properties of this intermediate by EPR and ENDOR spectroscopies was given.

$^{13}\text{C}$  ENDOR spectroscopy carried out on this intermediate generated with uniformly  $^{13}\text{C}$ -labeled propargyl alcohol gave signals from the three distinct C atoms of substrate with isotropic coupling to the FeMo-co spin in order of magnitude:  $\text{C}_3 > \text{C}_2 > \text{C}_1$  (Fig. 26A, C) [126]. This result established that the substrate-derived intermediate was covalently bound to metal ion(s) of the FeMo cofactor – that this state is bio-organometallic. However, even full determination of the  $^{13}\text{C}$  tensors

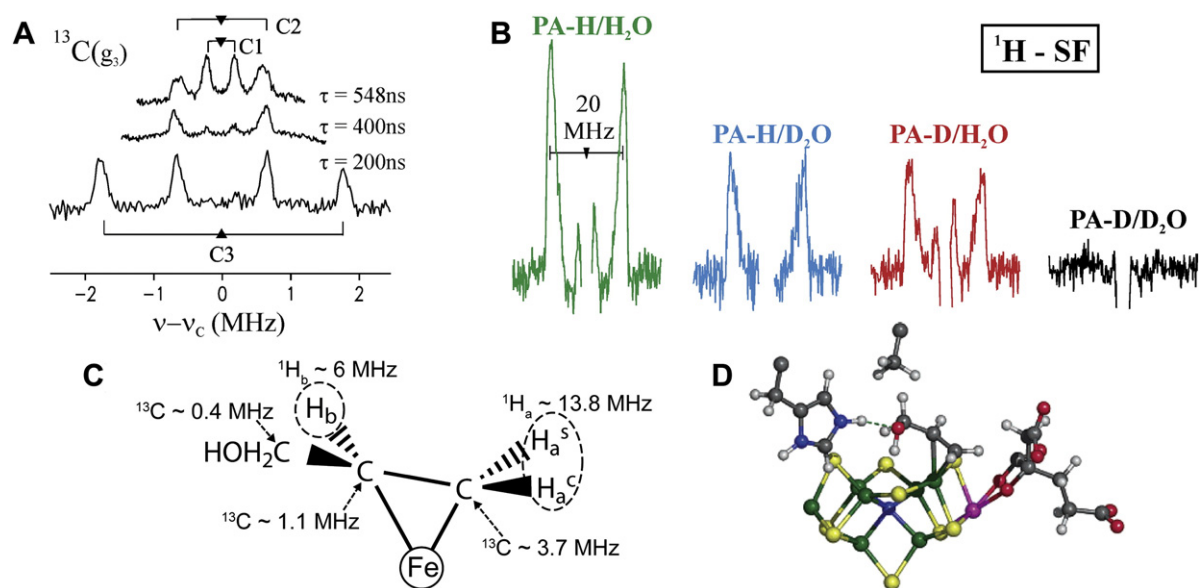


**Fig. 26.** A) Q-band ReMims and Mims pulsed  $^{13}\text{C}$  ENDOR of the FeMo-cofactor of the  $\alpha$ -70<sup>Ala</sup> MoFe protein under turnover with propargyl alcohol ( $\text{PA}^{13}\text{C}$ ). B) Quantitative stochastic field-modulated ENDOR spectra ( $^1\text{H}$ -SF) of the  $\alpha$ -70<sup>Ala</sup> MoFe protein same as in panel A. The deuteration patterns are indicated; spectra are centered at the  $^1\text{H}$  frequency and split by the hyperfine coupling. Key observation is that the intensity for the nondeuterated sample (green) is halved when either  $\text{D}_2\text{O}$  is used as solvent (blue) or the substrate is deuterated (red) and eliminated when deuterated substrate is used in  $\text{D}_2\text{O}$  (black). These results show that the bound intermediate contains two strongly coupled, magnetically identical protons, one that originates from substrate, the other from solvent. A third, weakly coupled proton is seen in the red and green spectra originating from the solvent. C) Proposed structure of the trapped propargyl alcohol reduction intermediate. D) Proposed structure for the trapped propargyl alcohol reduction intermediate bound to FeMo cofactor. The alkane unit of allyl alcohol is bound to Fe6 of the FeMo cofactor.

through analysis of 2D field-frequency patterns could not reveal the structure of the complex.

The nature of the bound intermediate instead was revealed by a detailed examination of the  $^1\text{H}$  ENDOR responses from the four isotopomers generated when H- or D-labeled propargyl alcohol (PA-H; PA-D) were used as substrate during turnover in either  $\text{H}_2\text{O}$  or  $\text{D}_2\text{O}$  [200]. Key was the combined use of a newly developed, *quantitative*  $^1\text{H}$  ENDOR technique, stochastic field-modulated (SF) CW ENDOR, in conjunction with Mims-pulsed  $^2\text{H}$  ENDOR, to study a strongly-coupled proton signal ( $\text{H}_a$ ) observed in the PA-H/ $\text{H}_2\text{O}$  spectrum (hyperfine coupling of  $A(^1\text{H}_a) \approx 20$  MHz) in the four isotopologs. As shown in Fig. 26B, the signal observed for PA-H/ $\text{H}_2\text{O}$  appears with half intensity in the spectra of *both* the PA-H/ $\text{D}_2\text{O}$  and PA-D/ $\text{H}_2\text{O}$  samples, and it is lost with the “doubly deuterated” PA-D/ $\text{D}_2\text{O}$  sample. Correspondingly the Mims  $^2\text{H}$  ENDOR spectrum of PA-D/ $\text{D}_2\text{O}$  was seen with half the intensity for PA-H/ $\text{D}_2\text{O}$  and PA-D/ $\text{H}_2\text{O}$  and was absent for PA-H/ $\text{H}_2\text{O}$ . These observations imply that the  $\text{H}_a$  doublet in the PA-H/ $\text{H}_2\text{O}$  spectrum is the superposition of doublets from two magnetically *identical* and hence *symmetry-equivalent* (*mirror-symmetry*) protons, one derived from propargyl alcohol substrate ( $\text{H}^c$ ) and the other acquired from solvent ( $\text{H}^s$ ) during reduction. In addition, the experiments disclosed one weakly coupled proton ( $\text{H}_b$ ) derived from solvent.

Detailed examination of the structures of inorganic model compounds having similar compositions showed that these  $^1\text{H}$  ENDOR measurements require that this intermediate is a complex of the alkene product of reduction, allyl alcohol, bound in a three-membered ring made up of the propargyl alcohol C3 and C2 atoms and a single Fe atom. Fig. 26C, a structure that can be viewed as either a ferracyclopropane adduct or a  $\pi$  complex of the allyl alcohol alkene product. Density functional theory (DFT) calculations on FeMo-co subsequently confirmed the structure [201]. Further work led to a proposed detailed bonding geometry of the cofactor-reduction intermediate shown in Fig. 26D.

This mechanistic insight into the reduction of an organic substrate is one component of the organometallic character of PA-FeMoco. This ferracycle structure was crucial in providing the basis for deriving the mechanism of IspG/IspH, as described next. Such bioorganometallic

species may become more widely found in nature, with advanced EPR techniques being crucial in their identification.

#### 5.2.10. Isoprene precursor synthesis through organometallic intermediates

The synthesis of isoprene precursors, which include carotenoids, cholesterol, steroid hormones, vitamins, and quinones, by eubacteria and apicomplexan parasites occurs solely via the methyl-erythritol phosphate (MEP) pathway [202,203]. Pathogenic microorganisms such as the causative agents of anthrax, plague, gastrointestinal ulcers, venereal diseases, malaria, and tuberculosis also solely depend on the MEP pathway for isoprenoid precursor production, making the MEP pathway an attractive target for the development of new drugs [204,205]. The last two steps in the MEP pathway, shown in Fig. 27, involve the proteins IspG ((*E*)-4-hydroxy-3-methylbut-2-enyl diphosphate synthase), initially known as GcpE [206,207], and IspH ((*E*)-1-hydroxy-2-methylbut-2-enyl 4-diphosphate reductase), initially known as LytB [208].

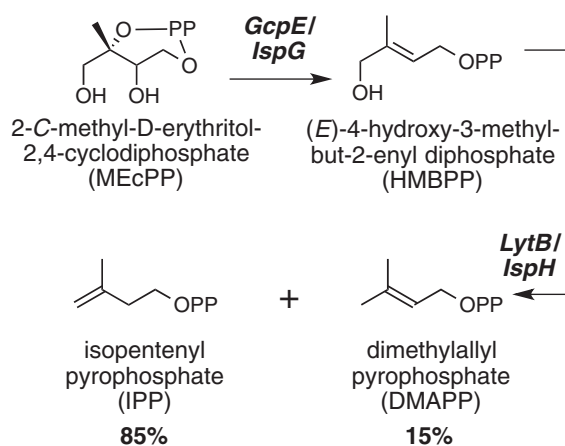


**Fig. 27.** The conversions of MEcPP to HMBPP by GcpE/IspG and HMBPP to DMAPP or IPP by LytB/IspH as part of the methyl-erythritol phosphate (MEP) pathway.

Both IspG and IspH catalyze  $2\text{H}^+/2\text{e}^-$  reductions of their substrates through organometallic intermediates, which have been characterized through advanced EPR techniques by two separate groups: the collaborative team of Duin (Auburn Univ.) and Hoffman (Northwestern Univ.); and Oldfield (Univ. of Illinois, Urbana-Champaign).

Initial ENDOR and HYSCORE studies by Oldfield and colleagues [209] attempted to shed light on the conversion of 2-C-methyl-D-erythritol-2,4-cyclodiphosphate (MEcPP) to (*E*)-4-hydroxy-3-methyl-but-2-enyl diphosphate (HMBPP) by IspG. To test a previously proposed reaction mechanism involving an epoxide [206], Oldfield compared the EPR, ENDOR, and HYSCORE spectroscopic characteristics of IspG with MEcPP or HMBPP binding, under turnover conditions and with a 2,3-HMBPP epoxide bound. Through uniform  $^2\text{H}$  and both uniform and partial  $^{13}\text{C}$  isotopic labeling of the MEcPP, the binding of substrate to the unique fourth iron was narrowed to occur via either 2C – or – 3C. A similar  $\pi/\sigma$  binding scheme for propargyl alcohol (PA) to the 7Fe9SMoC cluster (FeMo-co) of nitrogenase had earlier been described by Hoffman et al.; C1 exhibits  $^{13}\text{C}$  couplings of  $a_{\text{iso}} = 3.7$  MHz [200]. Taking as a model the work on propargyl alcohol bound to FeMo-co, Oldfield et al. proposed that the inhibition of IspG by alkynes results from their binding in an analogous organometallic  $\pi/\sigma$  fashion.

Duin and Hoffman [210] observed a strong  $^1\text{H}$  ENDOR response in IspG with MEcPP, and proposed that it arose from the C2' methyl group of MEcPP. This proposal was later confirmed by Oldfield through use of the isotopologue with  $^2\text{H}$  at C2' [185]. Further studies with individual atom isotopic labeling confirmed that C2 is the carbon most strongly coupled to the FeS cluster and the strong  $^1\text{H}$  response is from the C2' methyl group [185]. This supported the structure proposed by Duin and Hoffman, where “a ferraooxetane with an Fe–C2 bond (Fig. 28) also considered by Wang et al. [209] although not favored (by Oldfield), might be expected to have a large coupling to  $^{13}\text{C}$  and its  $\alpha$  proton...”

Subsequent studies by Oldfield involved  $^{17}\text{O}$  labeling of the hydroxyl group of MEcPP and the use of HYSCORE spectroscopy, which exhibited a strongly coupled  $^{17}\text{O}$  nucleus [211], indication of a strong Fe–O interaction. Taken together, the  $^1\text{H}/^2\text{H}$  [210],  $^{13}\text{C}$ , and  $^{17}\text{O}$  [185] ENDOR data create a consensus that IspG reacts via the ferraooxetane intermediate structure of Duin.

Following the production of HMBPP, IspH catalyzes its reduction into isopentenyl diphosphate and dimethylallyl diphosphate in ratios of 4:1 to 6:1 during the last step of the methylerythritol phosphate pathway [212].

Initial characterization of IspH inhibitors by Oldfield yielded the highest inhibition of activity by alkynyl diphosphate, which was proposed to bind to the unique iron of the [4Fe4S] cluster as a  $\pi$  (or  $\pi/\sigma$ ) metallocycle complex [213]. Later  $^{13}\text{C}$  ENDOR spectroscopy, also by Oldfield [211], revealed couplings once again similar to that observed for PA bound to nitrogenase. The analogy of the observed couplings with those for the PA properties, taken with the alkene inhibition observation, led Oldfield to propose a  $\pi/\sigma$  “metallacycle” or  $\eta_2$ -alkenyl complex [211].

Later ENDOR spectroscopic studies by Hoffman and colleagues of freeze-quenched samples of the wild-type and mutant enzymes confirmed the binding of the HMBPP substrate to IspH through the observation of weak  $^{31}\text{P}$  hyperfine dipolar couplings,  $A_{\text{max}} = 0.17$  MHz [214]. A dipolar interaction with no isotropic contributions may be treated as a point-dipole with the Fe–S cluster as a single point, and allows for reliable distance measurements to be made for distant nuclei, yielding an Fe– $^{31}\text{P}$  distance of  $r \sim 7$  Å [214]. These measurements initiated the assembly of the coordination sphere around the [4Fe4S] cluster. Analogous dipolar distance determinations were made for the racemate mixture of a single  $^2\text{H}$  label at the same carbon position as the hydroxyl group is attached, C1 (Fig. 28), of HMBPP. This deuteron creates a new ENDOR ‘probe’ on the opposite end of the substrate from the  $^{31}\text{P}$  of the phosphate group. Its  $^2\text{H}$  ENDOR signal gives a calculated distance of  $r(\text{Fe}-^2\text{H}) = 3.4$  Å, implying that this carbon with the hydroxyl group is adjacent to site of linkage to the FeS cluster. HMBPP is bound through either the hydroxyl or as a  $\pi$  complex with a Fe–O linkage of the freeze-trapped intermediate [214].

Isotopic labeling by Oldfield of the hydroxyl group of HMBPP with  $^{17}\text{O}$  yielded weak  $^{17}\text{O}$  hyperfine couplings, compared to IspG, implying the absence of direct Fe–O bonding [215,216]. This eliminated the possibility of binding through the hydroxyl group for the structure observed by Oldfield, contrasting with the freeze-trapped structure proposed by Duin and Hoffman. However,  $\pi$  binding of the allyl groups is still a viable mechanism, as previously suggested by Duin and Hoffman [214]. The final mechanism proposed by Oldfield, partially supported by crystallography [217], discarded the possibility of the ferraooxetane, but instead supports an  $\eta$ -3 allyl anion mechanism. Through the combined methods of crystallography and advanced EPR, Groll and Oldfield have made additional studies of the inhibitors of IspG and IspH and their organometallic binding modes [215–219].

## 6. Outlook

Advanced EPR techniques, namely ENDOR, and ESEEM and HYSCORE spectroscopies, have been crucial in understanding FeS proteins from the early days of their discovery. ENDOR, along with EPR and Mössbauer, was decisive in understanding the nature of magnetic coupling in ferredoxin FeS clusters that gave rise to their varying electron spin states. This in turn was connected to their redox properties, the only role initially assigned to FeS proteins. ENDOR also was essential in analyzing more complicated FeS systems, specifically nitrogenase FeMo-co, wherein the Fe and Mo sites were identified and quantified. The next phase was the key role played by ENDOR in demonstrating that an FeS cluster, in the citric acid cycle enzyme aconitase, was the catalytically active site for an organic transformation. Since then, advanced EPR techniques have gone in tandem with the biochemical progress on FeS proteins. Notable examples include work on unraveling the structure and mechanism of FeFe hydrogenase and on nitrogenase, wherein the tools of molecular biology and enzymology allowed the characterization of enzyme intermediates that has led to a deeper understanding

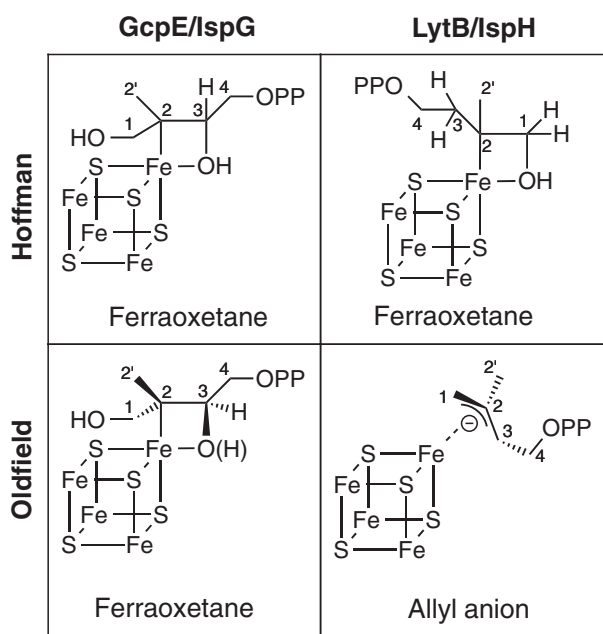


**Fig. 28.** Proposed intermediate structures of GcpE/IspG (left) and LytB/IspH (right) by Duin and coworkers (top) [210,214] and Oldfield and coworkers (bottom) [209,215,216]. Atom numbering follows that of MEcPP substrate for consistency.

of the mechanism of biological nitrogen fixation, and that an authentic organometallic moiety can exist on an FeS cluster. Another phase in the saga of FeS proteins is the identification of the radical SAM superfamily, whose membership and variety of chemical catalysis is constantly growing. Here again, ENDOR and ESEEM and HYSORE have all been instrumental in directly providing information that has allowed mechanism to be proposed for quite intricate organic reactions. The preparation of suitable isotopologs of substrates/inhibitors – many of which could be useful for NMR studies in other contexts, is also an important part of this progress. We conclude by expressing the belief that as long as biochemists are working on FeS proteins, practitioners of advanced EPR spectroscopic techniques can make major contributions to advance this important field.

### Conflict of interest statement

The authors do not declare any conflicts of interests.

### Acknowledgements

The authors thank Jacques Meyer for helpful conversations and careful reading of this manuscript. The authors also thank Jacques Meyer for providing the *A. aeolicus* Fd1 sample, Jose Moura, UNL, Lisbon, Portugal for the sample of *Desulfovibrio gigas* Fd, and Mary Claire Kennedy, Medical College of Wisconsin, for the sample of *Ectothiorhodospira halophila* HiPIP. This work was supported by the National Institutes of Health (GM111097 to B.M.H.) and the National Science Foundation (MCB-1118613 to B.M.H., and DGE-0824162 to G.E.C.).

### References

- R.H. Sands, H. Beinert, Studies on mitochondria and submitochondrial particles by paramagnetic resonance (EPR) spectroscopy, *Biochem. Biophys. Res. Commun.* 3 (1960) 47–52.
- Y.I. Shethna, P.W. Wilson, R.E. Hansen, H. Beinert, Identification by isotopic substitution of EPR signal at  $g = 1.94$  in non-heme iron protein from *Azotobacter*, *Proc. Natl. Acad. Sci.* 52 (1964) 1263–1271.
- G. Feher, Observation of nuclear magnetic resonances via the electron spin resonance line, *Phys. Rev.* 103 (1956) 834–835.
- G. Feher, Electron spin resonance experiments on donors in silicon. I. Electronic structure of donors by the electron nuclear double resonance technique, *Phys. Rev.* 114 (1959) 1219–1244.
- J. Lambe, N. Laurance, E.C. McIrvine, R.W. Terhune, Mechanisms of double resonance in solids, *Phys. Rev.* 122 (1961) 1161–1170.
- W.B. Mims, Pulsed endor experiments, *Proc. R. Soc. Lond.* 283 (1965) 452–457.
- J. Fritz, R. Anderson, J. Fee, G. Palmer, R.H. Sands, J.C. Tsibris, I.C. Gunsalus, W.H. Orme-Johnson, H. Beinert, The iron electron-nuclear double resonance (ENDOR) of two-iron ferredoxins from spinach, parsley, pig adrenal cortex and *Pseudomonas putida*, *Biochim. Biophys. Acta* 253 (1971) 110–133.
- R. Anderson, W.R. Dunham, R.H. Sands, A.J. Bearden, H.L. Crespi, On the nature of the iron sulfur cluster in a deuterated algal ferredoxin, *Q. Rev. Biophys.* 7 (1975) 443–504.
- A. Abragam, B. Bleaney, *Electron Paramagnetic Resonance of Transition Ions*, Dover Publications, New York, 1986.
- A. Schweiger, Pulsed electron spin resonance spectroscopy: basic principles, techniques, and examples of applications, *Angew. Chem. Int. Ed. Engl.* 30 (1991) 265–292.
- J. Weil, J. Bolton, *Electron Paramagnetic Resonance*, 2nd ed., 2011.
- K. Möbius, W. Lubitz, ENDOR spectroscopy in photobiology and biochemistry, *Biological Magnetic Resonance*, Springer US, Boston, MA, 1987, pp. 129–247.
- B.M. Hoffman, Electron nuclear double resonance (ENDOR) of metalloenzymes, *Acc. Chem. Res.* 24 (1991) 164–170.
- B.M. Hoffman, ENDOR of metalloenzymes, *Acc. Chem. Res.* 36 (2003) 522–529.
- A. Schweiger, Electron nuclear double resonance of transition metal complexes with organic ligands, *Electron Nuclear Double Resonance of Transition Metal Complexes with Organic Ligands*, vol. 51, Springer, Berlin Heidelberg, Berlin, Heidelberg, 1982, pp. 1–119.
- V.J. DeRose, B.M. Hoffman, Protein structure and mechanism studied by electron nuclear double resonance spectroscopy, in: K. Sauer (Ed.), *Methods in Enzymology*, vol. 246, Academic Press, New York, 1995, pp. 554–589.
- L. Noodleman, C.Y. Peng, D.A. Case, J.M. Mousesca, Orbital interactions, electron delocalization and spin coupling in iron-sulfur clusters, *Coord. Chem. Rev.* 144 (1995) 199–244.
- J.M. Mousesca, L. Noodleman, D.A. Case, B. Lamotte, Spin densities and spin coupling in iron-sulfur clusters: a new analysis of hyperfine coupling constants, *Inorg. Chem.* 34 (1995) 4347–4359.
- J. Telsler, H. Huang, H.-I. Lee, M.W.W. Adams, B.M. Hoffman, Site valencies and spin coupling in the 3Fe and 4Fe ( $S = 1/2$ ) clusters of *Pyrococcus furiosus* ferredoxin by  $^{57}\text{Fe}$  ENDOR, *J. Am. Chem. Soc.* 120 (1998) 861–870.
- G.E. Cutsail III, P.E. Doan, B.M. Hoffman, J. Meyer, J. Telsler, EPR and  $^{57}\text{Fe}$  ENDOR investigation of 2Fe ferredoxins from *Aquifex aeolicus*, *J. Biol. Inorg. Chem.* 17 (2012) 1137–1150.
- H.-I. Lee, B.J. Hales, B.M. Hoffman, Metal-ion valencies of the FeMo cofactor in CO-inhibited and resting state nitrogenase by  $^{57}\text{Fe}$  Q-band ENDOR, *J. Am. Chem. Soc.* 119 (1997) 11395–11400.
- P. Manikandan, E.Y. Choi, R. Hille, B.M. Hoffman, 35 GHz ENDOR characterization of the “very rapid” signal of xanthine oxidase reacted with 2-hydroxy-6-methylpurine ( $^{13}\text{C}_8$ ): evidence against direct Mo–C8 interaction, *J. Am. Chem. Soc.* 123 (2001) 2658–2663.
- C.A. Hutchison, D.B. McKay, The determination of hydrogen coordinates in lanthanum nicotinate dihydrate crystals by  $\text{Nd}^{3+}$ -proton double resonance, *J. Chem. Phys.* 66 (1977) 3311.
- E.A.C. Lucken, *Nuclear Quadrupole Coupling Constants*, Academic P, London, New York, 1969.
- W.B. Mims, J. Peisach, The nuclear modulation effect in electron spin echoes for complexes of  $\text{Cu}^{2+}$  and imidazole with  $^{14}\text{N}$  and  $^{15}\text{N}$ , *J. Chem. Phys.* 69 (1978) 4921.
- B.M. Hoffman, J. Martinsen, R.A. Venters, General theory of polycrystalline ENDOR patterns. g and hyperfine tensors of arbitrary symmetry and relative orientation, *J. Magn. Reson.* 59 (1984) 110–123.
- B.M. Hoffman, R.A. Venters, J. Martinsen, General theory of polycrystalline ENDOR patterns. Effects of finite EPR and ENDOR component linewidths, *J. Magn. Reson.* 62 (1985) 537–542.
- B.M. Hoffman, R.J. Gurbel, M.M. Werst, M. Sivaraja, Electron nuclear double resonance (ENDOR) of metalloenzymes, in: A.J. Hoff (Ed.), *Advanced EPR: Applications in Biology and Biochemistry*, Elsevier; Distributors for the U.S. and Canada, Elsevier Science Pub. Co., Amsterdam; New York New York, NY, U.S.A., 1989, p. xxii (918 pp.).
- P.E. Doan, The past, present, and future of orientation-selected ENDOR analysis: solving the challenges of dipolar-coupled nuclei, *Paramagnetic Resonance of Metallobiomolecules*, ACS Symposium Series, 2003.
- B. Epel, A. Poppl, P. Manikandan, S. Vega, D. Goldfarb, The effect of spin relaxation on ENDOR spectra recorded at high magnetic fields and low temperatures, *J. Magn. Reson.* 148 (2001) 388–397.
- B. Epel, D. Arieli, D. Baute, D. Goldfarb, Improving W-band pulsed ENDOR sensitivity—random acquisition and pulsed special TRIPLE, *J. Magn. Reson.* 164 (2003) 78–83.
- E.R. Davies, A new pulse ENDOR technique, *Phys. Lett. A* 47 (1974) 1–2.
- P.E. Doan, N.S. Lees, M. Shanmugam, B.M. Hoffman, Simulating suppression effects in pulsed ENDOR, and the ‘hole in the middle’ of Mims and Davies ENDOR spectra, *Appl. Magn. Reson.* 37 (2010) 763–779.
- A. Schweiger, G. Jeschke, *Principles of Pulse Electron Paramagnetic Resonance*, Oxford University Press, Oxford, UK; New York, 2001.
- C. Fan, P.E. Doan, C.E. Davoust, B.M. Hoffman, Quantitative studies of davies pulsed ENDOR, *J. Magn. Reson.* 98 (1992) 62–72.
- P.E. Doan, M.J. Nelson, B.M. Hoffman, Making hyperfine selection in Mims ENDOR independent of deadtime, *Chem. Phys. Lett.* 269 (1997) 208–214.
- C. Gemperle, A. Schweiger, Pulsed electron nuclear double-resonance methodology, *Chem. Rev.* 91 (1991) 1481–1505.
- R.A. Kinney, D.G.H. Hetterscheid, B.S. Hanna, R.R. Schrock, B.M. Hoffman, Formation of  $[\text{HIPTN}_3\text{N}]\text{Mo}(\text{III})\text{H}^-$  by heterolytic cleavage of  $\text{H}_2$  as established by EPR and ENDOR spectroscopy, *Inorg. Chem.* 49 (2010) 704–713.
- Y. Lee, R.A. Kinney, B.M. Hoffman, J.C. Peters, A nonclassical dihydrogen adduct of  $S = 1/2$  Fe(I), *J. Am. Chem. Soc.* 133 (2011) 16366–16369.
- P.E. Doan, M.J. Nelson, H. Jin, B.M. Hoffman, An implicit TRIPLE effect in Mims pulsed ENDOR: a sensitive new technique for determining signs of hyperfine couplings, *J. Am. Chem. Soc.* 118 (1996) 7014–7015.
- A. Silakov, E.J. Reijerse, S.P. Albracht, E.C. Hatchikian, W. Lubitz, The electronic structure of the H-cluster in the  $[\text{FeFe}]-\text{hydrogenase}$  from *Desulfovibrio desulfuricans*: a Q-band  $^{57}\text{Fe}$ -ENDOR and HYSORE study, *J. Am. Chem. Soc.* 129 (2007) 11447–11458.
- M.T. Bennebroek, J. Schmidt, Pulsed ENDOR spectroscopy at large thermal spin polarizations and the absolute sign of the hyperfine interaction, *J. Magn. Reson.* 128 (1997) 199–206.
- B. Epel, P. Manikandan, P.M.H. Kroneck, D. Goldfarb, High-field ENDOR and the sign of the hyperfine coupling, *Appl. Magn. Reson.* 21 (2001) 287–297.
- T.C. Yang, B.M. Hoffman, A Davies/Hahn multi-sequence for studies of spin relaxation in pulsed ENDOR, *J. Magn. Reson.* 181 (2006) 280–286.
- P.E. Doan, Combining steady-state and dynamic methods for determining absolute signs of hyperfine interactions: pulsed ENDOR saturation and recovery (PESTRE), *J. Magn. Reson.* 208 (2011) 76–86.
- P.E. Doan, J. Telsler, B.M. Barney, R.Y. Igarashi, D.R. Dean, L.C. Seefeldt, B.M. Hoffman,  $^{57}\text{Fe}$  ENDOR spectroscopy and ‘electron inventory’ analysis of the nitrogenase  $\text{E}_4$  intermediate suggest the metal-ion core of FeMo-cofactor cycles through only one redox couple, *J. Am. Chem. Soc.* 133 (2011) 17329–17340.
- J. Cowen, D. Kaplan, Spin-echo measurement of the spin-lattice and spin-spin relaxation in  $\text{Ce}^{3+}$  in lanthanum magnesium nitrate, *Phys. Rev.* 124 (1961) 1098–1101.
- W. Mims, K. Nassau, J. McGee, Spectral diffusion in electron resonance lines, *Phys. Rev.* 123 (1961) 2059–2069.
- L. Rowan, E. Hahn, W. Mims, Electron-spin-echo envelope modulation, *Phys. Rev.* 137 (1965) A61–A71.
- J. McCracken, *Electron spin echo envelope modulation (ESEEM) spectroscopy*, *Encyclopedia of Inorganic Chemistry*, John Wiley & Sons, Ltd., 2006

- [51] E. Hahn, Spin echoes, *Phys. Rev.* 80 (1950) 580–594.
- [52] R.P.J. Merks, R. De Beer, Two-dimensional Fourier transform of electron spin echo envelope modulation. An alternative for ENDOR, *J. Phys. Chem.* 83 (1979) 3319–3322.
- [53] P. Hofer, A. Grupp, M. Mehring, High-resolution time-domain electron-nuclear-sublevel spectroscopy by pulsed coherence transfer, *Phys. Rev. A* 33 (1986) 3519–3522.
- [54] S.A. Dikanov, M.K. Bowman, Cross-peak lineshape of two-dimensional ESEEM spectra in disordered  $S = 1/2$ ,  $I = 1/2$  spin systems, *J. Magn. Reson. Ser. A* 116 (1995) 125–128.
- [55] S.A. Dikanov, L. Xun, A.B. Karpel, A.M. Tyryshkin, M.K. Bowman, Orientationally-selected two-dimensional ESEEM spectroscopy of the Rieske-type iron–sulfur cluster in 2,4,5-trichlorophenoxyacetate monooxygenase from *Burkholderia cepacia* AC1100, *J. Am. Chem. Soc.* 118 (1996) 8408–8416.
- [56] Z.L. Madi, S. Van Doorslaer, A. Schweiger, Numerical simulation of one- and two-dimensional ESEEM experiments, *J. Magn. Reson.* 154 (2002) 181–191.
- [57] S. Stoll, A. Schweiger, Rapid construction of solid-state magnetic resonance powder spectra from frequencies and amplitudes as applied to ESEEM, *J. Magn. Reson.* 163 (2003) 248–256.
- [58] B.M. Hoffman, D.R. Dean, L.C. Seefeldt, Climbing nitrogenase: toward a mechanism of enzymatic nitrogen fixation, *Acc. Chem. Res.* 42 (2009) 609–619.
- [59] B.M. Hoffman, D. Lukoyanov, D.R. Dean, L.C. Seefeldt, Nitrogenase: a draft mechanism, *Acc. Chem. Res.* 46 (2013) 587–595.
- [60] B.M. Hoffman, D. Lukoyanov, Z.Y. Yang, D.R. Dean, L.C. Seefeldt, Mechanism of nitrogen fixation by nitrogenase: the next stage, *Chem. Rev.* 114 (2014) 4041–4062.
- [61] D. Lukoyanov, B.M. Barney, D.R. Dean, L.C. Seefeldt, B.M. Hoffman, Connecting nitrogenase intermediates with the kinetic scheme for  $N_2$  reduction by a relaxation protocol and identification of the  $N_2$  binding state, *Proc. Natl. Acad. Sci.* 104 (2007) 1451–1455.
- [62] D. Lukoyanov, Z.Y. Yang, B.M. Barney, D.R. Dean, L.C. Seefeldt, B.M. Hoffman, Unification of reaction pathway and kinetic scheme for  $N_2$  reduction catalyzed by nitrogenase, *Proc. Natl. Acad. Sci.* 109 (2012) 5583–5587.
- [63] M.P. Hendrich, P.G. Debrunner, Integer-spin electron paramagnetic resonance of iron proteins, *Biophys. J.* 56 (1989) 489–506.
- [64] E. Munck, K.K. Surerus, M.P. Hendrich, Combining Mössbauer spectroscopy with integer spin electron paramagnetic resonance, *Methods Enzymol.* 227 (1993) 463–479.
- [65] B.M. Hoffman, ENDOR and ESEEM of a non-Kramers doublet in an integer-spin system, *J. Phys. Chem.* 98 (1994) 11657–11665.
- [66] B.M. Hoffman, B.E. Sturgeon, P.E. Doan, V.J. DeRose, K.E. Liu, S.J. Lippard, ESEEM and ENDOR magnetic resonance studies of the non-Kramers doublet in the integer-spin diiron(II) forms of two methane monooxygenase hydroxylases and hemerythrin azide, *J. Am. Chem. Soc.* 116 (1994) 6023–6024.
- [67] B.E. Sturgeon, P.E. Doan, K.E. Liu, D. Burdi, W.H. Tong, J.M. Nocek, N. Gupta, J. Stubbe, J. Donald, M. Kurtz, S.J. Lippard, B.M. Hoffman, Non-Kramers ESEEM of integer-spin diferrous carboxylate-bridged clusters in proteins, *J. Am. Chem. Soc.* 119 (1997) 375–386.
- [68] K.M. Lancaster, M. Roemelt, P. Ettenhuber, Y. Hu, M.W. Ribbe, F. Neese, U. Bergmann, S. DeBeer, X-ray emission spectroscopy evidences a central carbon in the nitrogenase iron–molybdenum cofactor, *Science* 334 (2011) 974–977.
- [69] T. Spatzal, M. Aksoyoglu, L. Zhang, S.L. Andrade, E. Schleicher, S. Weber, D.C. Rees, O. Einsle, Evidence for interstitial carbon in nitrogenase FeMo cofactor, *Science* 334 (2011) 940.
- [70] J.A. Wiig, Y. Hu, C.C. Lee, M.W. Ribbe, Radical SAM-dependent carbon insertion into the nitrogenase M-cluster, *Science* 337 (2012) 1672–1675.
- [71] R.H. Sands, ENDOR and ELDOR on iron–sulfur proteins, in: M.M. Dorio, J.H. Freed (Eds.), *Multiple Electron Resonance Spectroscopy*, Plenum Press, New York & London, 1979, pp. 331–374.
- [72] B.R. Crouse, J. Meyer, M.K. Johnson, Spectroscopic evidence for a reduced  $Fe_2S_2$  cluster with a  $S = 9/2$  ground state in mutant forms of *Clostridium pasteurianum* 2Fe ferredoxin, *J. Am. Chem. Soc.* 117 (1995) 9612–9613.
- [73] L. Noodleman, J.G. Norman, J.H. Osborne, A. Aizman, D.A. Case, Models for ferredoxins: electronic structures of iron–sulfur clusters with one, two, and four iron atoms, *J. Am. Chem. Soc.* 107 (1985) 3418–3426.
- [74] C. Mailer, C.P. Taylor, Rapid adiabatic passage EPR of ferricytochrome c: signal enhancement and determination of the spin–lattice relaxation time, *Biochim. Biophys. Acta* 322 (1973) 195–203.
- [75] B.H. Huynh, T.A. Kent, Mössbauer studies of iron proteins, *Adv. Inorg. Biochem.* 6 (1984) 163–223.
- [76] T.A. Kent, J.L. Dreyer, M.C. Kennedy, B.H. Huynh, M.H. Emptage, H. Beinert, E. Munck, Mössbauer studies of beef heart aconitase: evidence for facile interconversions of iron–sulfur clusters, *Proc. Natl. Acad. Sci.* 79 (1982) 1096–1100.
- [77] G.J. Long, F. Grandjean, *Mössbauer Spectroscopy Applied to Inorganic Chemistry*, Plenum Press, New York, 1984.
- [78] M.M. Dicus, A. Conlan, R. Nechushtai, P.A. Jennings, M.L. Paddock, R.D. Britt, S. Stoll, Binding of histidine in the (Cys3)(His)1-coordinated [2Fe–2S] cluster of human mitoNEET, *J. Am. Chem. Soc.* 132 (2010) 2037–2049.
- [79] R.J. Gurbel, P.E. Doan, G.T. Gassner, T.J. Macke, D.A. Case, T. Ohnishi, J.A. Fee, D.P. Ballou, B.M. Hoffman, Active site structure of Rieske-type proteins: electron nuclear double resonance studies of isotopically labeled phthalate dioxygenase from *Pseudomonas cepacia* and Rieske protein from *Rhodobacter capsulatus* and molecular modeling studies of a Rieske center, *Biochemistry* 35 (1996) 7834–7845.
- [80] M. Orio, J.M. Mouesca, Variation of average g values and effective exchange coupling constants among [2Fe–2S] clusters: a density functional theory study of the impact of localization (trapping forces) versus delocalization (double-exchange) as competing factors, *Inorg. Chem.* 47 (2008) 5394–5416.
- [81] A.H. Priem, A.A. Klaassen, E.J. Reijerse, T.E. Meyer, C. Luchinat, F. Capozzi, W.R. Dunham, W.R. Hagen, EPR analysis of multiple forms of  $[4Fe–4S]^{3+}$  clusters in HiPIPs, *J. Biol. Inorg. Chem.* 10 (2005) 417–424.
- [82] R. Grazina, S.R. Pauleta, J.J.G. Moura, I. Moura, Iron–sulfur centers: new roles for ancient metal sites, in: J.R. Poeppelmeier (Ed.), *Comprehensive Inorganic Chemistry II*, Second edition Elsevier, Amsterdam, 2013, pp. 103–148.
- [83] M. Belinskii, Spin coupling model for tetrameric iron clusters in ferredoxins. I. Theory, exchange levels, g-factors, *Chem. Phys.* 172 (1993) 189–211.
- [84] D.C. Johnson, D.R. Dean, A.D. Smith, M.K. Johnson, Structure, function, and formation of biological iron–sulfur clusters, *Annu. Rev. Biochem.* 74 (2005) 247–281.
- [85] S.C. Lee, R.H. Holm, Speculative synthetic chemistry and the nitrogenase problem, *Proc. Natl. Acad. Sci.* 100 (2003) 3595–3600.
- [86] R.H. Holm, Trinuclear cuboidal heterometallic cubane-type iron–sulfur clusters: new structural and reactivity themes in chemistry and biology, *Adv. Inorg. Chem.* 38 (1992) 1–71.
- [87] R.H. Holm, S. Ciurli, J.A. Weigel, Subsite-specific structures and reactions in native and synthetic (4Fe–4S) cubane-type clusters, *Prog. Inorg. Chem.* 38 (1990) 1–74.
- [88] G. Rius, B. Lamotte, Single-crystal ENDOR study of a  $^{57}Fe$ -enriched iron–sulfur  $[Fe_4S_4]^{3+}$  cluster, *J. Am. Chem. Soc.* 111 (1989) 2464–2469.
- [89] J.-M. Mouesca, G. Rius, B. Lamotte, Single-crystal proton ENDOR studies of the  $[Fe_4S_4]^{3+}$  cluster: determination of the spin population distribution and proposal of a model to interpret the  $^1H$  NMR paramagnetic shifts in high-potential ferredoxins, *J. Am. Chem. Soc.* 115 (1993) 4714–4731.
- [90] J. Gloux, P. Gloux, B. Lamotte, J.-M. Mouesca, G. Rius, The different  $[Fe_4S_4]^{3+}$  and  $[Fe_4S_4]^{2+}$  species created by g irradiation in single crystals of the  $(Et_4N)_2 [Fe_4S_4(SBenz)_4]$  model compound: their EPR description and their biological significance, *J. Am. Chem. Soc.* 116 (1994) 1953–1961.
- [91] L. Noodleman, D.A. Case, J.M. Mouesca, B. Lamotte, Valence electron delocalization in polynuclear iron–sulfur clusters, *J. Biol. Inorg. Chem.* 1 (1996) 177–182.
- [92] L. Le Pape, B. Lamotte, J.-M. Mouesca, G. Rius, Paramagnetic states of four iron–four sulfur clusters. 1. EPR single-crystal study of 3+ and 1+ clusters of an asymmetrical model compound and general model for the interpretation of the g-tensors of these two redox states, *J. Am. Chem. Soc.* 119 (1997) 9757–9770.
- [93] L. Le Pape, B. Lamotte, J.-M. Mouesca, G. Rius, Paramagnetic states of four iron–four sulfur clusters. 2. Proton ENDOR study of a 1+ state in an asymmetrical cluster, *J. Am. Chem. Soc.* 119 (1997) 9771–9781.
- [94] R. Davydov, R. Kappl, J. Huttermann, J.A. Peterson, EPR-spectroscopy of reduced oxoferrous-P450cam, *FEBS Lett.* 295 (1991) 113–115.
- [95] S.A. Dikanov, R.M. Davydov, L. Xun, M.K. Bowman, CW and pulsed EPR characterization of the reduced Rieske type iron–sulfur center in 2,4,5-trichlorophenoxyacetate monooxygenase, *J. Magn. Reson.* 112 (1996) 289–294.
- [96] J. Telsler, R. Davydov, C.H. Kim, M.W.W. Adams, B.M. Hoffman, Investigation of the unusual electronic structure of *Pyrococcus furiosus* 4Fe ferredoxin by EPR spectroscopy of protein reduced at ambient and cryogenic temperatures, *Inorg. Chem.* 38 (1999) 3550–3553.
- [97] J. Gloux, P. Gloux, B. Lamotte, G. Rius, Creation and ESR identification, in single crystals, of synthetic analogs of the  $S = (1/2)$  states of the  $Fe_4S_4$  cores of the reduced ferredoxins and oxidized high-potential proteins, *Phys. Rev. Lett.* 54 (1985) 599–602.
- [98] F. Moriaud, S. Gambarelli, B. Lamotte, J.-M. Mouesca, Detailed proton Q-band ENDOR study of the electron spin population distribution in the reduced  $[4Fe–4S]^{1+}$  state, *J. Phys. Chem. B* 105 (2001) 9631–9642.
- [99] R.K. Thauer, A.K. Kaster, H. Seedorf, W. Buckel, R. Hedderich, Methanogenic archaea: ecologically relevant differences in energy conservation, *Nat. Rev. Microbiol.* 6 (2008) 579–591.
- [100] M. Simianu, E. Murakami, J.M. Brewer, S.W. Ragsdale, Purification and properties of the heme- and iron–sulfur-containing heterodisulfide reductase from *Methanosarcina thermophila*, *Biochemistry* 37 (1998) 10027–10039.
- [101] N. Hamann, G.J. Mander, J.E. Shokes, R.A. Scott, M. Bennati, R. Hedderich, A cysteine-rich CCG domain contains a novel [4Fe–4S] cluster binding motif as deduced from studies with subunit B of heterodisulfide reductase from *Methanothermobacter marburgensis*, *Biochemistry* 46 (2007) 12875–12885.
- [102] S. Madadi-Kahkesh, E.C. Duin, S. Heim, S.P. Albracht, M.K. Johnson, R. Hedderich, A paramagnetic species with unique EPR characteristics in the active site of heterodisulfide reductase from methanogenic archaea, *Eur. J. Biochem.* 268 (2001) 2566–2577.
- [103] E.C. Duin, C. Bauer, B. Jaun, R. Hedderich, Coenzyme M binds to a [4Fe–4S] cluster in the active site of heterodisulfide reductase as deduced from EPR studies with the  $[^{35}S]$ coenzyme M-treated enzyme, *FEBS Lett.* 538 (2003) 81–84.
- [104] E.C. Duin, S. Madadi-Kahkesh, R. Hedderich, M.D. Clay, M.K. Johnson, Heterodisulfide reductase from *Methanothermobacter marburgensis* contains an active-site [4Fe–4S] cluster that is directly involved in mediating heterodisulfide reduction, *FEBS Lett.* 512 (2002) 263–268.
- [105] M. Bennati, N. Weiden, K.P. Dinse, R. Hedderich,  $^{57}Fe$  ENDOR spectroscopy on the iron–sulfur cluster involved in substrate reduction of heterodisulfide reductase, *J. Am. Chem. Soc.* 126 (2004) 8378–8379.
- [106] A.J. Fielding, K. Parey, U. Ermler, S. Scheller, B. Jaun, M. Bennati, Advanced electron paramagnetic resonance on the catalytic iron–sulfur cluster bound to the CCG domain of heterodisulfide reductase and succinate: quinone reductase, *J. Biol. Inorg. Chem.* 18 (2013) 905–915.
- [107] P. Middleton, D.P. Dickson, C.E. Johnson, J.D. Rush, Interpretation of the Mössbauer spectra of the high-potential iron protein from *Chromatium*, *Eur. J. Biochem.* 104 (1980) 289–296.

- [108] W. Lubitz, H. Ogata, O. Rudiger, E. Reijerse, Hydrogenases, *Chem. Rev.* 114 (2014) 4081–4148.
- [109] J.W. Peters, W.N. Lanzilotta, B.J. Lemon, L.C. Seefeldt, X-ray crystal structure of the Fe-only hydrogenase (Cpl) from *Clostridium pasteurianum* to 1.8 angstrom resolution, *Science* 282 (1998) 1853–1858.
- [110] Y. Nicolet, C. Piras, P. Legrand, C.E. Hatchikian, J.C. Fontecilla-Camps, *Desulfovibrio desulfuricans* iron hydrogenase: the structure shows unusual coordination to an active site Fe binuclear center, *Structure* 7 (1999) 13–23.
- [111] A. Silakov, B. Wenk, E. Reijerse, S.P. Albracht, W. Lubitz, Spin distribution of the H-cluster in the H(ox)–CO state of the [FeFe] hydrogenase from *Desulfovibrio desulfuricans*: HYSCORE and ENDOR study of  $^{14}\text{N}$  and  $^{13}\text{C}$  nuclear interactions, *J. Biol. Inorg. Chem.* 14 (2009) 301–313.
- [112] J. Esselborn, C. Lambert, A. Adamska-Venkatesh, T. Simmons, G. Berggren, J. Noth, J. Siebel, A. Hemschemeier, V. Artero, E. Reijerse, M. Fontecave, W. Lubitz, T. Happe, Spontaneous activation of [FeFe]-hydrogenases by an inorganic [2Fe] active site mimic, *Nat. Chem. Biol.* 9 (2013) 607–609.
- [113] G. Berggren, A. Adamska, C. Lambert, T.R. Simmons, J. Esselborn, M. Atta, S. Gambarelli, J.M. Mouesca, E. Reijerse, W. Lubitz, T. Happe, V. Artero, M. Fontecave, Biomimetic assembly and activation of [FeFe]-hydrogenases, *Nature* 499 (2013) 66–69.
- [114] A. Silakov, B. Wenk, E. Reijerse, W. Lubitz,  $^{14}\text{N}$  HYSCORE investigation of the H-cluster of [FeFe] hydrogenase: evidence for a nitrogen in the dithiol bridge, *Phys. Chem. Chem. Phys.* 11 (2009) 6592–6599.
- [115] O.F. Erdem, L. Schwartz, M. Stein, A. Silakov, S. Kaur-Ghumaan, P. Huang, S. Ott, E.J. Reijerse, W. Lubitz, A model of the [FeFe] hydrogenase active site with a biologically relevant azadithiolate bridge: a spectroscopic and theoretical investigation, *Angew. Chem. Int. Ed. Engl.* 50 (2011) 1439–1443.
- [116] E.M. Shepard, F. Mus, J.N. Betz, A.S. Byer, B.R. Duffus, J.W. Peters, J.B. Broderick, [FeFe]-hydrogenase maturation, *Biochemistry* 53 (2014) 4090–4104.
- [117] J.M. Kuchenreuther, W.K. Myers, D.L. Suesst, T.A. Stich, V. Pelmeshnikov, S.A. Shiigi, S.P. Cramer, J.R. Swartz, R.D. Britt, S.J. George, The HydG enzyme generates an Fe(CO)<sub>2</sub>(CN) synthon in assembly of the FeFe hydrogenase H-cluster, *Science* 343 (2014) 424–427.
- [118] J.M. Kuchenreuther, W.K. Myers, T.A. Stich, S.J. George, Y. Nejatjahromy, J.R. Swartz, R.D. Britt, A radical intermediate in tyrosine scission to the CO and CN<sup>-</sup> ligands of FeFe hydrogenase, *Science* 342 (2013) 472–475.
- [119] J.M. Kuchenreuther, Y. Guo, H. Wang, W.K. Myers, S.J. George, C.A. Boyke, Y. Yoda, E.E. Alp, J. Zhao, R.D. Britt, J.R. Swartz, S.P. Cramer, Nuclear resonance vibrational spectroscopy and electron paramagnetic resonance spectroscopy of  $^{57}\text{Fe}$ -enriched [FeFe] hydrogenase indicate stepwise assembly of the H-cluster, *Biochemistry* 52 (2013) 818–826.
- [120] P. Berto, M. Di Valentin, L. Cendron, F. Vallese, M. Albertini, E. Salvadori, G.M. Giacometti, D. Carbonera, P. Costantini, The [4Fe–4S]-cluster coordination of [FeFe]-hydrogenase maturation protein HydF as revealed by EPR and HYSCORE spectroscopies, *Biochim. Biophys. Acta* 1817 (2012) 2149–2157.
- [121] T.A. Stich, W.K. Myers, R.D. Britt, Paramagnetic intermediates generated by radical S-adenosylmethionine (SAM) enzymes, *Acc. Chem. Res.* 47 (2014) 2235–2243.
- [122] T.R. Simmons, G. Berggren, M. Bacchi, M. Fontecave, V. Artero, Mimicking hydrogenases: from biomimetics to artificial enzymes, *Coord. Chem. Rev.* 270–271 (2014) 127–150.
- [123] C.H. Hsieh, O.F. Erdem, S.D. Harman, M.L. Singleton, E. Reijerse, W. Lubitz, C.V. Popescu, J.H. Reibenspies, S.M. Brothers, M.B. Hall, M.Y. Darensbourg, Structural and spectroscopic features of mixed valent Fe(II)Fe(I) complexes and factors related to the rotated configuration of diiron hydrogenase, *J. Am. Chem. Soc.* 134 (2012) 13089–13102.
- [124] S. Ogo, K. Ichikawa, T. Kishima, T. Matsumoto, H. Nakai, K. Kusaka, T. Ohhara, A functional [NiFe]hydrogenase mimic that catalyzes electron and hydride transfer from H<sub>2</sub>, *Science* 339 (2013) 682–684.
- [125] W. Lubitz, E. Reijerse, M. van Gastel, [NiFe] and [FeFe] hydrogenases studied by advanced magnetic resonance techniques, *Chem. Rev.* 107 (2007) 4331–4365.
- [126] P.C. Dos Santos, R.Y. Igarashi, H.I. Lee, B.M. Hoffman, L.C. Seefeldt, D.R. Dean, Substrate interactions with the nitrogenase active site, *Acc. Chem. Res.* 38 (2005) 208–214.
- [127] B.M. Hoffman, R.A. Venters, J.E. Roberts, M. Nelson, W.H. Orme-Johnson,  $^{57}\text{Fe}$  ENDOR of the nitrogenase MoFe protein, *J. Am. Chem. Soc.* 104 (1982) 4711–4712.
- [128] R.A. Venters, M.J. Nelson, P.A. Mclean, A.E. True, M.A. Levy, B.M. Hoffman, W.H. Orme-Johnson, ENDOR of the resting state of nitrogenase molybdenum iron proteins from *Azotobacter vinelandii*, *Klebsiella pneumoniae*, and *Clostridium pasteurianum* —  $^1\text{H}$ ,  $^{57}\text{Fe}$ ,  $^{95}\text{Mo}$ , and  $^{33}\text{S}$  studies, *J. Am. Chem. Soc.* 108 (1986) 3487–3498.
- [129] A.E. True, M.J. Nelson, R.A. Venters, W.H. Orme-Johnson, B.M. Hoffman,  $^{57}\text{Fe}$  hyperfine coupling tensors of the FeMo cluster in *Azotobacter vinelandii* MoFe protein: determination by polycrystalline ENDOR spectroscopy, *J. Am. Chem. Soc.* 110 (1988) 1935–1943.
- [130] S.J. Yoo, H.C. Angove, V. Papaefthymiou, B.K. Burgess, E. Münck, Mössbauer study of the MoFe protein of nitrogenase from *Azotobacter vinelandii* using selective  $^{57}\text{Fe}$  enrichment of the M-centers, *J. Am. Chem. Soc.* 122 (2000) 4926–4936.
- [131] R.C. Pollock, H.-I. Lee, L.M. Cameron, V.J. DeRose, B.J. Hales, W.H. Orme-Johnson, B.M. Hoffman, Investigation of CO bound to inhibited forms of nitrogenase MoFe protein by  $^{13}\text{C}$  ENDOR, *J. Am. Chem. Soc.* 117 (1995) 8686–8687.
- [132] P.D. Christie, H.I. Lee, L.M. Cameron, B.J. Hales, W.H. Orme-Johnson, B.M. Hoffman, Identification of the CO-binding cluster in nitrogenase MoFe protein by ENDOR of Fe-57 isotopomers, *J. Am. Chem. Soc.* 118 (1996) 8707–8709.
- [133] R.N.F. Thorneley, D.J. Lowe, Nitrogenase: substrate binding and activation, *J. Biol. Inorg. Chem.* 1 (1996) 576–580.
- [134] R.Y. Igarashi, M. Laryukhin, P.C. Dos Santos, H.I. Lee, D.R. Dean, L.C. Seefeldt, B.M. Hoffman, Trapping H<sup>-</sup> bound to the nitrogenase FeMo-cofactor active site during H<sub>2</sub> evolution: characterization by ENDOR spectroscopy, *J. Am. Chem. Soc.* 127 (1995) 6231–6241.
- [135] D. Lukoyanov, Z.Y. Yang, D.R. Dean, L.C. Seefeldt, B.M. Hoffman, Is Mo involved in hydride binding by the four-electron reduced (E<sub>4</sub>) intermediate of the nitrogenase MoFe protein? *J. Am. Chem. Soc.* 132 (2010) 2526–2527.
- [136] S. Shaw, D. Lukoyanov, K. Danylak, D.R. Dean, B.M. Hoffman, L.C. Seefeldt, Nitrite and hydroxylamine as nitrogenase substrates: mechanistic implications for the pathway of N<sub>2</sub> reduction, *J. Am. Chem. Soc.* 136 (2014) 12776–12783.
- [137] M.M. Werst, M.C. Kennedy, A.L.P. Houseman, H. Beinert, B.M. Hoffman, Characterization of the iron–sulfur [4Fe–4S]<sup>+</sup> cluster at the active site of aconitase by  $^{57}\text{Fe}$ ,  $^{33}\text{S}$ , and  $^{14}\text{N}$  electron nuclear double resonance spectroscopy, *Biochemistry* 29 (1990) 10533–10540.
- [138] A.H. Robbins, C.D. Stout, Structure of activated aconitase: formation of the [4Fe–4S] cluster in the crystal, *Proc. Natl. Acad. Sci.* 86 (1989) 3639–3643.
- [139] W.H. Orme-Johnson, R.E. Hansen, H. Beinert, J.C. Tisbriss, R.C. Bartholomew, I.C. Gunsalus, On the sulfur components of iron–sulfur proteins. I. The number of acid-labile sulfur groups sharing an unpaired electron with iron, *Proc. Natl. Acad. Sci.* 60 (1968) 368–372.
- [140] J. Meyer, Ferredoxins of the third kind, *FEBS Lett.* 509 (2001) 1–5.
- [141] J. Meyer, Iron–sulfur protein folds, iron–sulfur chemistry, and evolution, *J. Biol. Inorg. Chem.* 13 (2008) 157–170.
- [142] D.O. Hearshen, W.R. Hagen, R.H. Sands, H.J. Grande, H.L. Crespi, I.C. Gunsalus, W.R. Dunham, An analysis of g strain in the EPR of two [2Fe–2S] ferredoxins. Evidence for a protein rigidity model, *J. Magn. Reson.* 69 (1986) 440–459.
- [143] A.P. Yeh, X.I. Ambroggio, S.L. Andrade, O. Einsle, C. Chatelet, J. Meyer, D.C. Rees, High resolution crystal structures of the wild type and Cys-55 → Ser and Cys-59 → Ser variants of the thioredoxin-like [2Fe–2S] ferredoxin from *Aquifex aeolicus*, *J. Biol. Chem.* 277 (2002) 34499–34507.
- [144] H. Li, D.T. Mapolelo, N.N. Dingra, S.G. Naik, N.S. Lees, B.M. Hoffman, P.J. Riggs-Gelasco, B.H. Huynh, M.K. Johnson, C.E. Outten, The yeast iron regulatory proteins Grx3/4 and Fra2 form heterodimeric complexes containing a [2Fe–2S] cluster with cysteinyl and histidyl ligation, *Biochemistry* 48 (2009) 9569–9581.
- [145] M.L. Paddock, S.E. Wiley, H.L. Axelrod, A.E. Cohen, M. Roy, E.C. Abresch, D. Capraro, A.N. Murphy, R. Nechushtai, J.E. Dixon, P.A. Jennings, MitoNEET is a uniquely folded 2Fe 2S outer mitochondrial membrane protein stabilized by pioglitazone, *Proc. Natl. Acad. Sci.* 104 (2007) 14342–14347.
- [146] J.R. Colca, W.G. McDonald, D.J. Waldon, J.W. Leone, J.M. Lull, C.A. Bannow, E.T. Lund, W.R. Mathews, Identification of a novel mitochondrial protein (“mitoNEET”) cross-linked specifically by a thiazolidinedione photoprobe, *Am. J. Physiol. Endocrinol. Metab.* 286 (2004) E252–E260.
- [147] S.E. Wiley, A.N. Murphy, S.A. Ross, P. van der Geer, J.E. Dixon, MitoNEET is an iron-containing outer mitochondrial membrane protein that regulates oxidative capacity, *Proc. Natl. Acad. Sci.* 104 (2007) 5318–5323.
- [148] P. Berstrand, J.P. Gayda, J.A. Fee, D. Kuila, R. Cammack, Comparison of the spin–lattice relaxation properties of the two classes of [2Fe–2S] clusters in proteins, *Biochim. Biophys. Acta* 916 (1987) 24–28.
- [149] M.K. Bowman, E.A. Berry, A.G. Roberts, D.M. Kramer, Orientation of the g-tensor axes of the Rieske subunit in the cytochrome bc<sub>1</sub> complex, *Biochemistry* 43 (2004) 430–436.
- [150] J.A. Fee, K.L. Findling, T. Yoshida, R. Hille, G.E. Tarr, D.O. Hearshen, W.R. Dunham, E.P. Day, T.A. Kent, E. Munck, Purification and characterization of the Rieske iron–sulfur protein from *Thermus thermophilus*. Evidence for a [2Fe–2S] cluster having non-cysteine ligands, *J. Biol. Chem.* 259 (1984) 124–133.
- [151] R. Kappel, M. Ebelhäuser, F. Hannemann, R. Bernhardt, J. Hüttermann, Probing electronic and structural properties of the reduced [2Fe–2S] cluster by orientation-selective  $^1\text{H}$  ENDOR spectroscopy: adenodocus versus Rieske iron–sulfur protein, *Appl. Magn. Reson.* 30 (2006) 427–459.
- [152] D.R. Kolling, R.I. Samoilova, A.A. Shubin, A.R. Crofts, S.A. Dikanov, Proton environment of reduced Rieske iron–sulfur cluster probed by two-dimensional ESEEM spectroscopy, *J. Phys. Chem. A* 113 (2009) 653–667.
- [153] C.J. Fugate, T.A. Stich, E.G. Kim, W.K. Myers, R.D. Britt, J.T. Jarrett, 9-Mercaptodethiobiotin is generated as a ligand to the [2Fe–2S]<sup>+</sup> cluster during the reaction catalyzed by biotin synthase from *Escherichia coli*, *J. Am. Chem. Soc.* 134 (2012) 9042–9045.
- [154] C.J. Fugate, J.T. Jarrett, Biotin synthase: insights into radical-mediated carbon–sulfur bond formation, *Biochim. Biophys. Acta* 1824 (2012) 1213–1222.
- [155] F. Berkovitch, Y. Nicolet, J.T. Wan, J.T. Jarrett, C.L. Drennan, Crystal structure of biotin synthase, an S-adenosylmethionine-dependent radical enzyme, *Science* 303 (2004) 76–79.
- [156] A.M. Taylor, S. Stoll, R.D. Britt, J.T. Jarrett, Reduction of the [2Fe–2S] cluster accompanies formation of the intermediate 9-mercaptodethiobiotin in *Escherichia coli* biotin synthase, *Biochemistry* 50 (2011) 7953–7963.
- [157] J.S. Rieske, D.H. MacLennan, R. Coleman, Isolation and properties of an iron–protein from the (reduced coenzyme Q)–cytochrome C reductase complex of the respiratory chain, *Biochem. Biophys. Res. Commun.* 15 (1964) 338–344.
- [158] J.F. Gibson, D.O. Hall, J.H. Thornley, F.R. Whately, The iron complex in spinach ferredoxin, *Proc. Natl. Acad. Sci.* 56 (1966) 987–990.
- [159] W. Mims, Envelope modulation in spin–echo experiments, *Phys. Rev. B* 5 (1972) 2409–2419.
- [160] H. Beinert, M.C. Kennedy, C.D. Stout, Aconitase as iron–sulfur protein, enzyme, and iron-regulatory protein, *Chem. Rev.* 96 (1996) 2335–2374.

- [161] J. Telser, M.H. Emptage, H. Merkle, M.C. Kennedy, H. Beinert, B.M. Hoffman,  $^{17}\text{O}$  electron nuclear double resonance characterization of substrate binding to the  $[\text{4Fe-4S}]^{2+}$  cluster of reduced active aconitase, *J. Biol. Chem.* 261 (1986) 4840–4846.
- [162] M.C. Kennedy, M. Werst, J. Telser, M.H. Emptage, H. Beinert, B.M. Hoffman, Mode of substrate carboxyl binding to the  $[\text{4Fe-4S}]^{2+}$  cluster of reduced aconitase as studied by  $^{17}\text{O}$  and  $^{13}\text{C}$  electron-nuclear double resonance spectroscopy, *Proc. Natl. Acad. Sci.* 84 (1987) 8854–8858.
- [163] M.M. Werst, M.C. Kennedy, H. Beinert, B.M. Hoffman,  $^{17}\text{O}$ ,  $^1\text{H}$ , and  $^2\text{H}$  electron nuclear double resonance characterization of solvent, substrate, and inhibitor binding to the  $[\text{4Fe-4S}]^{2+}$  cluster of aconitase, *Biochemistry* 29 (1990) 10526–10532.
- [164] T.A. Kent, M.H. Emptage, H. Merkle, M.C. Kennedy, H. Beinert, E. Munck, Mössbauer studies of aconitase. Substrate and inhibitor binding, reaction intermediates, and hyperfine interactions of reduced 3Fe and 4Fe clusters, *J. Biol. Chem.* 260 (1985) 6871–6881.
- [165] A.H. Robbins, C.D. Stout, The structure of aconitase, *Proteins* 5 (1989) 289–312.
- [166] B.M. Barney, T.C. Yang, R.Y. Igarashi, P.C. Dos Santos, M. Laryukhin, H.I. Lee, B.M. Hoffman, D.R. Dean, L.C. Seefeldt, Intermediates trapped during nitrogenase reduction of N triple bond N,  $\text{CH}_3\text{-N}=\text{NH}$ , and  $\text{H}_2\text{N-NH}_2$ , *J. Am. Chem. Soc.* 127 (2005) 14960–14961.
- [167] D. Lukoyanov, V. Pelmenshikov, N. Maeser, M. Laryukhin, T.C. Yang, L. Noodleman, D.R. Dean, D.A. Case, L.C. Seefeldt, B.M. Hoffman, Testing if the interstitial atom, X, of the nitrogenase molybdenum-iron cofactor is N or C: ENDOR, ESEEM, and DFT studies of the  $S = 3/2$  resting state in multiple environments, *Inorg. Chem.* 46 (2007) 11437–11449.
- [168] L.C. Seefeldt, B.M. Hoffman, D.R. Dean, Mechanism of Mo-dependent nitrogenase, *Annu. Rev. Biochem.* 78 (2009) 701–722.
- [169] C.J. Walsby, D. Ortillo, J. Yang, M.R. Nnyepi, W.E. Broderick, B.M. Hoffman, J.B. Broderick, Spectroscopic approaches to elucidating novel iron-sulfur chemistry in the “radical-SAM” protein superfamily, *Inorg. Chem.* 44 (2005) 727–741.
- [170] N.S. Lees, D. Chen, C.J. Walsby, E. Behshad, P.A. Frey, B.M. Hoffman, How an enzyme tames reactive intermediates: positioning of the active-site components of lysine 2,3-aminomutase during enzymatic turnover as determined by ENDOR spectroscopy, *J. Am. Chem. Soc.* 128 (2006) 10145–10154.
- [171] D.H. Flint, R.M. Allen, Iron-sulfur proteins with nonredox functions, *Chem. Rev.* 96 (1996) 2315–2334.
- [172] P.A. Frey, Travels with carbon-centered radicals. 5'-deoxyadenosine and 5'-deoxyadenosine-5'-yl in radical enzymology, *Acc. Chem. Res.* 47 (2014) 540–549.
- [173] P.A. Frey, A.D. Hegeman, F.J. Ruzicka, The radical SAM superfamily, *Crit. Rev. Biochem. Mol. Biol.* 43 (2008) 63–88.
- [174] J.B. Broderick, Biochemistry: a radically different enzyme, *Nature* 465 (2010) 877–878.
- [175] Q. Zhang, W.A. van der Donk, W. Liu, Radical-mediated enzymatic methylation: a tale of two SAMs, *Acc. Chem. Res.* 45 (2012) 555–564.
- [176] K.S. Duschene, S.E. Veneziano, S.C. Silver, J.B. Broderick, Control of radical chemistry in the AdoMet radical enzymes, *Curr. Opin. Chem. Biol.* 13 (2009) 74–83.
- [177] G. Layer, D.W. Heinz, D. Jahn, W.D. Schubert, Structure and function of radical SAM enzymes, *Curr. Opin. Chem. Biol.* 8 (2004) 468–476.
- [178] R.U. Hutcheson, J.B. Broderick, Radical SAM enzymes in methylation and methylthiolation, *Metallomics* 4 (2012) 1149–1154.
- [179] S.C. Wang, P.A. Frey, S-adenosylmethionine as an oxidant: the radical SAM superfamily, *Trends Biochem. Sci.* 32 (2007) 101–110.
- [180] J. Cheek, J.B. Broderick, Adenosylmethionine-dependent iron-sulfur enzymes: versatile clusters in a radical new role, *J. Biol. Inorg. Chem.* 6 (2001) 209–226.
- [181] C.J. Walsby, W. Hong, W.E. Broderick, J. Cheek, D. Ortillo, J.B. Broderick, B.M. Hoffman, Electron-nuclear double resonance spectroscopic evidence that S-adenosylmethionine binds in contact with the catalytically active  $[\text{4Fe-4S}]^{2+}$  cluster of pyruvate formate-lyase activating enzyme, *J. Am. Chem. Soc.* 124 (2002) 3143–3151.
- [182] C.J. Walsby, D. Ortillo, W.E. Broderick, J.B. Broderick, B.M. Hoffman, An anchoring role for FeS clusters: chelation of the amino acid moiety of S-adenosylmethionine to the unique iron site of the  $[\text{4Fe-4S}]^{2+}$  cluster of pyruvate formate-lyase activating enzyme, *J. Am. Chem. Soc.* 124 (2002) 11270–11271.
- [183] P. Hanzelmann, H. Schindelin, Crystal structure of the S-adenosylmethionine-dependent enzyme MoaA and its implications for molybdenum cofactor deficiency in humans, *Proc. Natl. Acad. Sci.* 101 (2004) 12870–12875.
- [184] B.W. Lepore, F.J. Ruzicka, P.A. Frey, D. Ringe, The x-ray crystal structure of lysine-2,3-aminomutase from *Clostridium subterminale*, *Proc. Natl. Acad. Sci.* 102 (2005) 13819–13824.
- [185] W. Wang, K. Wang, J. Li, S. Nellutla, T.I. Smirnova, E. Oldfield, An ENDOR and HYSCORE investigation of a reaction intermediate in IspG (GcpE) catalysis, *J. Am. Chem. Soc.* 133 (2011) 8400–8403.
- [186] M.M. Wuebbens, K.V. Rajagopalan, Investigation of the early steps of molybdopterin biosynthesis in *Escherichia coli* through the use of in-vivo labeling studies, *J. Biol. Chem.* 270 (1995) 1082–1087.
- [187] P. Hanzelmann, H. Schindelin, Binding of 5'-GTP to the C-terminal FeS cluster of the radical S-adenosylmethionine enzyme MoaA provides insights into its mechanism, *Proc. Natl. Acad. Sci.* 103 (2006) 6829–6834.
- [188] N.S. Lees, P. Hanzelmann, H.L. Hernandez, S. Subramanian, H. Schindelin, M.K. Johnson, B.M. Hoffman, ENDOR spectroscopy shows that guanine N1 binds to  $[\text{4Fe-4S}]^{2+}$  cluster II of the S-adenosylmethionine-dependent enzyme MoaA: mechanistic implications, *J. Am. Chem. Soc.* 131 (2009) 9184–9185.
- [189] M.M. Cosper, G.N. Jameson, R. Davydov, M.K. Eidsness, B.M. Hoffman, B.H. Huynh, M.K. Johnson, The  $[\text{4Fe-4S}]^{2+}$  cluster in reconstituted biotin synthase binds S-adenosyl-L-methionine, *J. Am. Chem. Soc.* 124 (2002) 14006–14007.
- [190] I. Sanyal, K.J. Gibson, D.H. Flint, *Escherichia coli* biotin synthase: an investigation into the factors required for its activity and its sulfur donor, *Arch. Biochem. Biophys.* 326 (1996) 48–56.
- [191] B. Tse Sum Bui, D. Florentin, F. Fournier, O. Ploux, A. Méjean, A. Marquet, Biotin synthase mechanism: on the origin of sulphur, *FEBS Lett.* 440 (1998) 226–230.
- [192] B. Tse Sum Bui, T.A. Mattioli, D. Florentin, G. Bolbach, A. Marquet, *Escherichia coli* biotin synthase produces selenobiotin. Further evidence of the involvement of the  $[\text{2Fe-2S}]^{2+}$  cluster in the sulfur insertion step, *Biochemistry* 45 (2006) 3824–3834.
- [193] F. Pierrel, G.R. Bjork, M. Fontecave, M. Atta, Enzymatic modification of tRNAs: MiaB is an iron-sulfur protein, *J. Biol. Chem.* 277 (2002) 13367–13370.
- [194] F. Pierrel, T. Douki, M. Fontecave, M. Atta, MiaB protein is a bifunctional radical-S-adenosylmethionine enzyme involved in thiolation and methylation of tRNA, *J. Biol. Chem.* 279 (2004) 47555–47563.
- [195] H.L. Hernandez, F. Pierrel, E. Elleingand, R. Garcia-Serres, B.H. Huynh, M.K. Johnson, M. Fontecave, M. Atta, MiaB, a bifunctional radical-S-adenosylmethionine enzyme involved in the thiolation and methylation of tRNA, contains two essential  $[\text{4Fe-4S}]^{2+}$  clusters, *Biochemistry* 46 (2007) 5140–5147.
- [196] S. Boutigny, A. Saini, E.E. Baidoo, N. Yeung, J.D. Keasling, G. Butland, Physical and functional interactions of a monothiol glutaredoxin and an iron sulfur cluster carrier protein with the sulfur-donating radical S-adenosyl-L-methionine enzyme MiaB, *J. Biol. Chem.* 288 (2013) 14200–14211.
- [197] T. Molle, S. Arragain, R. Garcia, M. Clemancey, J. Latour, M. Fontecave, E. Mulliez, M. Atta, S. Gambarelli, J. Mouesca, M. Fontecave, S. Kieffer-Jaquinet, F. Forouhar, J.F. Hunt, Sulfur insertion in biology by radical mechanism: study of methylthiotransferases RimO and MiaB, *J. Biol. Inorg. Chem.* 19 (2014) S251–S251.
- [198] B.J. Landgraf, A.J. Arcinas, K.H. Lee, S.J. Booker, Identification of an intermediate methyl carrier in the radical S-adenosylmethionine methylthiotransferases RimO and MiaB, *J. Am. Chem. Soc.* 135 (2013) 15404–15416.
- [199] F. Forouhar, S. Arragain, M. Atta, S. Gambarelli, J.M. Mouesca, M. Hussain, R. Xiao, S. Kieffer-Jaquinet, J. Seetharaman, T.B. Acton, G.T. Montelione, E. Mulliez, J.F. Hunt, M. Fontecave, Two Fe-S clusters catalyze sulfur insertion by radical-SAM methylthiotransferases, *Nat. Chem. Biol.* 9 (2013) 333–338.
- [200] H.I. Lee, R.Y. Igarashi, M. Laryukhin, P.E. Doan, P.C. Dos Santos, D.R. Dean, L.C. Seefeldt, B.M. Hoffman, An organometallic intermediate during alkyne reduction by nitrogenase, *J. Am. Chem. Soc.* 126 (2004) 9563–9569.
- [201] I. Dance, The mechanism of nitrogenase. Computed details of the site and geometry of binding of alkyne and alkene substrates and intermediates, *J. Am. Chem. Soc.* 126 (2004) 11852–11863.
- [202] M. Rohmer, The discovery of a mevalonate-independent pathway for isoprenoid biosynthesis in bacteria, algae and higher plants, *Nat. Prod. Rep.* 16 (1999) 565–574.
- [203] W. Eisenreich, A. Bacher, D. Arigoni, F. Rohdich, Biosynthesis of isoprenoids via the non-mevalonate pathway, *Cell. Mol. Life Sci.* 61 (2004) 1401–1426.
- [204] F. Rohdich, A. Bacher, W. Eisenreich, Isoprenoid biosynthetic pathways as anti-infective drug targets, *Biochem. Soc. Trans.* 33 (2005) 785–791.
- [205] E. Oldfield, Targeting isoprenoid biosynthesis for drug discovery: bench to bedside, *Acc. Chem. Res.* 43 (2010) 1216–1226.
- [206] A.K. Kollas, E.C. Duin, M. Eberl, B. Altincicek, M. Hintz, A. Reichenberg, D. Henschker, A. Henne, I. Steinbrecher, D.N. Ostrovsky, R. Hedderich, E. Beck, H. Jomaa, J. Wiesner, Functional characterization of GcpE, an essential enzyme of the non-mevalonate pathway of isoprenoid biosynthesis, *FEBS Lett.* 532 (2002) 432–436.
- [207] D. Adedeji, H. Hernandez, J. Wiesner, U. Kohler, H. Jomaa, E.C. Duin, Possible direct involvement of the active-site  $[\text{4Fe-4S}]^{2+}$  cluster of the GcpE enzyme from *Thermus thermophilus* in the conversion of MeCpP, *FEBS Lett.* 581 (2007) 279–283.
- [208] B. Altincicek, E.C. Duin, A. Reichenberg, R. Hedderich, A.K. Kollas, M. Hintz, S. Wagner, J. Wiesner, E. Beck, H. Jomaa, LytB protein catalyzes the terminal step of the 2-C-methyl-D-erythritol-4-phosphate pathway of isoprenoid biosynthesis, *FEBS Lett.* 532 (2002) 437–440.
- [209] W. Wang, J. Li, K. Wang, C. Huang, Y. Zhang, E. Oldfield, Organometallic mechanism of action and inhibition of the 4Fe-4S isoprenoid biosynthesis protein GcpE (IspG), *Proc. Natl. Acad. Sci.* 107 (2010) 11189–11193.
- [210] W. Xu, N.S. Lees, D. Adedeji, J. Wiesner, H. Jomaa, B.M. Hoffman, E.C. Duin, Paramagnetic intermediates of (E)-4-hydroxy-3-methylbut-2-enyl diphosphate synthase (GcpE/IspG) under steady-state and pre-steady-state conditions, *J. Am. Chem. Soc.* 132 (2010) 14509–14520.
- [211] W. Wang, K. Wang, Y.L. Liu, J.H. No, J. Li, M.J. Nilges, E. Oldfield, Bioorganometallic mechanism of action, and inhibition, of IspH, *Proc. Natl. Acad. Sci.* 107 (2010) 4522–4527.
- [212] M. Wolff, M. Seemann, B. Tse Sum Bui, Y. Frapart, D. Tritsch, A.G. Estrabot, M. Rodríguez-Concepción, A. Boronat, A. Marquet, M. Rohmer, Isoprenoid biosynthesis via the methylerythritol phosphate pathway: the (E)-4-hydroxy-3-methylbut-2-enyl diphosphate reductase (LytB/IspH) from *Escherichia coli* is a  $[\text{4Fe-4S}]^{2+}$  protein, *FEBS Lett.* 541 (2003) 115–120.
- [213] K. Wang, W. Wang, J.H. No, Y. Zhang, Y. Zhang, E. Oldfield, Inhibition of the  $\text{Fe}_4\text{S}_4$ -cluster-containing protein IspH (LytB): electron paramagnetic resonance, metallacycles, and mechanisms, *J. Am. Chem. Soc.* 132 (2010) 6719–6727.
- [214] W. Xu, N.S. Lees, D. Hall, D. Welideniya, B.M. Hoffman, E.C. Duin, A closer look at the spectroscopic properties of possible reaction intermediates in wild-type and mutant (E)-4-hydroxy-3-methylbut-2-enyl diphosphate reductase, *Biochemistry* 51 (2012) 4835–4849.



- [215] W. Wang, K. Wang, I. Span, J. Jauch, A. Bacher, M. Groll, E. Oldfield, Are free radicals involved in IspH catalysis? An EPR and crystallographic investigation, *J. Am. Chem. Soc.* 134 (2012) 11225–11234.
- [216] J. Li, K. Wang, T.I. Smirnova, R.L. Khade, Y. Zhang, E. Oldfield, Isoprenoid biosynthesis: ferraoxetane or allyl anion mechanism for IspH catalysis? *Angew. Chem. Int. Ed. Engl.* 52 (2013) 6522–6525.
- [217] I. Span, T. Grawert, A. Bacher, W. Eisenreich, M. Groll, Crystal structures of mutant IspH proteins reveal a rotation of the substrate's hydroxymethyl group during catalysis, *J. Mol. Biol.* 416 (2012) 1–9.
- [218] I. Span, K. Wang, W. Eisenreich, A. Bacher, Y. Zhang, E. Oldfield, M. Groll, Insights into the binding of pyridines to the iron–sulfur enzyme IspH, *J. Am. Chem. Soc.* 136 (2014) 7926–7932.
- [219] I. Span, K. Wang, W. Wang, Y. Zhang, A. Bacher, W. Eisenreich, K. Li, C. Schulz, E. Oldfield, M. Groll, Discovery of acetylene hydratase activity of the iron–sulphur protein IspH, *Nat. Commun.* 3 (2012) 1042.